UNIVERSITÀ DI PARMA

UNIVERSITA' DEGLI STUDI DI PARMA
Department of Engineering for Industrial Systems and Technologies

Ph.D. in Industrial Engineering
XXXVII cycle

Mechanical Behavior and Failure Analysis of Additively Manufactured Cellular Structures and Architected Materials

Candidate:
Alberto Corvi

Supervisor:
Prof. Luca Collini

Coordinator:
Prof. Gianni Royer Carfagni

Academic Years 2021/2022 – 2023/2024

To Caterina
To my parents

Contents

List of Figures

List of Tables

Abstract

In recent years, cellular solids and architected materials have garnered increasing attention, thanks to their superior mechanical performance. This allows scientists nowadays to explore new regions in the material property space, paving the pathway to a revolution in most of engineering disciplines. This thesis opens with an exploration on the mechanical behavior of novel multi-phase cellular structures in quasi-static and dynamic conditions: experiments and simulations on foam- and shear-thickening-fluid-filled cellular structures are performed in parallel, to analyze the influence and the interaction between each constituent material on the global composite structure's properties. The wide spread of cellular structures is supported by the impressive advancements in additive manufacturing technologies, now able to fabricate structures with such complex geometries, otherwise impossible to obtain with traditional manufacturing processes. Following this, a further study on the failure mechanism of cellular structures and on the effect of the 3D-printing process on the mechanical properties of the material in safe and damage regimes is required. A multi-scale approach and a directional damage model, both based on microscopy analysis, are proposed to model parts produced via material extrusion and are validated against experimental tests, correctly predicting their predominant deformation and failure mechanisms. Moving the attention to the unprecedented potential of architected materials, focus is set on kirigami meta-materials. By harnessing the mechanics of a bi-stable truss, studied via analytical and experimental approaches, a new design methodology for multi-stable kirigami meta-materials is proposed, extending the kirigami world to aperiodic and potentially arbitrary geometries.

Highlights

- **Multi-Phase Cellular Structures**

  The state of the art shows some works on foam-filled honeycombs but no references to fluid-filled periodic structures. Here, a comprehensive investigation based on a full understanding of the interaction between the two phases is developed. Following, a novel composite meta-material with adaptive impact resistance is designed.

- **Mechanics and Failure Mechanisms of 3D-Printed Structures**

  Available works on the mechanical properties of 3D-printed structures concern analytical predictions and complex simulation methodologies. A multi-scale approach and an analysis specifically on lattice structures, to capture the mechanical behavior up to failure, are introduced and validated, paving the way to computationally efficient material modeling of additively manufactured parts.

- **Novel Kirigami Meta-Materials**

  Some works on bi-stable kirigami are available in literature, though limited to few and periodic patterns. A new design methodology is here presented. Starting from the underlying mechanics, this strategy allows to expand the kirigami applicability to aperiodic and possibly arbitrary tilings.

Aknowledgements

I am sincerely thankful to my supervisor Prof. Luca Collini for his expert guidance and encouragement throughout this journey.

I also want to aknowledge Prof. Katia Bertoldi and Dr. Anne Meeussen from Harvard University for trusting in me and working together.

I want to thank my colleagues Matteo and Farzad for the fruitful discussions and feedbacks, sharing the challenges of this journey.

I express my deepest gratitude to all my family and Caterina for the constant support, driving force for this accomplishment. This thesis is dedicated to you.

Introduction

Cellular structures and architected materials have gained a vital importance in modern engineering, thanks to their light weight combined with superior performance and functionality. The optimized properties of these family of engineered materials make them ideal candidates to address the new requirements in most of the applications where reducing weight is critical. Additionally, the ability to tailor their internal geometry allows engineers to design materials with specific tunable properties, further enhancing their versatility in advanced smart and functional solutions. This allows scientists nowadays to explore new regions in the material property space, paving the pathway to a revolution in most of engineering disciplines.

Motivated by this, the aim of this thesis is therefore to contribute in the scientific community effort to better understand the mechanical behavior of cellular and architected materials in order to provide more novel and structured hints in the design stage.

The thesis is structured in three chapters, each of them targeting a different topic in the framework described above. A brief resume of the chapters follows:

Chapter 1 opens with an overview on cellular solids, presenting their main common features and the structures' classification. A globally-walled additively manufactured periodic structure is introduced as the starting point for the study of this chapter; the empty space inside the structure is filled with a secondary material in a different physical phase, and the interaction between each constituent material on the global composite structure's properties is investigated. In details, a polymeric foam and a shear-thickening

fluid are adopted as fillers, for quasi-static and dynamic loading conditions, respectively. Both experimental and simulation results prove the desired enhancement in the mechanical performance, confirming the utility of the proposed idea and opening a new range of possible applications.

Chapter 2 addresses the need of having a comprehensive and computationally efficient way to model additively manufactured components inside numerical environment. In other words, on one side most of the available approaches focus only on the mechanics at the micro-scale and are therefore not helpful in modelling actual components, and on the other side modelling a 3D-printed part as if fabricated with traditional subtractive or formative technologies does not capture all the peculiar characteristics derived from the additive process. Starting from the analysis of the failure mechanisms, a multi-scale approach is proposed considering the effect of process conditions on the micro-structure and consequently on the part strength: the model captures accurately the material response both in safe and damage regimes. Focusing again on cellular structures, an anisotropic damage model is also proposed, as the complex geometry of such structures does not allow to consider the periodicity of a unit-cell block of material.

Chapter 3 deals with the design of architected materials with unprecedented properties. Inspired by the recently developed engineering devices with smart and functional properties inspired by the Japanese art of rationally cutting thin sheets of paper, a new design methodology is proposed to generate novel auxetic highly multi-stable kirigami meta-materials. The building block for this strategy is the bi-stable Von Mises truss, which is extensively studied in this chapter via an analytical model validated against experiments. Once the underlying physics is fully clarified, it is harnessed to move into unexplored regions of the design space. Starting from a new tile definition, geometric constraints are gradually reduced, increasing the design degrees of freedom: multi-stable kirigami meta-materials can be obtained from aperiodic tilings, such as the Penrose, and possibly arbitrarily complex tilings, like the Girih.

Multi-Phase Cellular Structures

The following articles have been extracted from the content of this chapter:

- **A. Corvi**, L. Collini, C. Sciancalepore, Improving the compressive response of biopolymeric additively manufactured cellular structures via foam-filling: An experimental and numerical investigation, *Mechanics of Advanced Materials and Structures*, 2023.
- **A. Corvi**, L. Collini, Shear-thickening-fluid-based meta-material for adaptive impact response, *Materials & Design*, 2024.

1.1 Cellular Structures

In their seminal book *"Cellular Solids: Structure and Properties"* [1], first published in 1988, Gibson and Ashby define a cellular solid as "one made up of an interconnected network of solid struts or plates which form the edges and faces of cells". These structures, characterized by a porous architecture, can be naturally occurring, such as wood, bone, and coral, or engineered for specific applications. Gibson and Ashby systematically explored the mechanical behavior of cellular structures, categorizing cellular materials based on their structural configuration and providing models to predict their mechanical properties. These models have been extensively validated and expanded upon in the literature during the last decades, leading to the development of new cellular designs with enhanced performance, able to address the requirements of modern advanced and functional applications.

Among the families of cellular solids, some of the most commons are honeycombs (Figure 1.1(a)) and foams, which can be further classified in open-cell foams (Figure 1.1(b)) and closed-cell foams (Figure 1.1(c)).

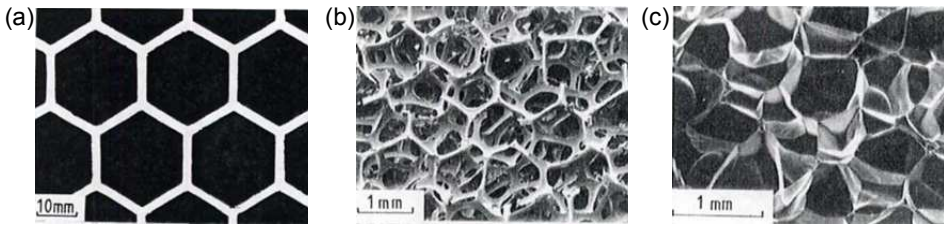

Figure 1.1: Examples of cellular structures: a)Planar honeycomb; b)Open-cell foam; c)Closed-cell foam.

Nature is full of cellular structures: Figure 1.2 brings as examples the porous medium of the trabecular bone (a), the bee honeycomb (b), and the dragonfly wing structure (c). These structures are the result of millions of years of evolution and adaptation of natural species, and the underlying reason is that the unique geometric configuration of cellular structures allows for efficient material usage while providing superior mechanical performance,

such as energy absorption, stiffness, and impact resistance. More in details, the primary advantage of cellular solids lies in their ability to achieve an incredibly high strength-to-weight ratio, making them ideal candidates for applications where reducing weight without compromising strength is crucial.

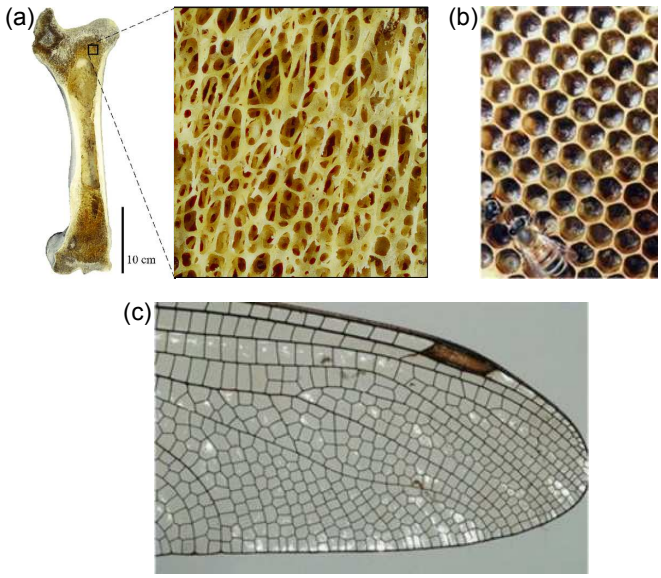

Figure 1.2: Cellular structures in nature: a)Trabecular bone; b)Bee honeycomb; c)Dragonfly wing.

Following this, it is possible to introduce the concept of relative density ρ_r, which is the most important parameter to classify cellular solids, defined as the ratio of the density of the cellular material ρ_c to the density of the solid material from which it is made ρ_s, as expressed in

$$\rho_r = \frac{\rho_c}{\rho_s} \tag{1.1}$$

It is demonstrated how this parameter influences the behavior of cellular structures: Gibson and Ashby's work laid the groundwork on this, showing that mechanical properties can be tailored by adjusting the architecture and relative density of the cells. Key mechanical properties include:

- Stiffness and Strength: The stiffness and strength of cellular structures are strongly influenced by their relative density. As the relative density

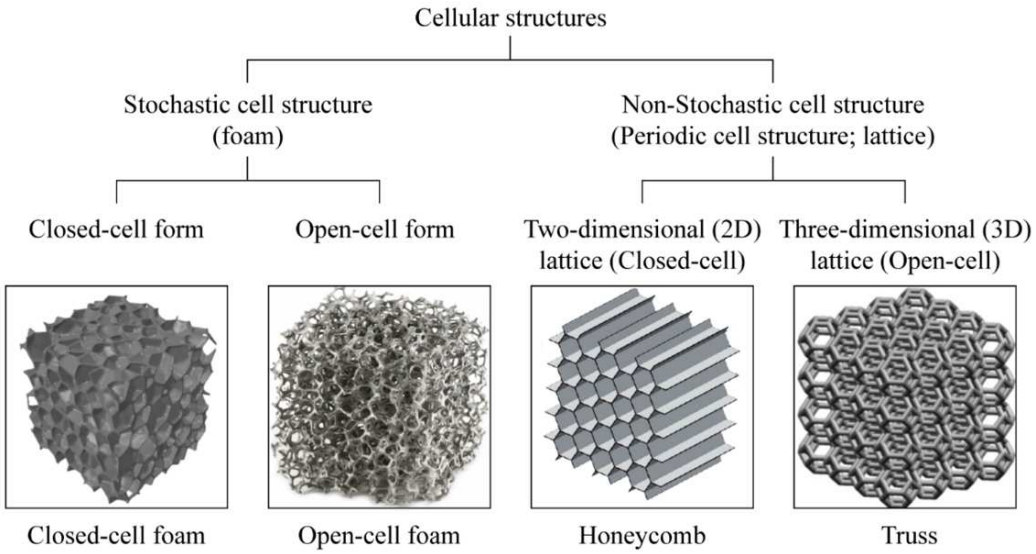

Figure 1.3: Classification of cellular structures

increases, the stiffness and strength typically increase, but at the cost of higher weight. Cellular structures can be designed to achieve a balance between these properties, making them suitable for load-bearing applications.

- Energy Absorption: The porous nature of cellular structures allows them to deform under load, dissipating energy and reducing the transmitted force: they excel in energy absorption, which is critical for impact protection and cushioning applications. The essence of protective packaging is the ability to convert kinetic energy into energy of some other kind while keeping the peak force below a certain threshold. For the same quantity of absorbed energy, the cellular structure always generates a lower peak force than the solid of which it is made. Energy is absorbed as cell walls bend plastically, or buckle, or fracture (depending on the constituent material), but the stress is limited by the long, flat plateau of the stress-strain curve, which allows large energy absorption at near constant load, as shown in Figure 1.4(a). Figure 1.4(b) proves the existence of an optimum density value to absorb a defined quantity of energy at the lowest peak stress σ_P. Each density

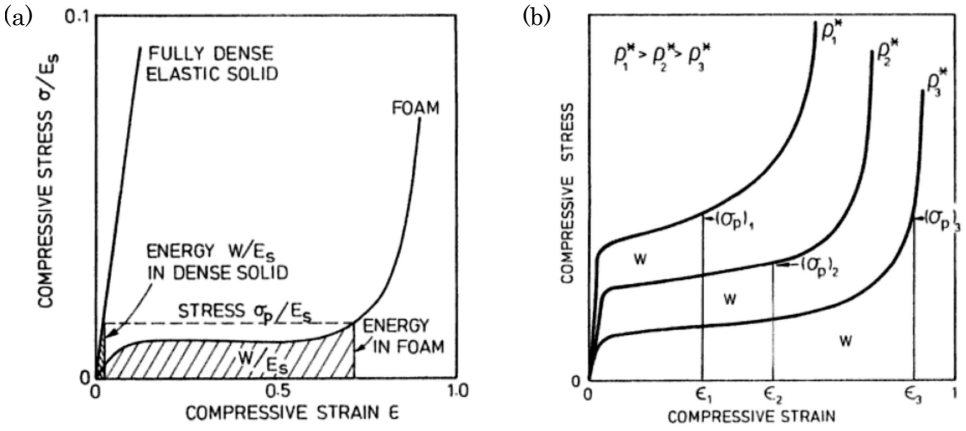

Figure 1.4: Energy absorption in cellular structures: a)Comparison between cellular and elastic solids; b)Optimum density to absorb a fixed amount of energy. *Reproduced from* [1].

has a maximum stress for which it is the best choice. Idealizing the stress-strain curve in the way shown in the inset of Figure 1.5, i.e. considering the linear elastic region being followed by a horizontal plateau at the buckling stress (or plastic collapse stress) and then truncated by a vertical rise at the densification strain $\varepsilon_D = 1 - 1.4\rho_r$, the energy absorption diagram can be modeled as shown in Figure 1.5. Samples with a range of densities are tested in compression, at a fixed strain rate and temperature. The absorbed energy per unit volume up to the stress σ_P is plotted against σ_P for each curve, normalizing by the modulus of the elastic solid material. The shoulder on the energy curve defines the region where the curve corresponding to a certain density lies above that for any other. The envelope line, having a slope of near 1 at low stresses and about 0.85 at high ones, described a relationship between absorbed energy and maximum stress for the optimum density.

- Lightweight: One of the most significant advantages of cellular structures is their low density, which results in lightweight materials with high specific strength and stiffness.

Thanks to their remarkable mechanical response, cellular structures have emerged as a pivotal focus in materials science and engineering, prompting

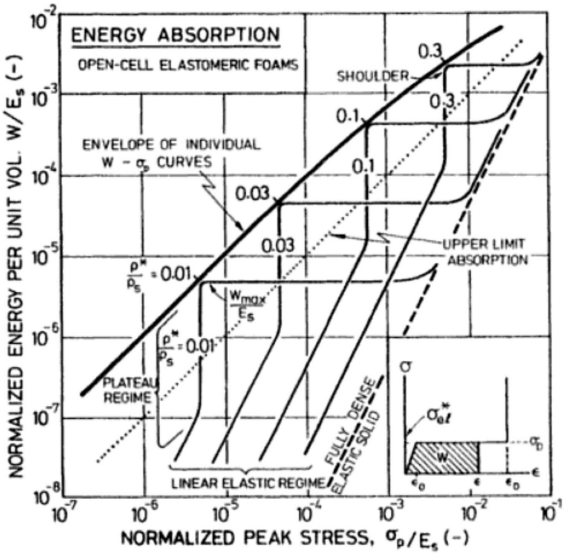

Figure 1.5: Modeling of energy absorption diagram. *Reproduced from* [1].

scientists to mimic designs observed in the biological world in order to create architected structures with particularly desirable properties. A wide range of engineering disciplines, from the aerospace and automotive industries to the biomedical field can significantly benefit from the application of cellular structures into newly designed components with enhanced efficiency and performance.

In the last decade, the wide spread of Additive Manufacturing has paved the way to the development and application of cellular structures. In fact, 3D printing technologies enable the layer-by-layer fabrication of intricate designs required for cellular structures with high precision, otherwise challenging or impossible to create using traditional subtractive or formative manufacturing methods.

Lattice structures are a particular type of cellular structures, consisting of a periodic tessellation of a unit cell arranged to generate a three-dimensional network. These structures are characterized by their open architecture, which can be precisely controlled to achieve desired mechanical properties, offering a high degree of design flexibility that, at least in principle, allows engineers to create materials tailored for specific applications. The field of application

for lattice structures is across different length scales, from below the micro-scale to the centimeter scale (or even to the meter scale if we include reticular structures for civil constructions).

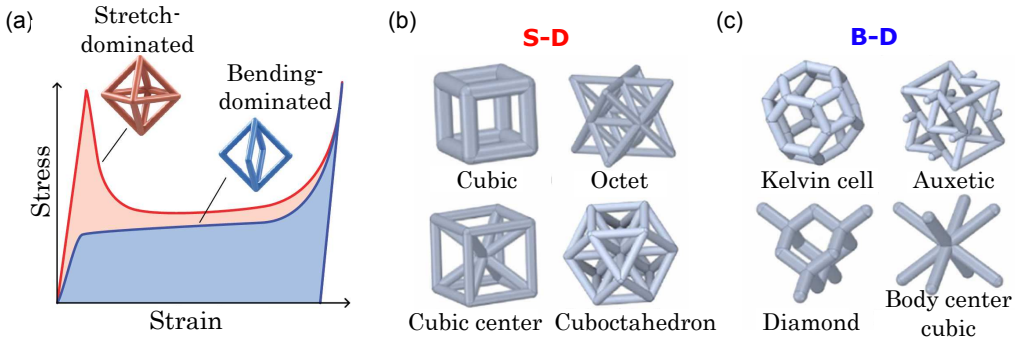

Figure 1.6: Stretch- and bending-dominated lattice structures: a)Stress-strain curves; b)Examples of S-D unit-cells; c)Examples of B-D unit-cells.

Mechanical properties are ruled by the architecture, which can be chosen from the most commonly known range or can be computed through an optimization algorithm for specific requirements. Two main categories can be identified, based on the load-bearing mechanism:

- Stretch-dominated (S-D) lattices: the applied loads are primarily resisted by axial stretching or compression of the struts. This type of lattice structure is typically stiffer and stronger, making it suitable for applications requiring high load-bearing capacity. The typical stress-strain curve is not monotonous because of the appearance of buckling phenomena which are responsible of the curve drop after the stress peak. Examples include the octet truss lattice and the cubic lattice.

- Bending-dominated (B-D) lattices: these lattices resist loads through bending of the struts. These structures are generally more compliant and can absorb more energy before failure, which is advantageous in applications requiring high energy absorption, such as impact protection. The typical stress-strain curve is characterized by a wide plateau region, responsible for the high-energy absorption capability. Examples include the kelvin lattice and the auxetic re-entrant lattice.

At this point, a brief digression on the deformation mechanism in lattice architectures is helpful to clarify the relationship between relative density and the mechanical response of these interesting structures.

Despite cell-shapes being characterized by complex and different geometries, at the simplest level the unit-cell of an open-cell lattice can be modeled as a cubic array of members with length l and square cross section of side t, schematized in Figure 1.7(a): proved they deform and fail by the same mechanisms, their properties can be understood using arguments independent from the specific cell geometry.

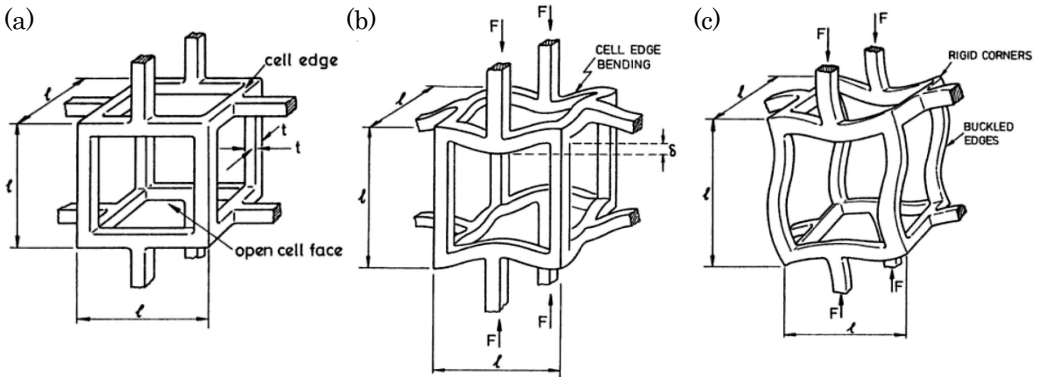

Figure 1.7: Deformation mechanism in open-cell lattices: a)Equivalent cubic cell; b)Linear elasticity: bending; c)Non-linear elasticity: buckling.

Assuming elastic behavior, the Young's modulus for the lattice can be obtained from the linear elastic deflection of a beam loaded at its midpoint, as in Figure 1.7(b). The deflection δ is inversely proportional to the elastic modulus of the material E_s and the second moment of area of a member I: $\delta \propto Fl^3/E_sI$. Considering also that $\sigma \propto F/l^2$ and that $\varepsilon \propto \delta/l$, the elastic modulus of the lattice is:

$$E = \frac{\sigma}{\varepsilon} \propto \frac{F}{\delta l} \propto \frac{E_s I}{l^4} \tag{1.2}$$

Recalling the relationship between geometrical dimensions and relative density $\rho_r \propto (t/l)^2$ and second moment of area $I \propto t^4$, and including all of the geometric constants of proportionality in the factor C_1, it is found that the ratio between the elastic modulus of the lattice and the one of the

elastic solid is function of the square of the relative density, with $C_1 \approx 1$ from experimental data.

$$\frac{E}{E_s} = C_1(\rho_r)^2 \tag{1.3}$$

The linear elastic region is limited to $\varepsilon \leq 0.05$: for larger strains, the deformation of lattice structures shows an extensive plateau at elastic collapse stress σ_{el} (or plastic collapse stress σ_{pl}). The critical load at which a cell edge buckles is given by Euler's formula: $F_{crit} = n^2\pi^2 E_s I/l^2$, with the factor n^2 describing the degree of constraint at the ends of the column. Figure 1.7(c) schematizes the buckling mechanism. The elastic collapse stress is given by $\sigma_{el} \propto F_{crit}/l^2 \propto E_s I/l^4$. Considering again the relationship between geometry and relative density, the normalized elastic collapse stress as well is found to be proportional to the square of the relative density, with the factor $C_4 \approx 0.05$ from experimental data.

$$\frac{\sigma_{el}}{E_s} = C_4(\rho_r)^2 \tag{1.4}$$

After the digression on the deformation mechanisms, other interesting behaviors achieved with lattice structures are worth mentioning. For example, the use of auxetic designs (Poisson's ratio $\nu < 0$), which expand laterally when stretched and shrink when compressed, can lead to materials with improved energy absorption and impact resistance. The open framework of lattice structures also allows for multi-functionality, such as incorporating channels for fluid flow or thermal management. Regarding the multi-functionality, a primary role is played by sheet-based and skeletal-based lattices, also known as Triply-Periodic-Minimal-Surface (TPMS) lattices; the most common designs are shown in Figure 1.8. These geometries are generated from trigonometric equations: modifying the equation controls the shape, size, and density of the 3D structure. Without discussing the mathematical properties and constraints of such equations, TPMS structures outperform strut-based lattices in most of smart and functional applications, mainly thanks to their significantly high surface-to-volume ratio. It is precisely this property that makes TPMS structure incredibly suitable

for thermal applications like heat exchangers, for airflow and noise reduction applications, and also in the bio-medical scaffolds and prosthesis field.

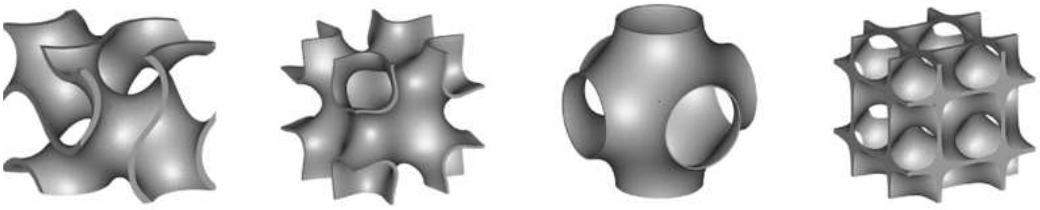

Figure 1.8: Most common TPMS lattices in engineering applications

One of the most significant advancements within additive manufacturing is the development of multi-material AM, which allows the integration of different materials within a single build process. This capability has opened new avenues for the design and fabrication of 3D-printed structures with tailored properties and functionalities. The ability to use multiple materials in a single printing process allows the strategic placement of materials with varying properties, such as stiffness, strength, and elasticity, within the cellular architecture. This selective material distribution can be used to optimize the performance of the structure under specific loading conditions. For instance, stiff and strong materials can be used in regions subject to high stress, while more flexible materials can be incorporated in areas requiring higher strain accommodation. This approach not only improves the overall mechanical performance of the cellular structures but can also introduce new smart functionalities not present in the mono-material design.

A focal point of recent research efforts in the framework of multi-material AM concerns the development and study of composite cellular structures. The integration of secondary materials by filling the voids within these structures aims at further enhancing the mechanical performance of the composite. This innovative approach leverages the synergistic interaction between the structural geometry and the filler material, leading to substantial improvements in energy absorption, mechanical stability, and resistance to dynamic loads when compared to the algebraic sum of the contributions of the two

constituents. In other words, the beneficial phenomenon underlying this approach can be found in the way the different phases interact with each other during the deformation of the composite structure.

The combination of multi-material AM with advanced computational design tools, such as topology optimization and finite element analysis, has further enhanced the performance of cellular structures. Computational models can simulate the mechanical behavior of multi-material cellular structures under various loading conditions, enabling the precise understanding of the structure load-bearing capacity and the consequent stress and deformation field, with the aim to optimize the design by controlling both material distribution and structural geometry.

Despite the significant progress in multi-material AM, several challenges remain, both at the fabrication and at the design stage. The first group includes studies related to material compatibility, interface bonding, and the development of suitable printing processes for a wide range of material combinations; the second group is related with the lack of a deep and comprehensive investigation into the deformation mechanisms at play, and the role of primary and secondary material in this process.

In the following sections, a polymeric 3D-printed TPMS cellular structure is considered. More in details, a Schwarz-Primitive (P) unit-cell, with dimensions 10x10x10 mm and shell thickness 0.8 mm, is periodically repeated in the three-dimensional space via a face-to-face tessellation process.

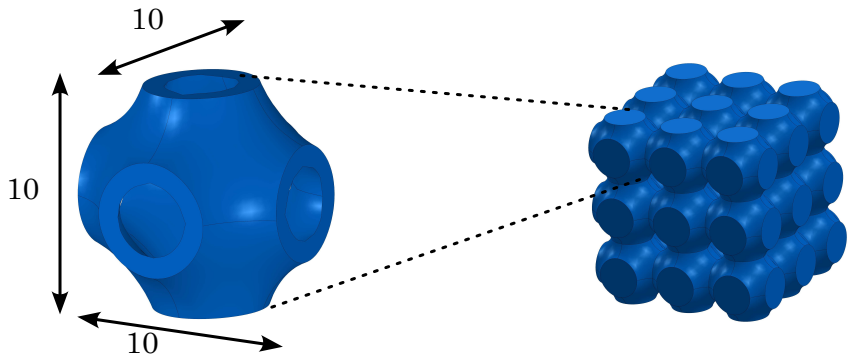

Figure 1.9: Structure geometry for this work

To form a closed volume, suitable to be filled with a secondary material, external walls with the same thickness of 0.8 mm are incorporated around the structure.

The relative density, the most significant parameter to design cellular structures, is set via Equation 1.1 as $\rho_r = 0.26$ and falls within the range proposed by Gibson and Ashby [1] for cellular solids, defined as $\rho_r < 0.3$.

The resulting structure, reported in Figure 1.9 is used as the starting point for two distinct strategies: the closed internal volume has been filled with Poly-Urethane (PU) foam first, and with shear-thickening fluid (STF) secondly, and tested in quasi-static compression and dynamic impact regime, respectively. The ability to integrate different materials within a single structure offers unprecedented opportunities to create optimized cellular architectures that meet the specific demands of various applications, paving the pathway to innovative solutions in aerospace, biomedical, automotive, and other high-performance engineering sectors.

1.2 Foam-filling

In the nature, species have developed structures with multi-functional properties through millions of years of adaptation and evolution. The idea underlying this approach takes inspiration from biological structures that have to provide high energy absorption capability. By observing the turtle shell, the woodpecker skull, and many other systems, it is noted that they are all characterized by an internal foam-like material in between stiffer regions, see Figure 1.10.

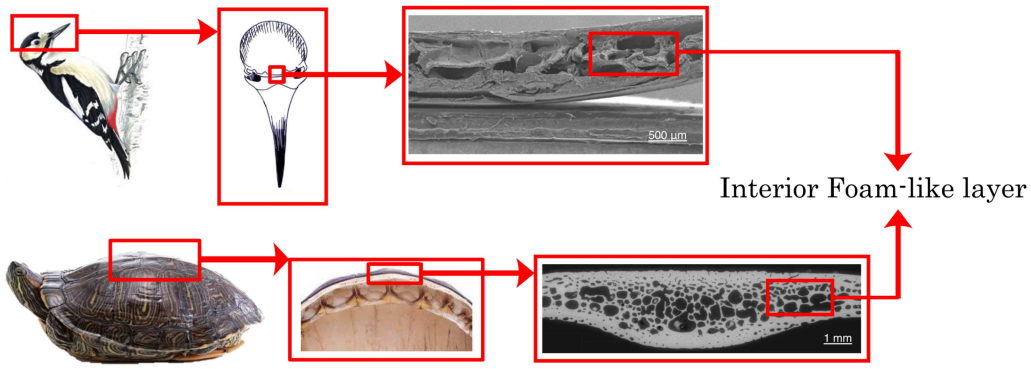

Figure 1.10: Bio-inspiration for multi-phase structures exhibiting enhanced energy absorption capability

Focusing on the unique energy absorption features of such structures, the engineering world is taking inspiration from these biological systems to develop dual-phase composite structures to enhance the mechanical response under compressive loads. Thanks to their characteristic combination of low weight and good thermo-mechanical properties, PU foams are the perfect candidates for this goal.

Some works are available in literature about mechanical tests on thin-walled structures. In particular, the quasi-static and crushing behavior of cylindrical [2], squared [3] and conical [4] tubes filled with a secondary foam-like material is proved to be significantly higher if compared with the empty

tubes. In particular, the most relevant finding is found in Yao [5] and Ren [6] works on foam-filled aluminum multi-cell tubes and stainless-steel auxetic tubes, respectively, experimentally demonstrating the energy absorption capability of the dual-phase assembly being higher than the algebraic sum of the individual contributions of each constituent material. This beneficial phenomenon is noticed also in foam-filled cellular structures: as an example, hexagonal and auxetic honeycombs during in-plane crush [7] and quasi-static uniaxial compression [8] present enhanced load-bearing capacity when totally filled with foam. Recently, foam-filled 3D-printed lattice structures have also combined the effects of novel optimized structure designs with that of the filler. Airoldi [9] proposed an energy absorber based on a 2D hexachiral geometry; Liu [10] developed a zero-Poisson-ratio honeycomb alternating positive- and negative-Poisson-ratio cells and compared the resulting properties when selectively foam-filling only hexagons or only auxetic cells. The desirable effect of the foam on cellular and lattice structures also led to the development of a multi-material additive manufacturing technology by Prajapati [11], which is effective in selectively foam-filling specific regions of the structure including closed volumes.

However, these encouraging findings are related to experimental evidence and lack full investigation into the interaction at play between the two phases. Addressing this gap, it is necessary to provide a deeper insight into the deformation mechanism of such structures.

The walled cellular structure previously discussed in Figure 1.9 is FDM-printed with a non-commercial Poly-(Butylene Adipate-co-Terephthalate) (PBAT) bio-polymer filament: PBAT is gaining significant importance due to its biodegradability in conjunction with good mechanical properties such as remarkable stretchability, leading in the direction of more environmentally friendly manufacturing, especially considering the FDM world where it is a perfect candidate to replace non-biodegradable oil-based flexible filaments that are currently commercially available [12].

Figure 1.11 explains the process to create the PBAT filament suitable for FDM-printing through a single-screw extruder starting from PBAT granules, which also includes multiple fans to cool the polymer and optical sensor to

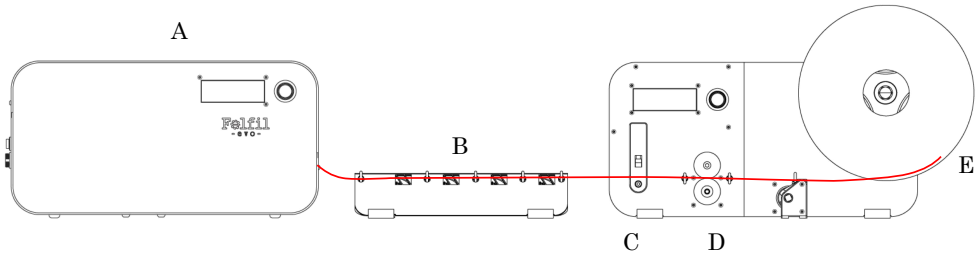

Figure 1.11: Extrusion process to fabricate PBAT filament: a)Single-screw extruder; b)Cooling region; c)Optical sensor; d)Pulling system to control the filament flux; e)Spooler.

precisely set the filament diameter to a constant target value.

Samples consisting of 2x2x2 cell arrays are fabricated in two configurations: empty and filled with PU foam. The filling process involves a modified G-code file which pauses extrusion just before the top layer, foam is sprayed into the cell cavity to completely fill the volume, and the printing is quickly resumed. The scalability of these specimens, which are intended to be effective in representing periodic structures, will be later discussed.

The investigation is performed under both static and cyclic compressive loading. Focus is set on the relationship between the local stress field and the consequent global deformation of the structure, responsible for its overall mechanical properties, especially in terms of energy absorption performance. To this end, a Finite-Element (FE) model is developed with the commercial software Abaqus©to analyze in a deeper way the load distribution in the structure: this will pave the way to new geometry at the design stage, aiming at improving the bi-phase structure functional performance.

To accurately model the materials behavior in the FE model, a proper characterization on the two constituents must be performed. 3D-printed PBAT specimens with standard geometry according to UNI EN ISO 527 and same printing parameters set of the cellular structure undergo a uniaxial tensile test in quasi-static conditions. Stress-strain curves of multiple samples are available in Figure 1.12(a), exhibiting an initial linear elastic response followed by a wide plastic plateau at large strain. Hence, an elasto-plastic

constitutive model is chosen, described by elastic modulus $E = 60$MPa, Poisson's ratio $\nu = 0.46$, and plastic regime defined from tensile test data. On the other hand, cylindrical samples of PU foam, with height-to-radius-ratio $H/R = 1$ and dimensions suitable to consider homogeneous porosity within samples, are subject to compression tests: outcomes are reported in Figure 1.12(b). The foam density is experimentally determined as $\rho_{foam} = 47.2$ kg/m^3. The material behavior is typically hyper-elastic: a *HyperFoam* constitutive model of 3^{rd} degree is found to be the one fitting the best the material response. Equation 1.5 defines the strain energy density function U as function of the principal stretches λ_i for this model.

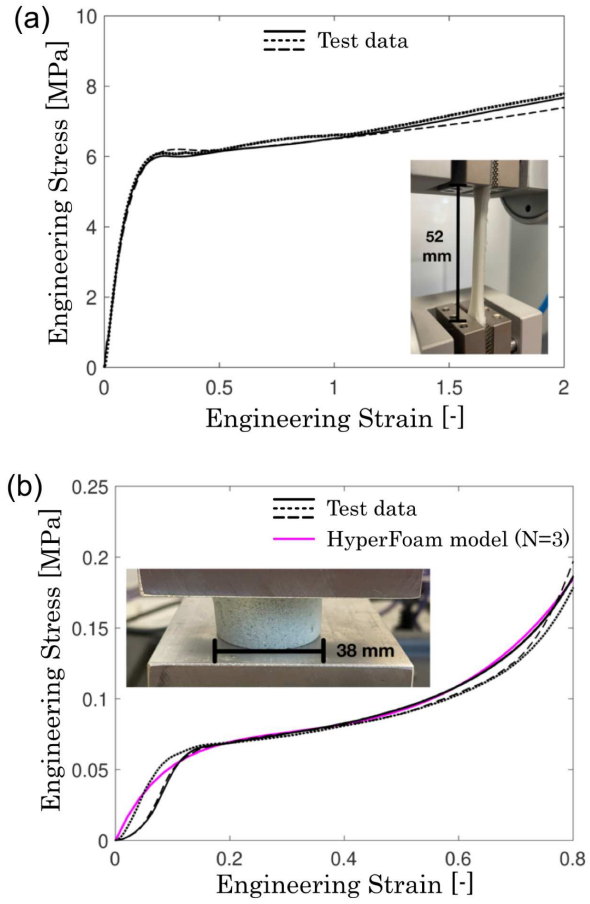

Figure 1.12: Mechanical behavior of the two constituents: a)PBAT tensile tests; b)PU foam compression tests.

$$U = \sum_{i=1}^{N} \frac{2\mu_i}{\alpha_i^2}[\lambda_1^{\alpha_i} + \lambda_2^{\alpha_i} + \lambda_3^{\alpha_i} - 3 + \frac{1}{\beta}(J_{el}^{-\alpha_i\beta} - 1)] \tag{1.5}$$

with β representing the compressibility of the foam, defined as $\beta = \nu/(1-2\nu)$. All coefficients employed to perform the fitting are listed in Table 1.1.

Table 1.1: HyperFoam model coefficients

	μ_i	α_i	β
i=1	-0.200436	9.09239	
i=2	0.205346	9.09473	1.16666
i=3	0.443730	-9.14177	

The numerical analysis is performed in the Abaqus Explicit environment. *General contact* is set for all the contact pairs and self-contact during the analysis, with *Hard contact* property in the normal direction and *Penalty* function with 0.2 friction coefficient in the tangential direction. *Tie* constraint is set between the cell internal surface and the external surface of the foam, avoiding any detachment between shell and foam, in line with what observed in specimens sectioned after deformation, found to maintain perfect adhesion between the two phases. Both the upper and lower plates are modeled via analytically rigid surfaces. Linear C3D4 elements are adopted to mesh the structure and the foam. Mass scaling with a factor 10 is employed over the whole model to scale the minimum solution increment, with no loss of physical meaning.

Numerical simulation outputs are compared with experimental outcomes in terms of load-displacement curves and global deformation of the structure, up to the densification regime which occurs at approximately 70% of nominal compression. Both empty and Foam-Filled (FF) configurations are tested under compression loading at a displacement rate of 5mm/min.

Results from Figure 1.13 show that foam-filling the cellular structure leads to an increase in the load-carrying capacity at the end of the initial linear response. Despite the additional strength provided by the foam being negligible for small deformations, at increasing compression levels the dif-

ference between the two responses becomes significant, with the foam-filled composite characterized by a higher load carrying capacity over the plateau region. This enhanced mechanical response is not due to the load-bearing contribution of the foam, which is almost negligible despite its hyper-elastic behavior, but it is related with the monotonically non-decreasing slope of the foam-filled curve, in contrast with the fluctuating curve exhibited by the empty structure.

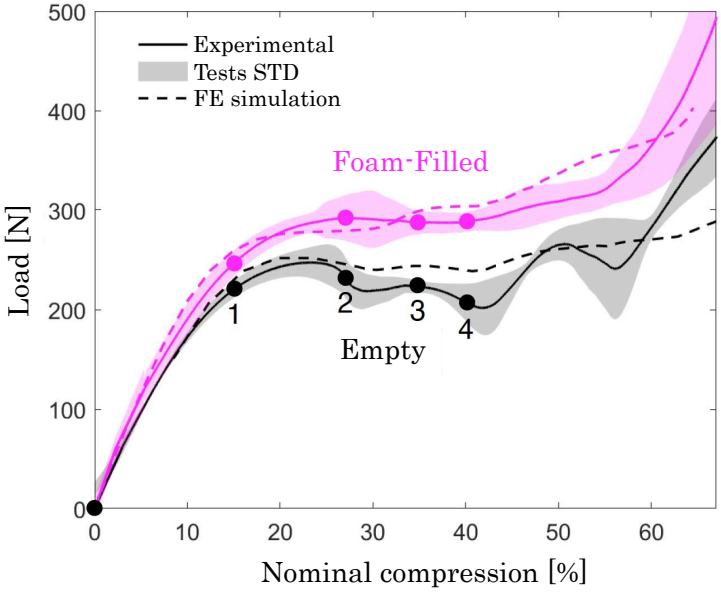

Figure 1.13: Experimental and numerical compression test for empty and foam-filled samples

The reason for this is found in the instabilities occurring in the cell walls of the empty configuration: this does not happen in the foam-filled configuration, characterized by a load stabilization in between approximately 25% and 50% of global compression. To further investigate this phenomenon, the stress field for both configurations is analyzed in Figure 1.14(a) for five values of progressive nominal compression (0(0%), 1(15%), 2(27%), 3(35%) and 4(40%)). The two configurations are characterized by very different global deformation mechanisms.

The empty configuration was severely affected by the collapse of the upper

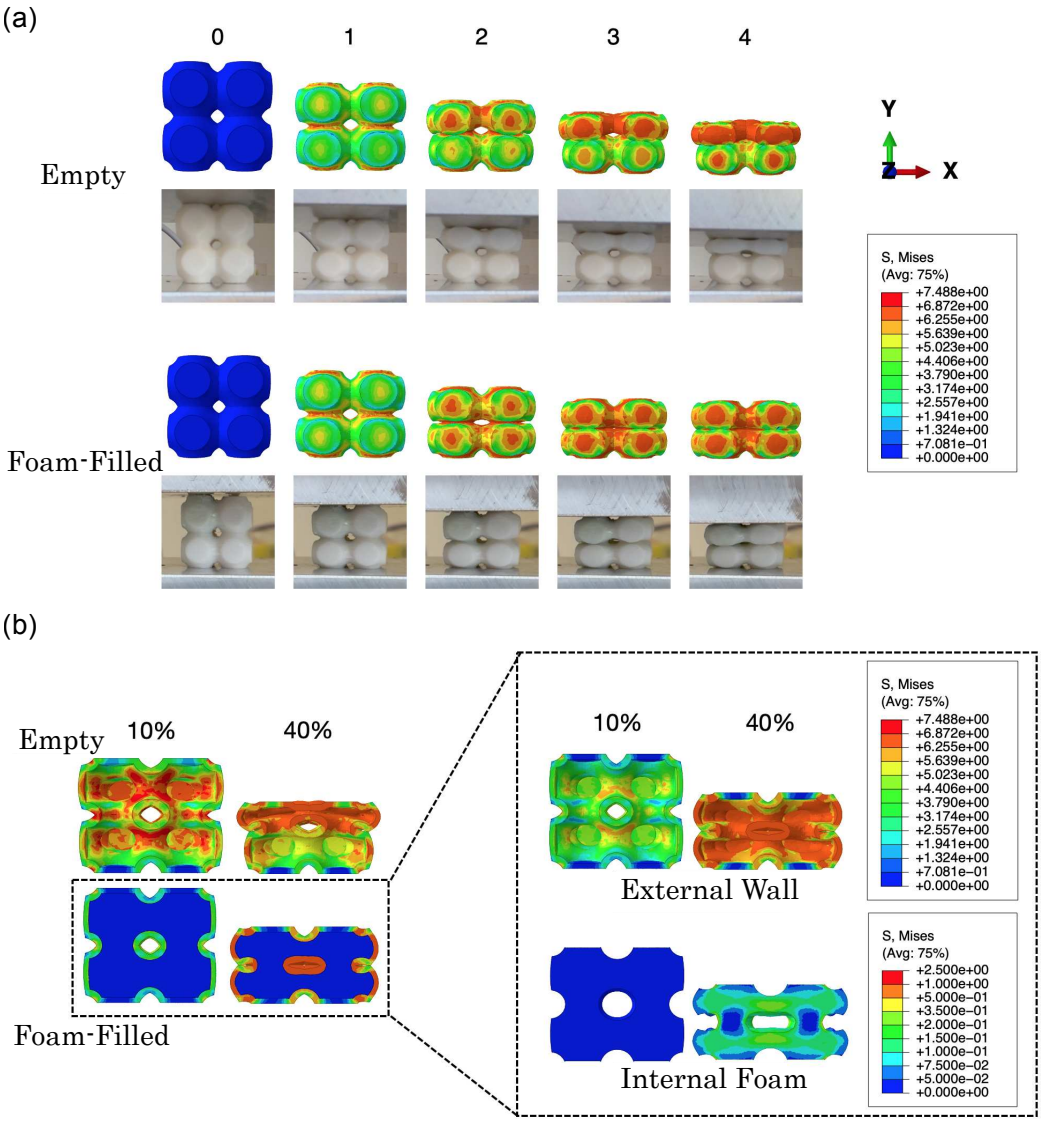

Figure 1.14: Global deformation mechanisms for empty and foam-filled structures: a)Stress field at different compression stages; b)Foam contribution.

cell layer, which completely lost its load-bearing capacity, while the bottom layer was only slightly deformed. On the other hand, the foam-filled structure presented an overall regular deformation, even for severe compression levels, hence leading to an isotropic stress distribution in the cell wall. This behavior, discussed in Figure 1.14(b), highlights the fact that foam-filling the cellular structure generates benefits which go way beyond the strength of the

foam itself, which is almost two orders of magnitude less than that of the wall. PU foam is, indeed, acting as a constraint for transverse displacement, preventing inward/outward bending of the cell wall, achieving an almost total reduction of the deformation anisotropy related with the consequent enhanced load carrying capacity.

This behavior is supported by the plot in Figure 1.15, where the reduction in anisotropy achieved with foam is discussed in terms of the average axial stress at the center of cell walls in the upper and lower cells layers. For increasing levels of nominal compression, the foam-filled structure shows the same load-bearing performance in both layers, confirming the uniform global deformation, while the layers of the empty structure undergo totally different stress fields. The same exact trend is noticed also in the three-layer 27-cell structure, excluding any scale effects (this concept will be deeper analyzed later) and proving once again the beneficial effect of the foam on the cellular structure global deformation mechanism.

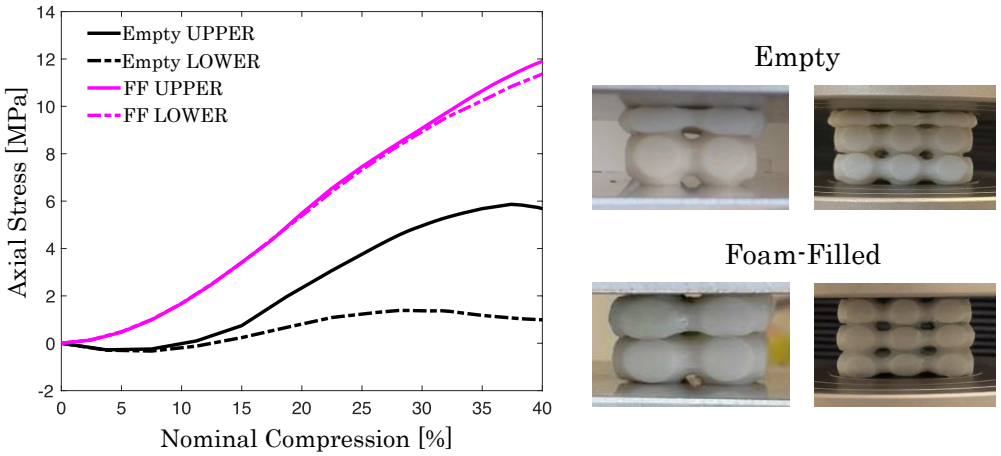

Figure 1.15: Comparison on the stress distribution

To provide an additional more in-depth understanding of the stress distribution within the structures in the two explored configurations, a path is defined through the wall thickness at the center of the external wall, as shown in Figure 1.16, where the maximum value of stress is attained.

The comparison between the upper and the lower layer at 35% nominal

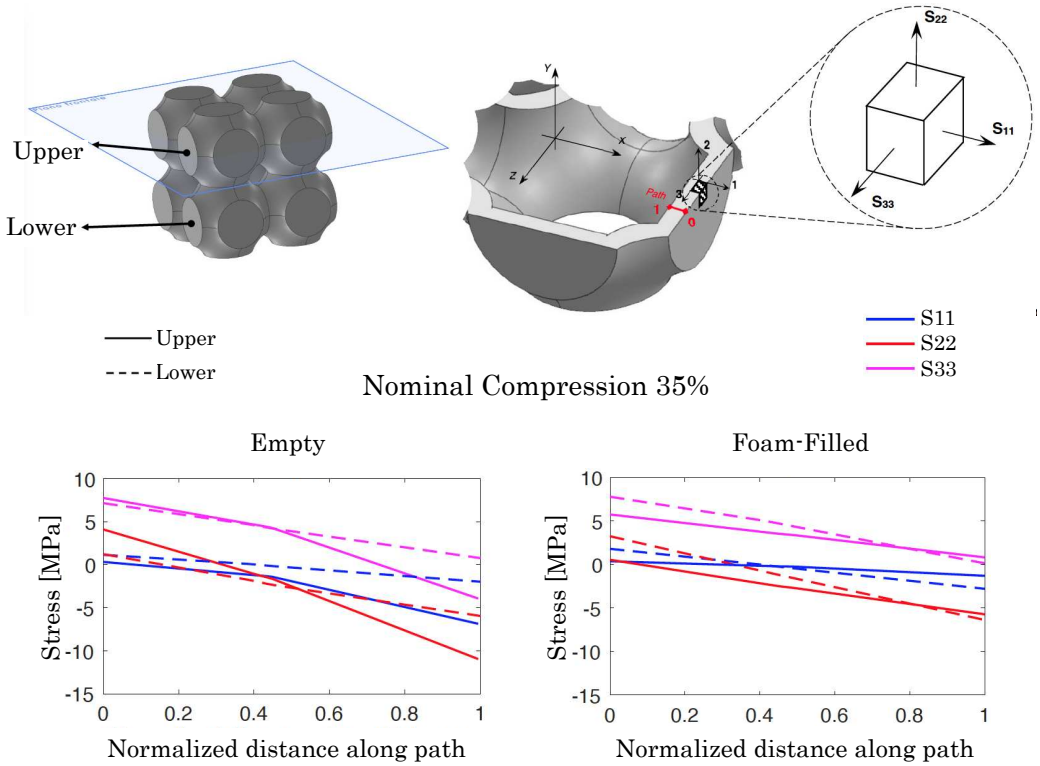

Figure 1.16: Stress distribution in the structure thickness during deformation

compression provides data to support the stress regularization effect. The difference between the two configurations becomes indeed more remarkable when the previously discussed different macroscopic deformation mechanisms take place. For example, focusing on the the axial stress (S22) of the upper layer, displayed by the continuous red line, it can be observed that in the foam-filled structure the walls undergo only compressive stress (from 0 to 5MPa) while for the empty structure the material enters a severe bending stress state with a much more significant gradient (4MPa and -12 MPa at the path boundaries).

To evaluate the mechanical performance of both empty and foam-filled configurations, the total (TEA) and the specific (SEA) energy absorption capabilities (Equation 1.16) are defined, with F representing the applied load and M the mass of the sample.

$$TEA = \int_{x_0}^{x_f} F(x)dx \qquad SEA = \frac{TEA}{M} \tag{1.6}$$

The beneficial effect from filling the structure with a secondary foamy material is not limited to the enhanced overall compressive performance and the more isotropic response at the macro-scale, previously discussed in details. Further to these outcomes, the TEA of the FF configuration is found to be much higher than the algebraic sum of the individual contributions of the constituents, PBAT structure and PU foam. This finding, observed also in different geometries and materials [5, 6], justifies the investigation into foam-filled cellular structures. The highlighted region in Figure 1.17(a) represents the enhancement in the load-carrying performance by the FF configuration: the significance of interactions between the wall and foam is quantified in 1.17(b). The FF configuration exhibits an 18% increase in SEA capability compared to the empty configuration. This unique behavior is mainly due to the interaction effect between the two phases and can again be accounted for in terms of more regular deformation during compression: filling of cellular structures subjected to compressive stresses with foam prevents instability phenomena and leads to a deformation mode that limits the onset of buckling, resulting in a more stable mechanical response.

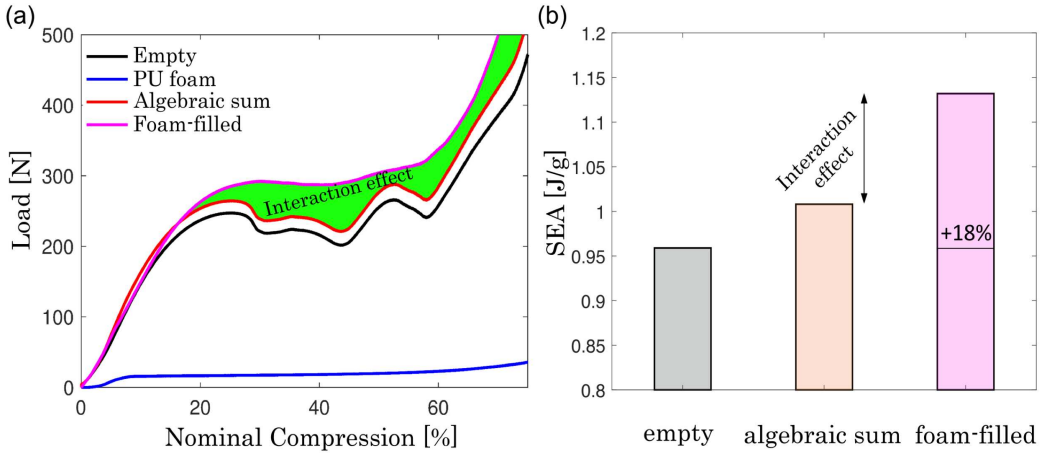

Figure 1.17: Interaction effect between the structure and the filling foam: a)Load-bearing performance; b)Comparison in terms of SEA.

Loading-unloading cycle up to 75% of nominal compression is also applied, using the same test parameters as quasi-static monotonic tests, to investigate the transient behavior of the material. To this end, the total (TED) and specific (SED) energy dissipation values (Equation 1.7) are also introduced, where x_0 and x_f represent the displacement at the first and final stages, respectively.

$$TED = \int_{x_0}^{x_f} F(x)dx - \int_{x_f}^{x_0} F(x)dx \qquad SED = \frac{TED}{M} \tag{1.7}$$

Specific damping capacity (SDC) is another important parameter to be considered when investigating the cyclic behavior, being defined as the ratio between energy dissipation and absorption.

$$SDC = \frac{TED}{TEA} \tag{1.8}$$

Figure 1.18(a) compares the cyclic response of the two configurations after the first cycle. The TED is represented by the (coloured) area enclosed between the loading and unloading curves in the load-displacement plot.

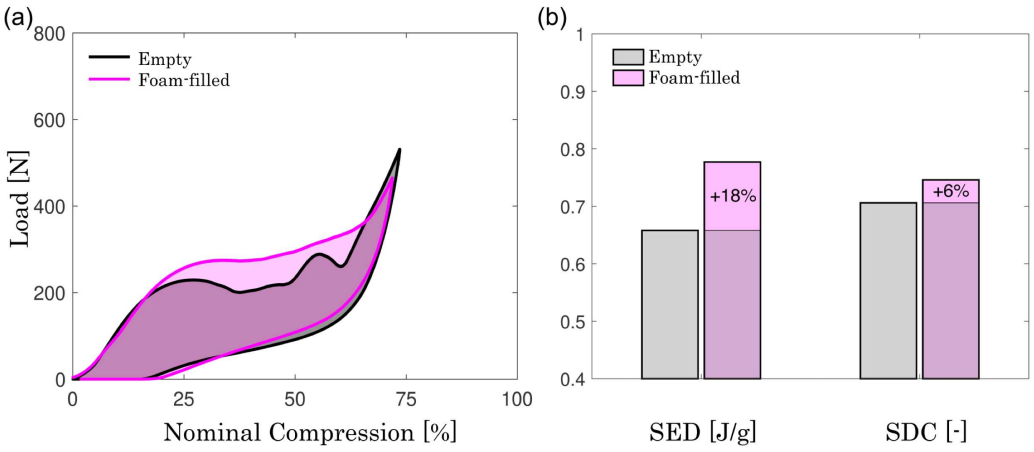

Figure 1.18: Cyclic loading for empty and foam-filled structures: a)Load-displacement curves; b)Enhancement in the SED and SDC parameters.

A significant increase in the specific energy dissipation capability can be observed in Figure 1.18(b). Such an improvement is strongly sought after as a beneficial effect of foam filler materials within thin external shells and can be easily explained by the previously discussed different deformation mechanisms, together with the hysteretic response of PU foam itself, which is not unusual amongst hyper-elastic materials. The SED gained more than 18% with the presence of foam, while the SDC increased by more than 6%. The latter was not very high as the unloading response was similar in both configurations: the increased load-bearing capacity of the FF structure provides the same increase both in TEA and TED, with the effective enhancement of SDC not able to reach very high values.

After the discussion of all the numerical and experimental findings, it is necessary to spend some time in validating the effectiveness of the analyzed samples in representing a periodic structure. In other words, as the considered structure is a cellular solid based on spatial face-to-face tessellation of a unit cell, the scalability of the findings must be determined and proved. It is impossible to determine the influence of the finite geometry and of border effects on the structure mechanical response during experiments: to this end, a method is developed to verify that the considered geometry is a significant reference volume describing the response of a much larger component. The methodology consists in testing samples with different size, i.e. with different number of cells (see 1.19(a)), and requires two steps:

- Compare the increase in energy dissipation capability due to the presence of foam as filler material;
- Compare the initial stiffness of the structure, to check whether the macro-scale initial elasticity exhibits significant discrepancies.
- Compare the enhancement in the plateau stress for different sample sizes.

In Figure 1.19(b) the TEA per unit cell is almost independent of the number of cells when considering the 8-cell and 27-cell structures, implying that the structure behavior does not change with size. The effect of the

foam-filling technique is therefore similar for all configurations, enhancing the energy absorption capability on average by 17%.

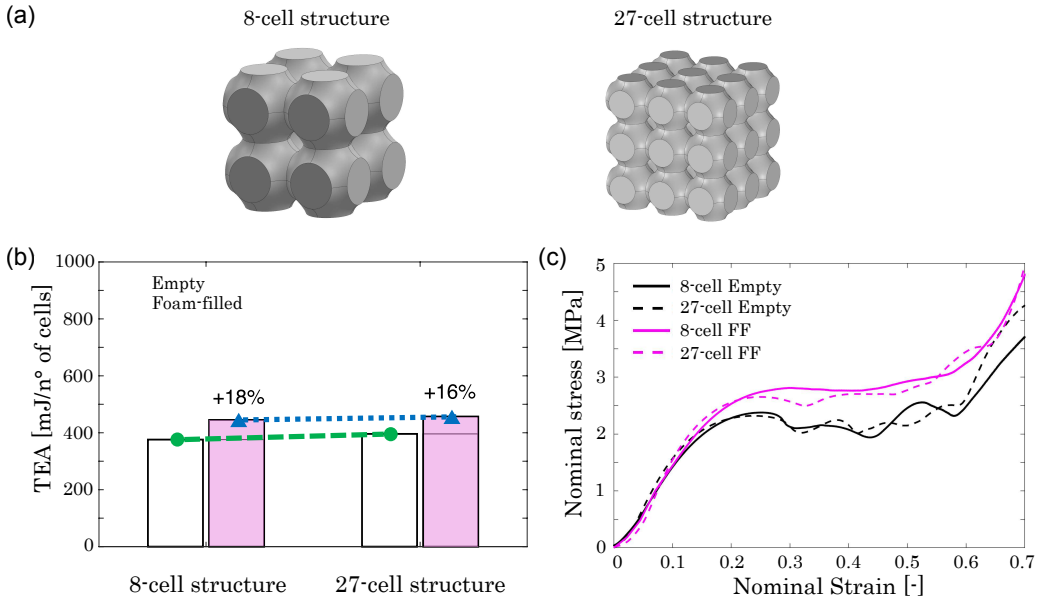

Figure 1.19: Investigation on the sample size effect: a)Samples with different number of cells; b)Comparison between energy absorption capabilities; c)Comparison between stress-strain curves.

To obtain the initial stiffness K_0, the cross-head displacement in the test direction and the reaction forces measured by the load cell are considered:

$$K_0 = \left.\frac{dP_c(z)}{dz}\right|_{(\epsilon=0.05)} \tag{1.9}$$

where P_c is the total compressive load. Differentiation of $P_c(z)$ is performed from 0.05 strain onwards to neglect the initial part where the elastic behavior is not linear due to inaccuracies in the sample geometry resulting from the printing process. The initial stiffness is found to be constant across different sizes, with structures behaving as linear elastic springs, see Figure 1.19(c).

To obtain the stress-strain curve of the overall compressive response, the nominal compressive stress $\sigma_{N,c}$ and the nominal compressive strain $\epsilon_{N,c}$ are defined as follows:

$$\epsilon_{N,c} = \frac{-u_c}{h_0} \qquad \sigma_{N,c} = \frac{P_c}{A_{0,eq}} \tag{1.10}$$

where u_c represents the nominal displacement, h_0 the initial height of the structure, and $A_{0,eq} = V_L/h_0$ the equivalent cross-sectional area of the structure, obtained dividing the lattice volume $V_L$by the structure initial height. The plateau stress is proved to be independent of the number of cells, with increases in performance also observed for larger structures upon foam injection, see 1.19(c). The average plateau stress in the FF configuration, defined as the mean of the plateau stress of 8-cell and 27-cell structures, is about 30% higher than that of the empty configuration. This is an encouraging result, as it extend the beneficial effect of the foam to periodic cellular structures, overcoming any size limitations.

Finally, the energy absorption performance of the meta-material studied in this work, both in empty and FF configuration, is compared with that of other lattices, cellular solids, and other engineered materials commonly available in literature.

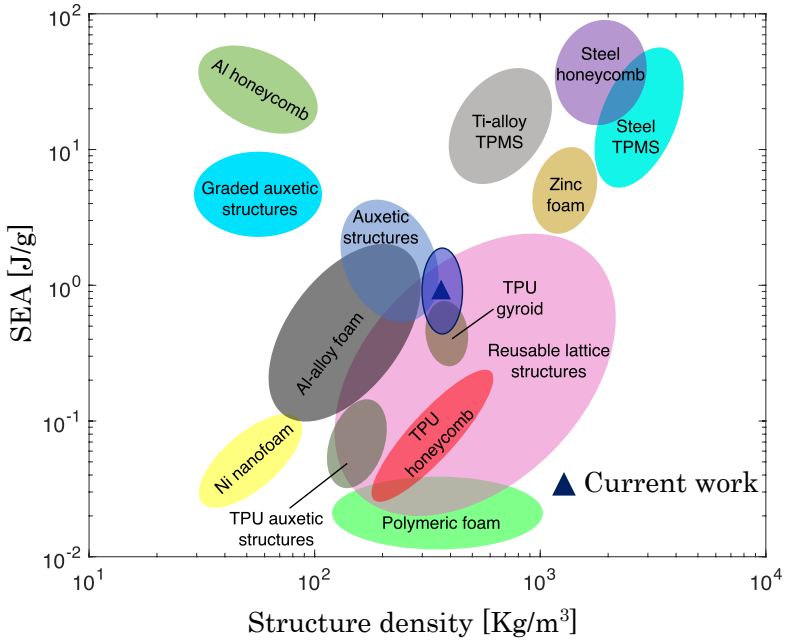

Figure 1.20: Map of the SEA as function of the structure density for reference works in literature

Figure 1.20 reports the SEA as function of the structure density: data obtained within the present study falls at the top of the region for nonmetallic materials, confirming the advantages of such structures.

In conclusion, the main findings of this section allow to state that filling thin-walled structures with a secondary foam-like material leads to an increase in compressive performance thanks to interaction between the two constituents, combining the good properties of additively manufactured lattices with the functional effect of PU foam. Foam-filled periodic cellular structures exhibit more uniform and regular deformation when subjected to compression, contrasting the buckling of some cells, which is responsible for a drop in strength of the original empty structures.

Finally, fields of interest for the developed cellular composite are not limited to structural engineering, which takes advantage of the enhanced energy absorption capability and the avoidance of instability phenomena. From a material point of view, the proven biodegradability combined with good mechanical behavior and printability of PBAT polymer could pave the pathway to new applications for 3D-printed mechanical meta-materials. This could include, for example, energy absorbers and dampers within food packaging industry to facilitate transition toward more environmentally sustainable production, or biodegradable scaffolds for tissue regeneration in the bio-mechanics field.

1.3 Fluid-filling

In the previous section the positive outcomes obtained from foam-filling cellular structures have been deeply investigated. The technique is inspired by biological structures found in the animal world and is proved to be useful also in various engineering disciplines for both structural and functional devices. The demonstrated benefits of this approach, consisting in combining a 3D-printed cellular geometry with a proper secondary material to develop multi-material structures with properties that are significantly more desirable than those of the single constituents, makes it definitely worth to be further studied.

Filler materials are not limited to foams: gels [13, 14] and silicons [15] have recently been employed inside additively manufactured lattice structure, displaying enhanced energy dissipation and constraint against instability, respectively.

Liquid secondary materials such as water have also been tested as fillers for 3D-printed cones under impact loads [16]; however, the proposed geometry was limited by lack of periodicity, making it impossible to extend this approach to non-stochastic cellular structures. Solid-liquid composites also exhibit interesting behavior under dynamic conditions. In this framework, a key role is played by Shear-Thickening-Fluids (STF). Within this family of non-Newtonian fluids, the shear stress is greater than proportional to the shear rate, with the viscosity consequently not constant but depending significantly on the applied shear rate. The material strength drastically increases as the critical shear rate is reached due to a thickening-hardening phenomenon within the fluid. This phenomenon underlies the adaptive behavior of dilatant fluids, making them ideal candidates for advanced functional applications where the dynamic response is ruled by stimulus received by the liquid [17, 18].

The state of the art in engineering field is often dedicated to applications in safety, where STF-impregnated fabric shows enhanced performance against penetration and ballistic impact. Sandwich panels with STF-filled

cores have been developed to enhance the impact resistance of composite materials [19, 20, 21], as well as STF-filled honeycombs [22] and lattices [23]. STF have been also integrated in closed-cell PU foams [24], focusing on the STF effect on the foam cell morphology and the composite mechanical performance. In [25] a sandwich composite combining PU foam skeleton with STF is presented to investigate the interaction between the two constituents Also origami structures have been combined with STF: in [26] a partially filled Miura-Ori geometry is developed to obtain increased crashworthiness; a Kresling geometry is filled with STF in [27] to obtain higher yield strength and lower peak force.

Despite the quantity of literature reporting positive experimental outcomes within this field, a more in-depth analysis of the coupled fluid-structure dynamic behavior is required. To this end, the previously discussed walled Schwarz-Primitive TPMS cellular structure is now filled with STF and experimentally and numerically tested under low-velocity impact loads. This section therefore aims to provide a fuller understanding of the adaptive response which characterizes STF-filled composites, which is necessary at the design stage to tune the mechanical response of a given structure in line with application requirements to obtain the maximum beneficial effect from adoption of such bi-phase meta-materials.

To prepare the shear-thickening fluid, hydrophilic SiO_2 nano-particles (12 nm average primary particle size) are dispersed in a liquid matrix of Poly-Ethylene Glycol (PEG - molecular weight Mn=200). Figure 1.21 presents a schematic of the fabrication process.

A beaker containing PEG is maintained in constant centrifugal motion by a mechanical mixer (550 rpm rotational speed) while nano-particles are slowly added to it. An ultrasonic bath treatment (45 kHz frequency) is used at regular time intervals to both facilitate homogeneous particle mixing within the solution and avoid the appearance of dry gel-like regions which irreversibly compromise the specimen preparation. The whole process is performed at room temperature (20°C) to avoid a temperature-induced gelation transition of the PEG/SiO_2 solution.

Fluids with different silica mass fractions of 10%, 12%, 17% and 20% are

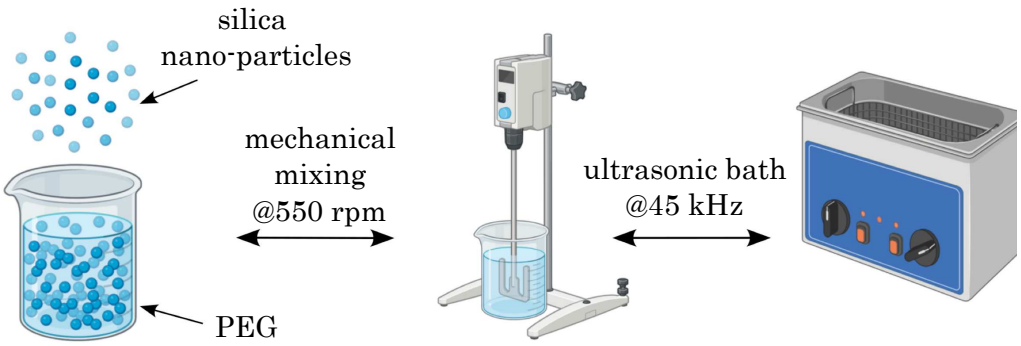

Figure 1.21: Shear-thickening fluid preparation

prepared, in order to understand the influence of the silica weight fraction $wt\%$ on the rheological properties of the solution and consequently determine the most suitable concentration for this work. To characterize the mechanical response of the fluid, rheological tests are performed with an Anton Paar MCR 101 rheometer (Figure 1.22(a)) with plates of diameter 25 mm, a gap between the plates of 1.0 mm and a controlled temperature of 20 °C (see Figure 1.22(b)). The shear rate range is set to 0-200 s^{-1}. Rheological curves are shown in Figure 1.22(c).

For low silica nano-particle $wt\%$, no shear-thickening behavior is observed, confirming a minimum threshold value of about 10 $wt\%$: the lightest line (10 $wt\%$) exhibits only slight shear-thickening. However, hardening trends are more evident when higher silica mass fractions are considered, such as 12 $wt\%$, 17 $wt\%$ and 20 $wt\%$. In addition, the maximum value of viscosity (about 1.76, 15.9, 52.7 and 510.0 Pa*s, respectively) is strongly dependent on the silica fraction.

Figure 1.22(d) highlights how the viscosity gain, defined as the ratio of peak viscosity η_{max} to initial viscosity η_0, is strongly affected by the percentage of nanoparticles, demonstrating the effectiveness of fluid shear thickening behavior, with increases in viscosity of more than 10000% achieved. High viscosity gain is extremely beneficial for a more remarkable adaptive behavior and for energy dissipation related with viscous phenomena. In addition, the thickening critical shear rate is another important parameter to be consid-

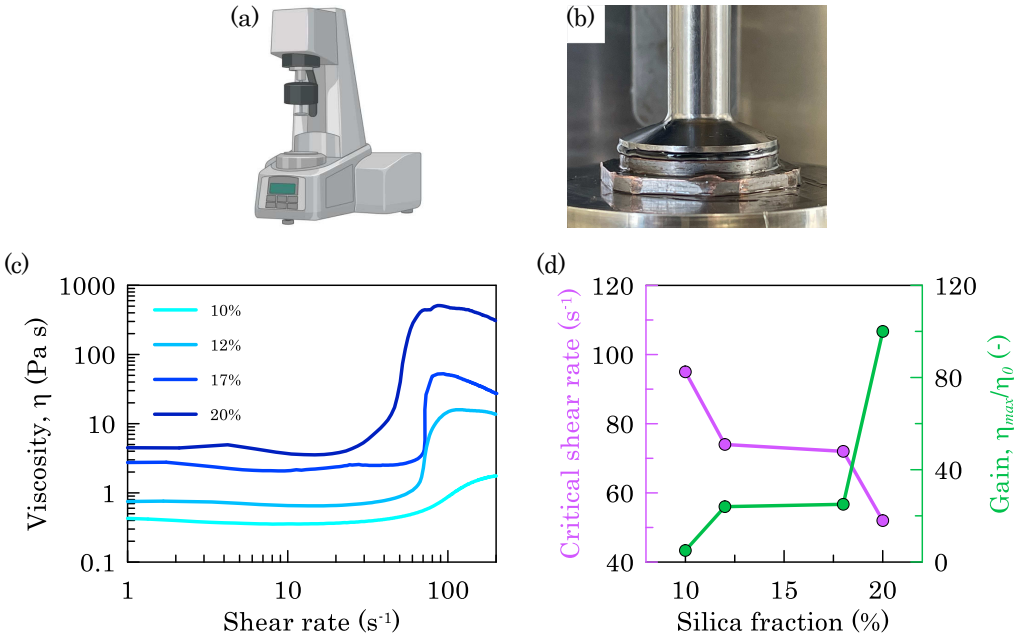

Figure 1.22: STF rheological characterization: a)Rotational rheometer; b)Detail of the parallel plates; c)Viscosity as a function of shear rate; d)Influence of silica weight fraction on the peak viscosity η_{max} and the viscosity gain η_{max}/η_0.

ered at the design stage: this allows to tune the adaptive fluid behavior depending on the shear rate range for a specific application. Based on this, 20 $wt\%$ is chosen within the present work as the most representative adaptive behaviour of the fluid, and therefore employed as the filler for the bi-phase samples to be tested. The periodic cellular structure, previously defined in Section 1.1, is manufactured via FDM technology using a commercial Thermoplastic Poly-Urethane (TPU) filament.

To perform the filling process, a pause is set in the G-code file used for printing to allow the structure to be completely filled before resuming printing to close the upper faces with the top layers. Figure 1.23 schematizes the fabrication of the bi-phase composite.

A FE numerical model is developed to accurately investigate the interaction between the liquid and the solid part: a further comprehension of the underlying fluid-structure-interaction is necessary to understand the way the bi-phase composite mechanically behaves, and consequently to optimize its

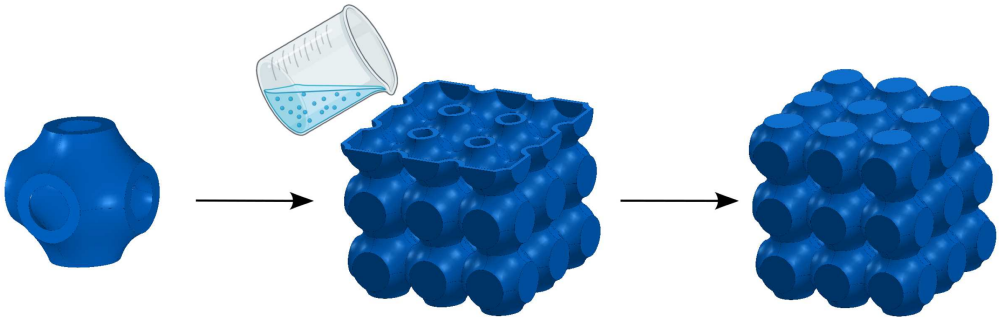

Figure 1.23: Bi-phase composite fabrication process

response depending on the application. The development of the FE model required accurate models of the materials making up the composite structure.

To characterize the structure material, five tensile test specimens with standard geometry (type 5A in UNI EN ISO 527) were produced with the same printing parameters employed for production of the composite structures. During tensile tests, pneumatic grippers were adopted to avoid possible slipping of the sample when subjected to large deformation. The cross-head displacement rate was set to 10 mm/min for all tests. Based on its tensile response (experimental setup shown in Figure 1.24(a)), TPU exhibits hyper-elastic behavior.

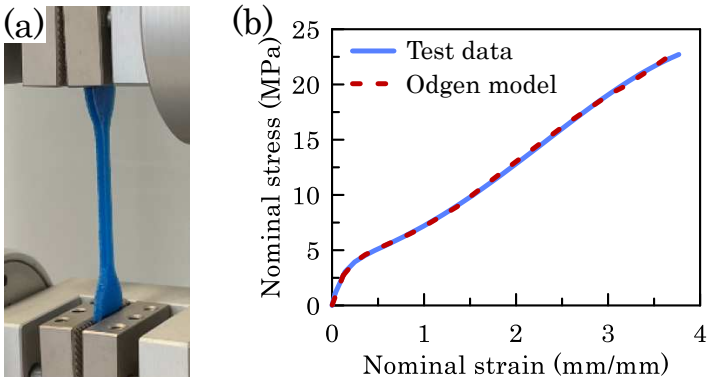

Figure 1.24: TPU mechanical characterization: a) Tensile test setup; b) Stress-strain test data and Odgen constitutive law.

Ogden strain energy density function of 3^{rd} degree is adopted, as this formulation is found to provide the best fit with experimental data, as shown in Figure 1.24(b). The strain energy density function is defined by Equation(1.11): a table with all the coefficients follows (Table 1.2).

$$U = \sum_{i=1}^{N} \frac{2\mu_i}{\alpha_i^2}[\lambda_1^{\alpha_i} + \lambda_2^{\alpha_i} + \lambda_3^{\alpha_i} - 3] + \sum_{i=1}^{N} \frac{1}{D_i}(J_{el} - 1)^{2i} \tag{1.11}$$

Table 1.2: TPU Ogden model coefficients

	μ_i	α_i	D_i
i=1	2.7067	-0.9858	0
i=2	-6.9373	4.0601	0
i=3	16.7480	-7.9081	0

Two fluids are considered for numerical modelling of liquids, which are water and the shear thickening PEG-SiO_2 suspension. The hydrostatic behavior of these fluids is described by the Mie-Grüneisen equation of state (EOS) in Eq.(1.12), where p is the pressure, E is the internal energy per unit reference volume, and $x = 1 - (\rho_0/\rho)$ with ρ_0 and ρ the initial density and current density, respectively.

$$p = \frac{\rho_0 C_0^2 X}{(1 - sX)^2}(1 - \frac{\Gamma_0 X}{2}) + \Gamma_0 E \tag{1.12}$$

where C_0 is the speed of sound through the material medium, Γ_0 is the Grüneisen parameter and s is the linear Hugoniot slope, defined as the coefficient of linear relationship between the linear shock velocity U_s and the particle velocity U_p. Values of all parameters are reported in Table 1.3.

Table 1.3: Equation-Of-State parameters

	$\rho_0[T/mm^3]$	$C_0[mm/s]$	$s[-]$	$\Gamma_0[-]$
Water	1.0 e-9	1.48 e+6	1.43	2.50
STF	1.6 e-9	2.10 e+6	3.75	0.80

To comprehensively characterize the mechanical behavior of a fluid, it's

necessary to consider both its hydrostatic properties and the constitutive equation that governs its viscous response. In the case of non-Newtonian fluids, viscosity is not constant but varies depending on the shear rate experienced by the fluid. For shear thickening fluids, three distinct rheological behaviors can be observed as viscosity changes with shear rate, see Figure 1.25. Initially, there is a mild shear-thinning phase for shear rates below a critical point. This is followed by a pronounced shear-thickening phase near the critical shear rate, where viscosity sharply increases by over an order of magnitude. Finally, the fluid returns to a shear-thinning behavior.

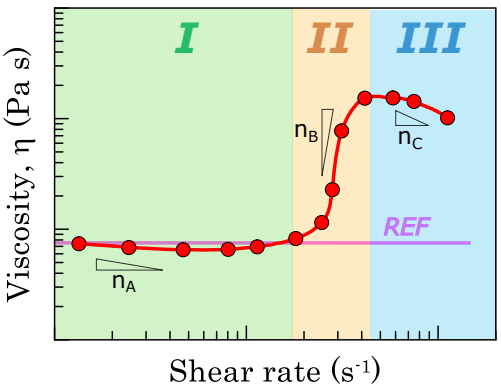

Figure 1.25: Viscosity regions in shear-thickening fluid

Based on this trend, a piece-wise function was introduced to define the three stages separately. Power-law functions were found to accurately fit viscosity trends observed during rheological tests. Equation (1.13) shows the function implemented to characterize the viscous behavior of the fluid, where $\dot{\gamma}$ is the shear rate $[s^{-1}]$, a, b, c are coefficients [Pa·s], and n_i are the flow behavior indexes [-].

$$\eta(\dot{\gamma}) = \begin{cases} a \cdot (\dot{\gamma})^{n_A - 1} & for \quad \eta_{\min} < \eta < \eta_{\max} \\ b \cdot (\dot{\gamma})^{n_B - 1} & for \quad \eta_{\min} < \eta < \eta_{\max} \\ c \cdot (\dot{\gamma})^{n_C - 1} & for \quad \eta_{\min} < \eta < \eta_{\max} \end{cases} \tag{1.13}$$

When $n_i < 1$, the fluid exhibits shear thinning, with the viscosity de-

creasing with increasing shear rate. When $n_i > 1$, the fluid exhibits shear thickening, with the viscosity increasing with shear rate. When $n_i = 1$, the fluid is a Newtonian fluid, with viscosity independent of the shear rate. Within the commercial Finite-Element suite Abaqus/Explicit, the viscosity function is provided via a User Subroutine code.

Various methods exist for numerically simulating the dynamic behavior of fluids using the Finite-Element approach. In this study, the Coupled-Eulerian-Lagrangian (CEL) method was employed, which integrates both Lagrangian and Eulerian components within a single analysis. The Lagrangian elements are represented by deformable bodies with meshed material volumes, while the Eulerian elements are defined by control volumes through which material flows within a fixed, predefined mesh. Figure 1.26 illustrates this technique. This method is highly effective in capturing key fluid dynamics phenomena, making it well-suited for fluid-structure interaction simulations.

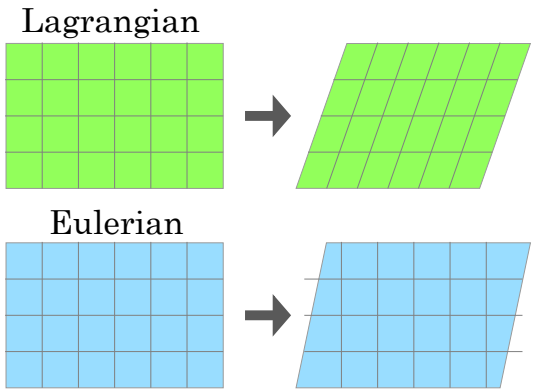

Figure 1.26: Coupled-Eulerian-Lagrangian methodology

Before designing the finite-sized cellular meta-material, it is essential to study the mechanical behavior of both constituent materials and how they interact. Initially, the focus is on examining the interaction between the two phases within a filled unit cell, serving as a proof of concept for the adaptive properties of the composite under dynamic conditions. Once this has been

validated, the approach is then expanded to a larger, finite-sized sample. This step is crucial for ensuring the solid-liquid composite is properly designed to withstand the anticipated dynamic stress field for a specific application.

In low-velocity impact tests, the total moving mass is accelerated by gravity g towards the test specimen. By lifting a mass m to a given height h, a certain quantity of potential energy $E_P = mgh$ is attained. During acceleration, all the potential energy is converted into kinetic energy $E_K = \frac{1}{2}mv^2$, which is maximum immediately prior to impact. Impact experiments are performed at different impact energies to compare the effects of different filler materials, justifying the use of a dilatant fluid based on its promising mechanical response. The adaptive properties of the bi-phase composite are also shown to be very useful in many applications due to the tunability of the stiffening threshold through control of the shear rate field under actual working conditions.

The external solid structure is defined within the Lagrangian framework, while the fluid filler is free to flow within the defined control volume. A **general contact* interaction is employed with friction coefficient of 0.2 and normal hard contact. Both plates are defined as analytically rigid surfaces. The inertia and initial velocity are assigned to the top plate, while the bottom one is fixed with an (*encastre* constrain). Gravity is applied to all parts within the simulation. The cellular structure is meshed with three-dimensional S4R shell elements, which are computationally less demanding than solid elements when considering thin-walled structures. The fluid is instead meshed with three-dimensional 8-node EC3D8R elements. Fig. 1.27(a) schematically shows the modeled fully-filled unit-cell.

The model is tested for two different values of impact energy, maintaining the dropped mass m constant (0.3 kg) and varying the impact velocity v_0 from 0.5 m/s to 2.2 m/s.

Three different configurations are evaluated: air-, ref-, and STF-filled composites, respectively, with "ref" referring to a Newtonian liquid employed for comparison, characterized by constant viscosity equal to the initial viscosity of the shear-thickening fluid (η corresponding to zero shear rate), as shown in Figure 1.25. This approach is employed to highlight the effect of

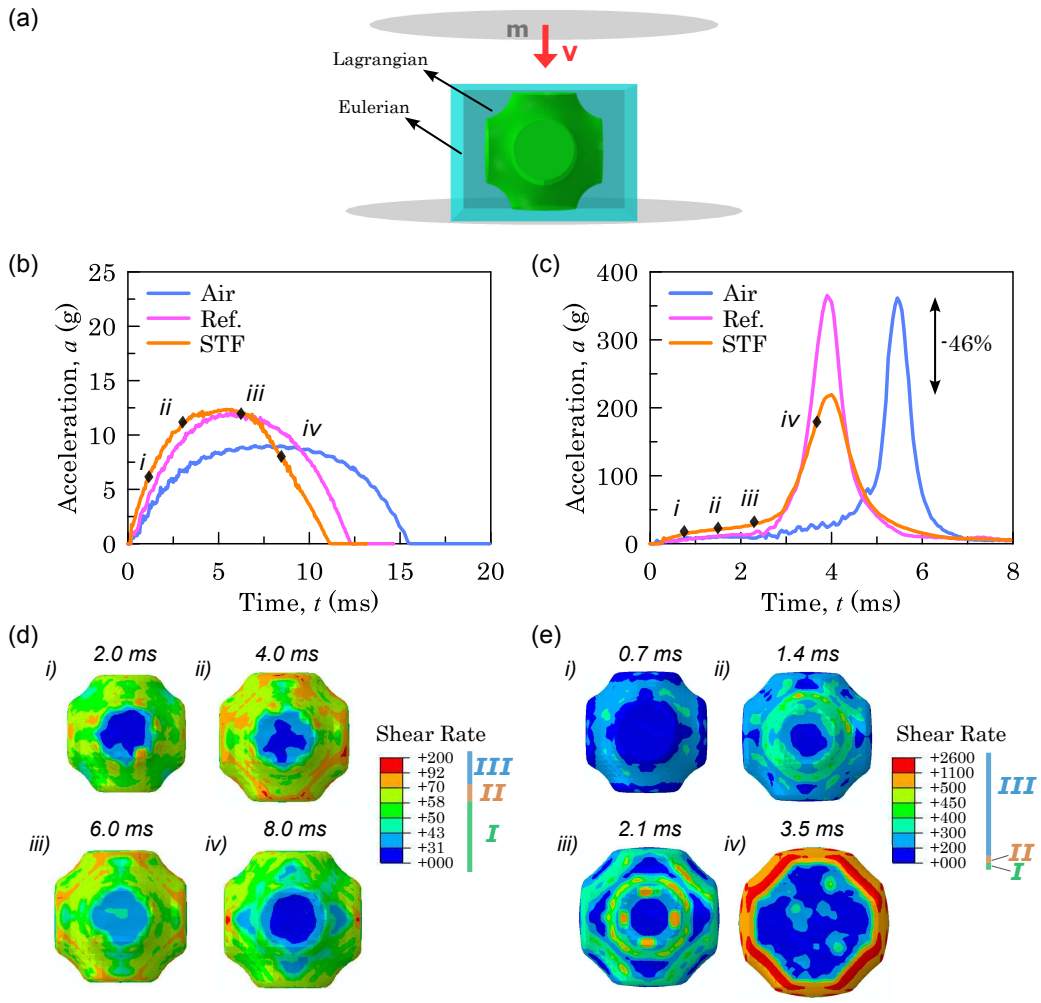

Figure 1.27: Proof of adaptive mechanical behavior: a)Unit-cell FE model; b-c)Acceleration of the plate, velocity 0.5 and 2.2 m/s, respectively; d-e)Shear-rate field in the STF part, velocity 0.5 and 2.2 m/s, respectively.

the adaptive response of the STF compared to non-adaptive fluids.

Figure 1.27(b)-(c) shows the plate acceleration during impact, highlighting the adaptive response. At lower speeds, the two curves are nearly identical, but at higher speeds, there is a marked difference between them. Additionally, the presence of a liquid phase (both 'ref' and STF) within the composite results in higher acceleration compared to the air-filled configuration at low velocities. However, the effect reverses at higher velocities. While

the 'ref'-filled composite reaches acceleration values similar to the air-filled setup, the STF-filled composite notably smooths the acceleration profile.

The explanation for these results is depicted in Figure 1.27(d)-(e). At low velocities, only a small percentage of fluid elements reach the critical shear rate, limiting the stiffening effect, especially in region II compared to region III. As a result, the stiffening is confined to a small portion of the liquid, allowing the STF to flow and follow the shell deformation. At higher velocities, however, the critical shear rate is quickly exceeded after impact (*i*-*ii*), causing a significant portion of the STF to thicken, which inhibits deformation. As the deformation progresses, high shear rates develop in the top region due to the striker's contact, leading to large deformations and immediate fluid compression. The liquid near the cell walls also experiences high shear rates, as it is constrained by the shell structure, forcing the fluid to deform (*iii*). This phase can be described as the stress diffusion stage. During the following interaction phase (*iv*), the fluid undergoes expansion due to the impact, while fluid regions near the cell walls are obstructed. These opposing effects counterbalance each other, leading to stress relief in the central region. Consequently, part of the impact energy is absorbed as internal energy through flow dispersion and activation of STF stiffening, resulting in a distinct dynamic response.

To evaluate the impact properties of the 27-cell bi-phase composite, dynamic compression tests are performed with an AD-Engineering drop-tower machine while recording deformation with a Phantom v1840 ultrahigh-speed camera at 3300 frames per second. The striker is a 40 mm diameter plate of mass 0.09 kg and it is connected to a ram of mass 4.75 kg, generating a total moving mass $m = 4.84$ kg. The impact velocity is verified with a photocell: the difference between the theoretical ($v_{th} = \sqrt{2gh}$) and actual (v_0) velocities is due to the contribution of friction between the ram and guides during the fall.

Table 1.4 summarizes the drop height, impact energy and initial velocity of all experiments that are carried out.

The impact force $F(t)$, measured by the load cell, is acquired during each test. Equation(1.14) shows how the displacement profile $u(t)$ was obtained.

Table 1.4: Experimental plan for impact tests

Drop height [cm]	Impact energy [J]	Initial velocity [m/s]
25	6	1.6
45	11.5	2.2
70	22.5	3.1

$$u(t) = v_0 t + \iint \frac{F(t)}{m} dt \tag{1.14}$$

The Crushing Force Efficiency (CFE) is an important parameter to be evaluated in the impact behavior of structures, defined as the ratio of the average force to the peak force (Equation (1.15)).

$$CFE = \frac{\int_0^{u_{max}} F du}{u_{max} F_{peak}} \tag{1.15}$$

Based on findings relating to the unit cell, a series of experiments is conducted on tessellated structures consisting of 27 cells (setup shown in Figure 1.28(a-c)). Lattices filled with air, water, and STF are tested under three different impact energy levels (corresponding to varying impact velocities) to assess the dynamic behavior of these composites.

The experimental results in Figure 1.28(d) demonstrate that filling the lattice structure with a shear-thickening fluid effectively reduced the peak force F_{peak} during impact by up to 58%, leading to a 180% increase in the CFE parameter. The peak force also shifted to earlier times due to reduced sample penetration. Additionally, both the rebound velocity and maximum compressive displacement were influenced by the properties of the filler and its interaction with the structure.

The air-filled configuration showed the highest rebound velocity and maximum compressive displacement (U_{max}), while the STF-filled composite had the lowest values. Water-filled structures showed intermediate performance, with a 23% reduction in F_{peak} and a 27% increase in CFE. Figure 1.28(e) summarizes the complete test results.

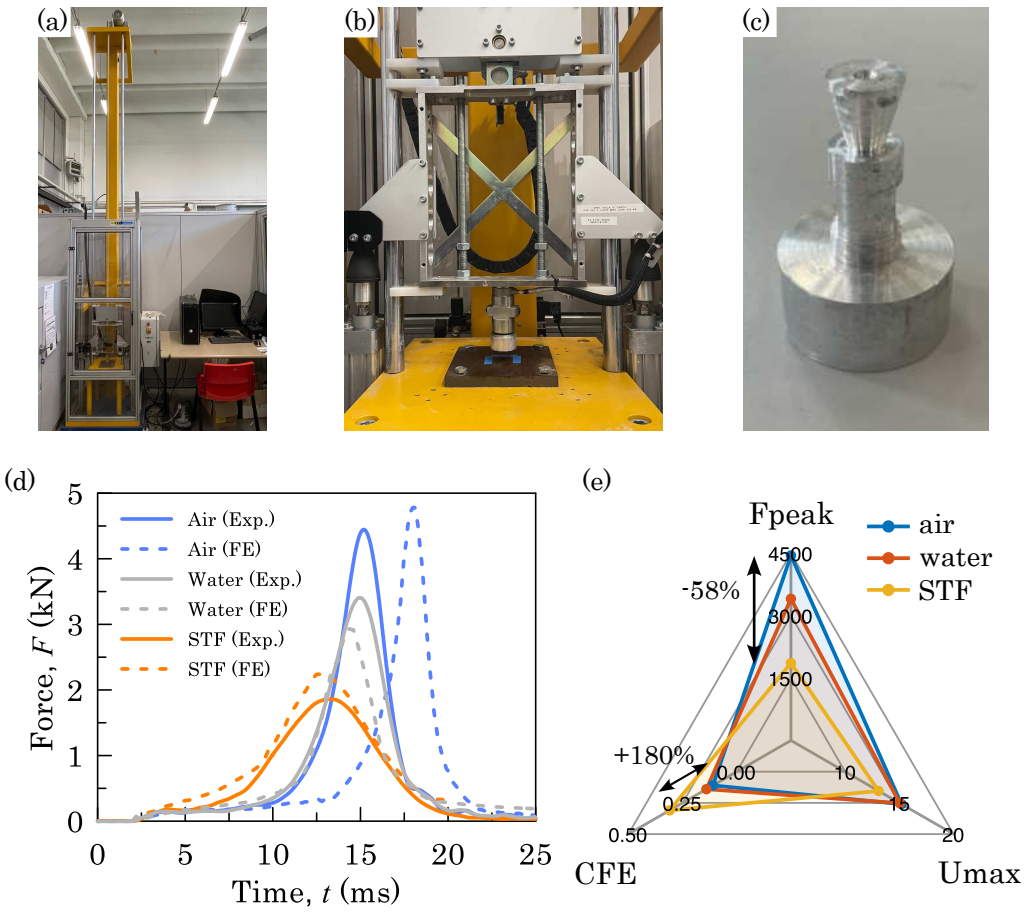

Figure 1.28: Impact response of 27-cell structure: a)Weight drop-tower setup; b)Ram; c)Striker; d)Impact force, velocity = 2.2 m/s; e)Impact parameters.

Camera frames at different stages of compression U/U_{max} (Figure 1.29(a-b)) show regular deformation throughout the whole structure for both air- and STF-filled configurations, respectively. Alignment between the experimental and numerical deformation provides additional validation of the FE model, allowing evaluation of the stress field within the lattice part during its deformation.

At the onset of deformation, the highest stresses are concentrated in the necking regions between adjacent cells, both vertically and horizontally, due to the smaller cross-sectional area and increased wall curvature in these regions. As deformation increases, stress concentration in the vertical necking

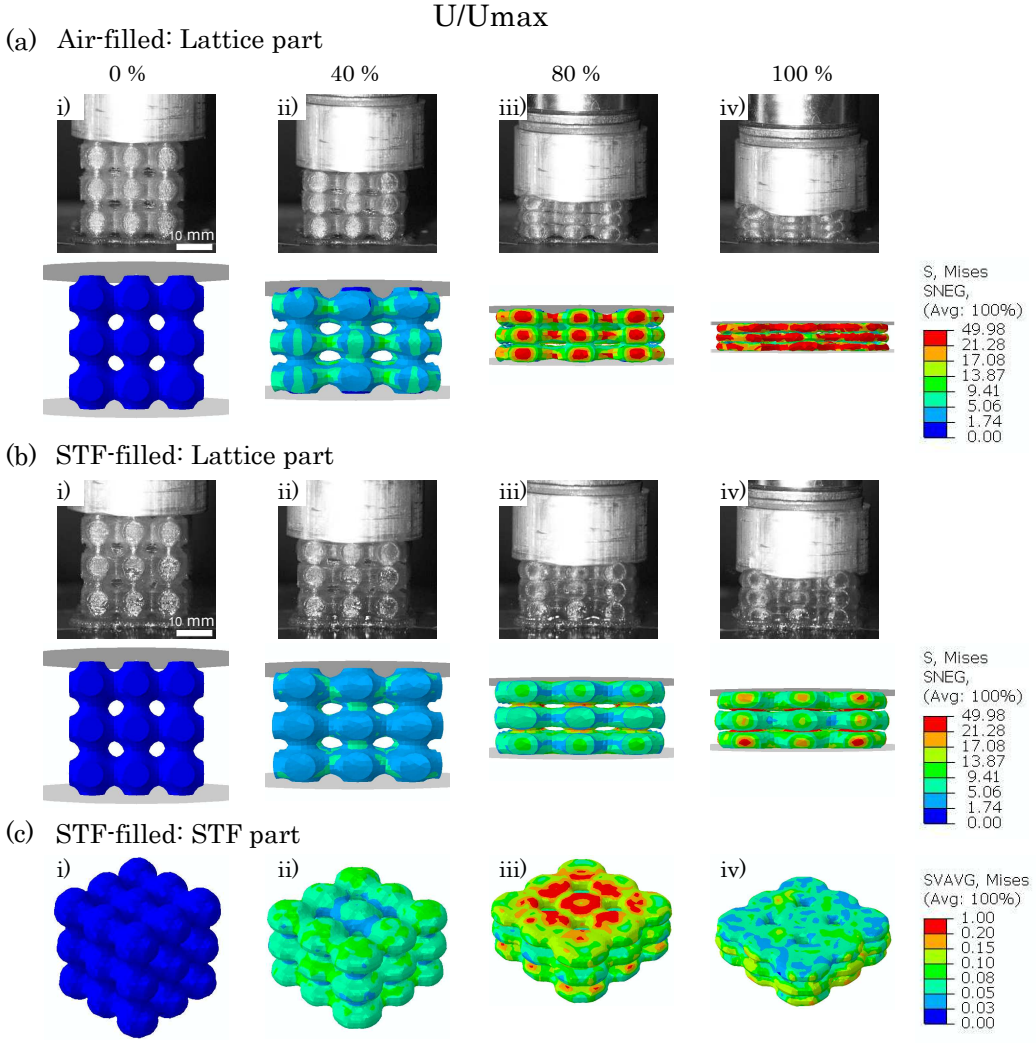

Figure 1.29: Deformation mechanisms and stress field distribution: a)Air-filled structure; b)STF-filled structure (solid phase); c)Liquid phase.

regions becomes more pronounced as the structure undergoes densification. This is accompanied by localized high bending stresses in the outer walls. The presence of the viscous filler greatly reduces stress distribution and aids in energy dissipation, acting as a damper and therefore helping to stabilize the structure by preventing instability due to its thin walls.

To analyze the fluid-structure interaction, Figure 1.29(c) presents the volume-averaged stress within the STF inside the structure's cavity. Shortly after impact (*ii*), the STF flows in response to the structure's deformation,

moving into the horizontal necking regions between cells. The reduced cross-sectional area increases the shear rate, triggering the STF's thickening behavior. This localized stiffening blocks further flow between adjacent cells, confining the STF to a single unit cell, where it gradually responds to the deformation imposed by the external shell, resulting in viscous energy dissipation. When severe deformation begins (*iii*), the striker compresses the top wall of the structure, and the fluid resists radial expansion, causing peak stress values in the upper region of the liquid phase.

At this point, the relationship between crushing parameters and impact velocity must be explored, to quantify the adaptivity in the mechanical response. The impact velocity is, indeed, responsible for the impact duration and initial strain rate the structure undergoes when hit. To do so, tests at different drop heights are performed (Table 1.4).

For the air-filled configuration, only the TPU constitutive law plays a role in the dynamic behavior: consequently, the peak force increases with velocity, together with the maximum penetration, while the CFE decreases.

The behavior of bi-phase liquid-filled composites becomes more complex, as the strain rate influences not only the material properties but also the shear rate distribution within the liquid and, for shear-thickening liquids, the fraction of the fluid that surpasses the critical stiffening threshold. At a velocity of 1.6 m/s, the F_{peak} values for air-, water-, and STF-filled structures are similar, but they diverge significantly at higher impact velocities (2.2 and 3.1 m/s). The air-filled structure shows the steepest increase, followed by the water-filled structure, and finally the STF-filled composite, as shown in Figure 1.30(a).

Figure 1.30(b) illustrates that the CFE for air- and water-filled samples behaves similarly, decreasing sharply until around 2 m/s, after which it stabilizes for air and slightly increases for water due to the dynamic damping effects of liquids at higher speeds. In contrast, the STF-filled composite maintains an almost constant CFE value over the entire range of velocities, thanks to the significant contribution of viscous dissipation from the stiffened fluid, which helps smooth the force profile during impact and sustain a relatively high CFE.

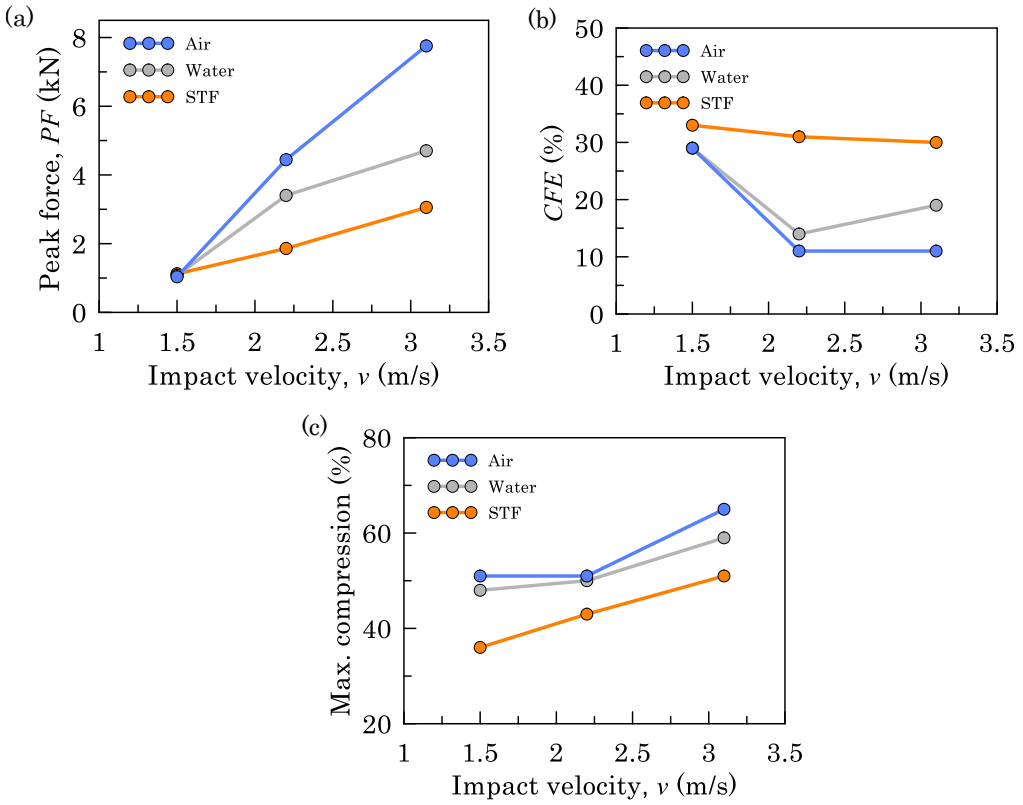

Figure 1.30: Influence of impact velocity on crash parameters: a)Peak force; b)Crashing Force Efficiency CFE; c)Maximum compression.

These patterns highlight the adaptive nature of the bi-phase meta-material, demonstrating that the overall resistance to impact loads is influenced by the unique properties of the STF, which are determined by the fluid's response to external stimuli, as well as the interaction between the two components. Maximum compression increases with velocity (Figure 1.30(c)), with the STF-filled composite showing the lowest compression, as expected.

After extensive experimental and numerical tests, the energy absorption capability of the proposed bi-phase adaptive cellular structure is evaluated. As a matter of fact, during the impact only a fraction of the impact energy is absorbed by the sample, with the remaining quantity leading to rebound of the striker. The absorbed energy EA is calculated in line with Equation (1.16), where v_r is the rebound velocity after impact.

$$EA = \int_0^{u_{max}} F du \quad - \int_{u_{max}}^{0} F du = \frac{1}{2} m(v_0^2 - v_r^2) \tag{1.16}$$

To evaluate the energy absorption behaviour of samples, the coefficient of restitution e is introduced, defined in Equation (1.17), ranging from 1 for perfectly elastic behaviour to 0 for perfectly inelastic behavior. E_r represents the rebound energy, while E_0 is the total impact energy.

$$e = \sqrt{\frac{E_r}{E_0}} \tag{1.17}$$

Figure 1.31(a) illustrates the load versus displacement curves observed during impacts with various fillers. By integrating the curves according to Equation (1.16), it is evident that the impact energy remains constant across all samples, as it is determined solely by the mass of the ram and the height from which it is dropped. In contrast, the rebound energy is influenced by the properties of the filler and its interaction with the surrounding structure during deformation. The rebound energy, defined as the energy loss after achieving maximum compression (refer to Figure 1.31(b)), is subtracted from the impact energy to calculate the energy absorbed by the bi-phase composite. This allows for an assessment of the energy absorption capability relative to the initial strain rate. The restitution coefficient e is displayed in Figure 1.31(c) for each conducted impact test. The results highlight the advantageous role of using an adaptive fluid as a filler. For initial strain rates below the STF's stiffening threshold, the rebound energy values are comparable to those of structures filled with air or water. However, at higher strain rates, the e value shows a negative slope for the shear-thickening fluid composite, indicating a larger proportion of absorbed energy, unlike the nearly constant values observed for the water-filled composite and the increasing values for the air-filled structure, which correspond to a significantly reduced fraction of absorbed energy.

The advantages of incorporating a liquid medium into the meta-material are quantitatively illustrated in Figure 1.31(d), which shows the enhanced energy absorption of water- and STF-filled structures compared to air-filled

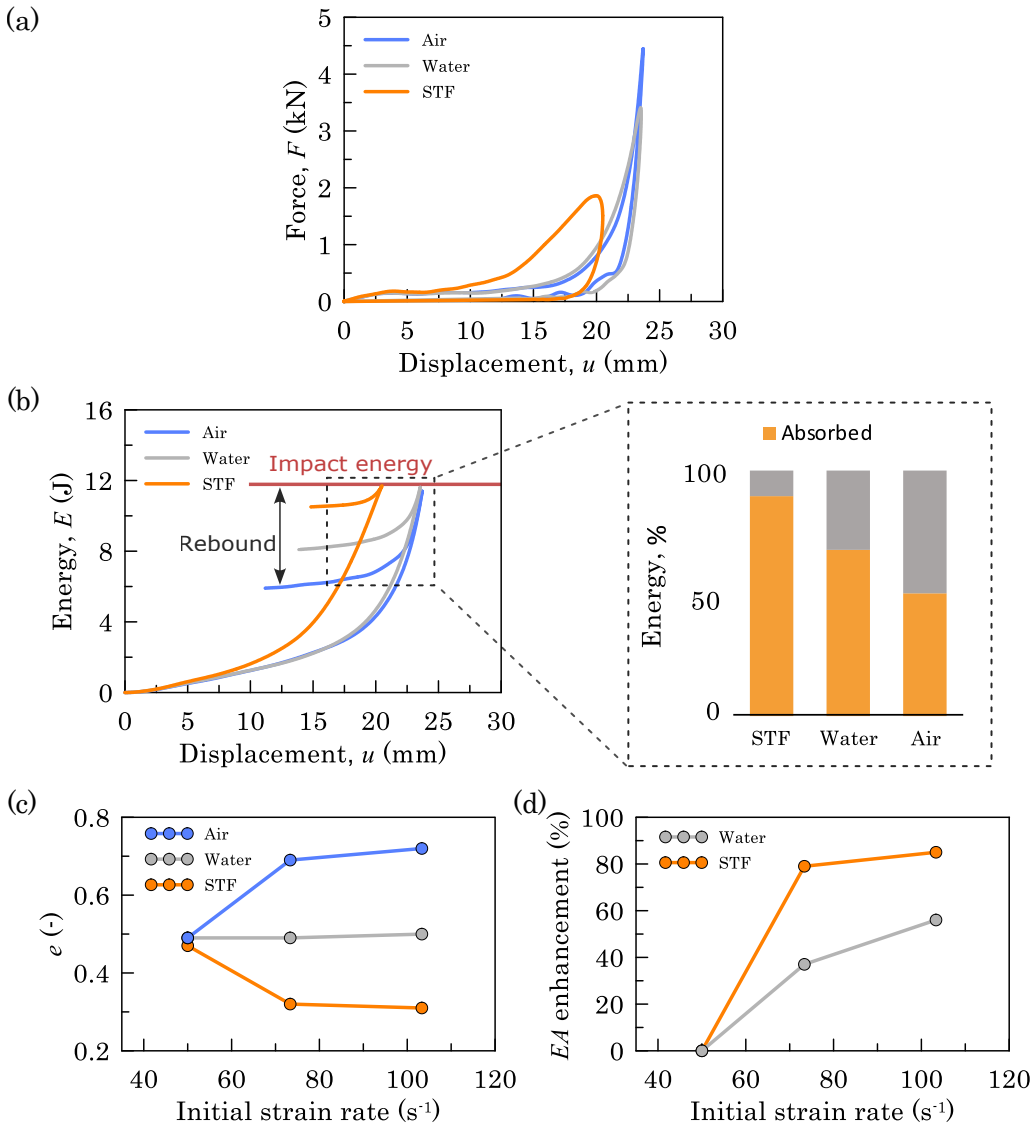

Figure 1.31: Energy Absorption properties for different fillers: a) Impact force vs. displacement, velocity = 2.2 m/s; b) Energy profile during impact; c) Coefficient of restitution e; d) Enhancement of EA capability.

ones as a function of the initial strain rate. Notably, the primary distinction between the two responses occurs at strain rates approaching the critical threshold for the shear-thickening fluid, where the behavior diverges significantly from that of a Newtonian fluid.

The graph in Figure 1.32 compares the EA performance of the bi-phase

meta-material developed in the present work with STF-composites presented in the literature; specifically, honeycomb and auxetic kirigami filled with shear-thickening gel [14], a STF-filled sandwich panel with PU-foam skeleton [25], bio-inspired sandwich structures with STF alternating PU foam cores [19], and STF-filled re-entrant auxetic lattice structures [23]. The outcomes of the present study exceed other works in the low initial strain rate region, confirming the promising behavior of the developed structure.

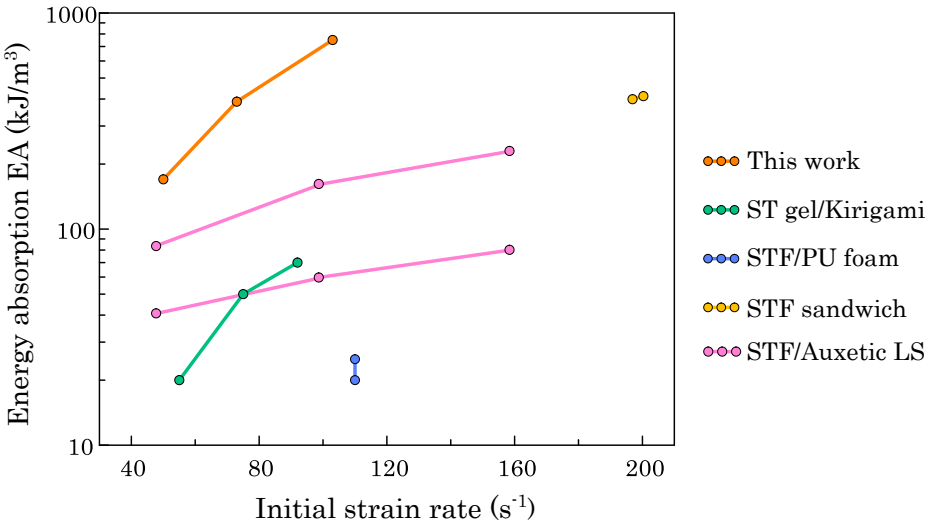

Figure 1.32: Comparison of impact energy absorption with reference similar works from literature [14, 19, 23, 25]

The 3D-printed TPMS structures filled with shear-thickening fluid is proposed as a novel flexible adaptive meta-material: owing to the unique rheological properties of dilatant liquids, behavior of the meta-material under dynamic compressive loads is ruled by interaction between the fluid and structure during impact. To resume the most promising findings, the force and acceleration profiles are notably smoothed in comparison to air- and water-filled structures, thanks to the viscous energy dissipation phenomena consequent to the hydro-cluster formation inside the fluid solution. The peak reduction reaches values of about 50%, and the energy absorption capability is found to be more than 85% enhanced.

These remarkable results lay the basis for new hybrid impact-resistant devices, re-designed in line with this concept to emphasize the adaptive shock-absorbing property. A wide range of applications is available, as the tessellation of a unit cell allows linear, planar, or spatial periodicity to be achieved when required, overcoming both size and geometric curvature constraints.

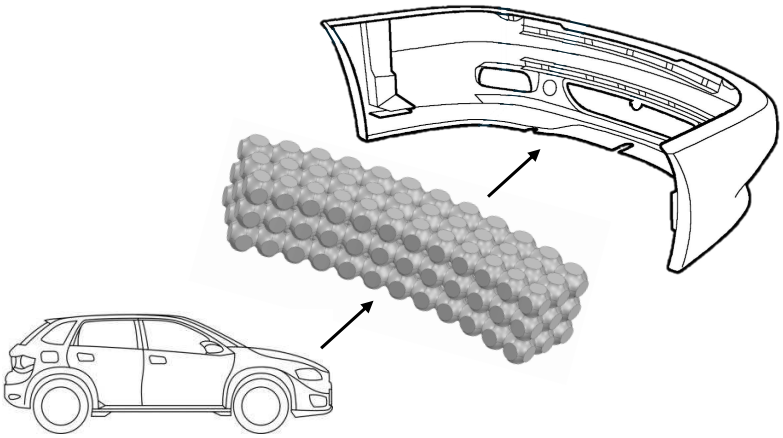

Figure 1.33: Using the bi-phase meta-material as a shock-absorber component for cars front bumper

The ability to mitigate acceleration spikes during impacts is a highly sought-after feature in protective devices for humans, as well as in wearable gear such as sports equipment and military armor. Figure 1.33 illustrates a potential application within a newly designed car bumper. While the advantages of reduced maximum penetration and the potential for re-use are notable, the significant reduction in peak acceleration transmitted to the driver (up to 85%) is particularly beneficial. This improvement positively influences crash test performance metrics, including the Acceleration Severity Index (ASI) and Theoretical Head Impact Velocity (THIV), as outlined by European standards.

1.4 Conclusions

The present chapter has investigated the effect of incorporating a secondary material on the mechanical response of thin-walled cellular structures. In particular, the developed idea concerns the investigation of structures characterized by a secondary material in a different physical phase than the one of the structure. The compressive behavior has been analyzed both in static and dynamic regimes: two different fillers have been therefore employed, to exploit the best response depending on the application.

For both configurations, foam-filled and shear-thickening-fluid-filled cellular structures, the enhanced performance is derived from the interaction between the two phases. The choice of the secondary material is properly evaluated to harness in a smart way the peculiar material properties, interacting with the advanced (potentially *ad-hoc*) geometry of the 3D-printed lattice structure.

In quasi-static regime, a polymeric foam used as filler inside the periodic structures leads to a more uniform and regular deformation of the whole structure when compressed; the overall load-bearing capacity, energy absorption capability, and plateau stress, are remarkably increased, placing the new composite meta-material in the top region of polymeric lattices in terms of performance.

In dynamic regime, the stf is characterized by energy dissipation phenomena and is consequently responsible of the significant reduction (about half of the value) of the peak force and peak acceleration taking place during impact loads. Also, the hybrid bi-phase cellular structure shows a very desirable enhancement (almost two times the initial value) in the energy absorption capability.

Future works will compare different TPMS and lattice geometries. This will aim at the evaluation of the foam contribution to the local deformation in bending- or stretch-dominated lattices, and of the local shear-rate field for the non-Newtonian fluid when subjected to flow inside the cellular architecture. Considering this last scenario, it will be possible to reverse engineer the

structure geometry at the design stage "tuning" the fluid flow to optimize the solid-liquid interaction depending on the expected dynamic load.

Moreover, thanks to the novel advancements in multi-material additive manufacturing technologies, new phases are already available as fillers for multi-phase cellular structures: examples include powders and other granular media to be studied.

Also, the multi-phase structures studied in this chapter are globally filled with the secondary material in a different phase. This because the lattice structure is globally walled to prevent leaks of the filler. New structures with locally walled unit-cells will allow a selective filling pattern, introducing a new degree of freedom during the fabrication that will pave the way to structures customized and optimized for the most desired behavior.

Mechanics and Failure Mechanisms of 3D-Printed Structures

The following articles have been extracted from the content of this chapter:

- **A. Corvi**, L. Collini, Combined RVE-Cohesive elements approach to the multi-scale modelling of FDM 3D-printed components, *Theoretical and Applied Fracture Mechanics*, 2023.
- **A. Corvi**, L. Collini, C. Sciancalepore, A. Kumar, Analysis and modelling of damage mechanism in FDM 3D-printed lattice structure under compression loading, *Journal of Mechanical Science and Technology*, 2023.

2.1 Overview on 3D-Printing

3D-printing, also referred to with the umbrella term Additive Manufacturing (AM), is the construction of a three-dimensional object from a CAD model or a digital 3D model. This contrasts with traditional subtractive manufacturing technologies, which rely on the removal of material from a bulk block, before achieving the final shape. Despite of the term gaining popularity in the 2000s, first recording of the additive manufacturing concept can be found in a U.S. patent from 1971 where J. F. Gottwald presented a continuous inkjet metal material device to form a removable metal fabrication on a reusable surface for immediate use. In 1980 additive methods for fabricating three-dimensional plastic models with photo-hardening thermoset polymer have been invented, anticipating the appearance of stereolitography (SLA), patented in 1984. While owning a 3D printer in the 1980s cost upwards of USD300,000, in 2020 decent quality printers can be found for less than USD300 for entry-level machines, allowing most people to enter the world of 3D printing.

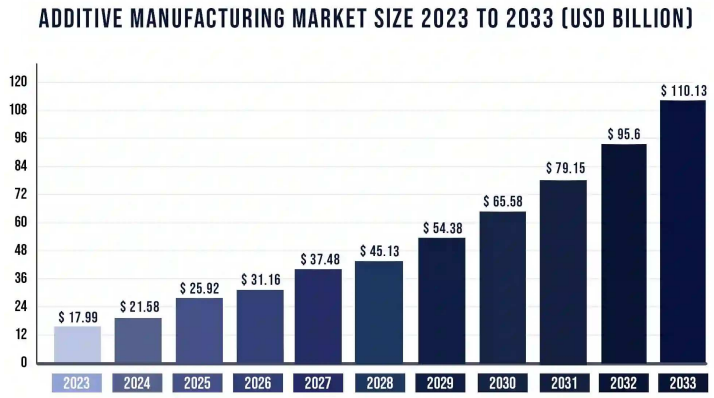

Figure 2.1: Prediction of Additive Manufacturing market. Source: *https://www.precedenceresearch.com/additive-manufacturing-market*

The global additive manufacturing market revenue was valued at USD 17.99 billion in 2023 and is poised to grow from USD 21.58 billion in 2024 to USD 110.13 billion by 2033, as shown in Figure 2.1. This extremely positive

predictions are a direct consequence of the deep interest from many different markets: the vast majority of engineering disciplines is now exploiting the benefits of 3D-printing. Structural, aerospace, automotive, biomedical, electronic, and energy storage, are only some of the sectors where additively manufactured components already embrace a primary role. Even in the medical world, bio-printing is responsible of huge developments, especially regarding the fabrication of tissues and organs. But again, it is not limited to this: let's cite for example the food industry, the design and fashion market, etc. The vision of 3D-printing embraces a new wider design freedom, thanks to the AM capability to produce complex geometries, otherwise impossible to obtain with traditional manufacturing technologies, which lead to custom enhanced properties optimized for the specific application requirements. From a broader perspective, AM leads the game in the fields where the main focus is set on the component performance and, strictly related with this, its customization. Moreover, 3D-printing is characterized by a smaller carbon footprint consequent to the reduction in material waste. A brief overview of the available AM technologies is resumed in Figure 2.2. Among these, the most commonly employed are shortly described.

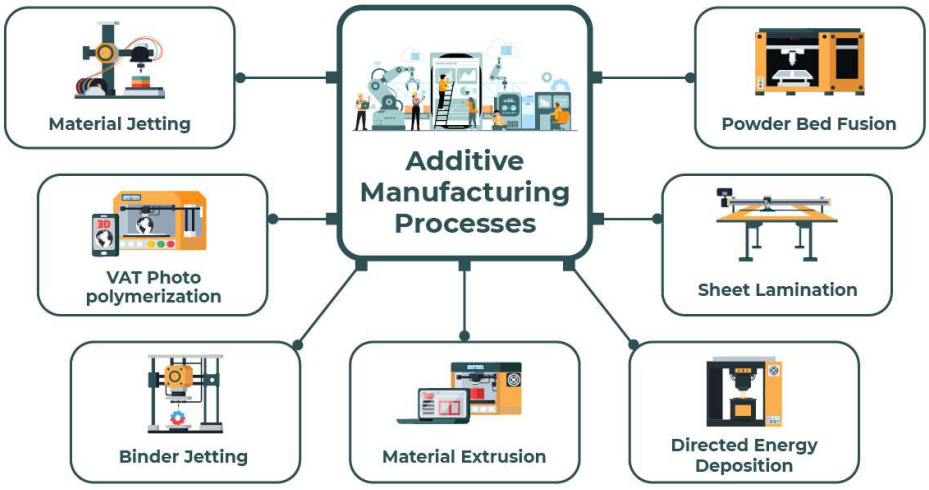

Figure 2.2: Schematics of the main Additive Manufacturing processes. Source: *https://manufacturing.report/articles/which-additive-manufacturing-process-is-right-for-you*

- **VAT Photo-polymerization (SLA)**: utilizes a UV laser to cure liquid photo-polymer resin into solid objects layer by layer. Known for producing parts with high accuracy and smooth surface finishes.

- **Binder Jetting**: involves depositing a liquid binding agent onto a powder bed to form solid parts. It is commonly used for producing metal, sand, and ceramic components.

- **Powder Bed Fusion (LPBF)**: this family includes Selective Laser Sintering (SLS) and Selective Laser Melting (SLM) technologies. A high-power laser is used to fuse powdered material, typically polymers (SLS) or metals (SLM), into solid objects. This method is known for its ability to create complex and durable parts with high precision.

- **Material Extrusion (MEX)**: the material, usually in form of filament or pellets, is heated up to a semi-melted state and extruded through a nozzle that moves following the deposition trajectory.

The MEX family includes also the Fused Deposition Modeling (FDM) technology, also known as Fused Filament Fabrication (FFF), developed by Stratasys in 1988. This technology is definitely the most cost-effective, as FDM printers and filaments are relatively inexpensive and easy to use, as a considerable amount of pre-configured settings for simple operations are available. Advantages in adopting FDM include also the material variety, as the wide range of filaments allows for versatile applications, from commercially available rigid or flexible plastics to fiber-reinforced materials and bio-polymers. As a direct consequence, FDM has become the most popular and accessible 3D-printing process to date. The most popular materials for thermoplastic filaments are worth being summarized:

- **PLA** *(PolyLactic Acid)*: PLA is relatively stiff and strong compared to other FDM materials, although it can be brittle. Hence, it is suitable for parts that need rigidity but are not subjected to high impact or bending, being prone to cracking. Also, PLA is derived from renewable resources, making it biodegradable and more environmentally friendly compared to petroleum-based plastics.

- **ABS** *(Acrylonitrile Butadiene Styrene)*: ABS is known for its toughness and impact resistance, making it suitable for functional parts that may undergo stress or handling. It is moderately more flexible than PLA, so it can withstand higher mechanical stress before breaking. Its properties make ABS a very good candidate for structural applications and functional prototypes. ABS performs best when 3D-printed in a controlled environment due to its tendency to warp and shrink.

- **PETG** *(PolyEthylene Terephtalate Glycol)*: PETG is known for combining the advantages of both PLA and ABS: PLA's ease of printing and low warping tendency come together with ABS's strength, durability, and flexibility. PETG is available in transparent or translucent varieties, which can be used to create parts with a glass-like appearance.

- **TPU** *(Thermoplastic PolyUrethane)*: Known for its elasticity and resilience, TPU offers a unique set of characteristics that make it suitable for applications that require flexibility, impact resistance, and wear resistance. It can bend, stretch, and compress without breaking, making it ideal when soft or flexible components are required, such as in gaskets, seals, and protective cases.

- **PC** *(PolyCarbonate)* and **PEEK** *(PolyEther Ether Ketone)*: PC and PEEK are high-performance thermoplastics, which offer superior mechanical and thermal properties compared to standard filaments. PC is a strong and tough material known for its excellent impact resistance and heat tolerance; PEEK has one of the highest tensile strengths of all 3D printing materials, combined with excellent fatigue resistance, making them ideal for critical applications in industries like aerospace, automotive, and healthcare, where extreme conditions demand superior material performance.

In recent years, the amount of new materials with advanced properties introduced in the 3D-printing filaments world, combined with the remarkable developments in the Design for Additive Manufacturing (DfAM) discipline,

paved the way to a transition in the FDM technology application fields. FDM was, indeed, mainly confined to rapid prototyping and usages where no load-bearing capability was involved. On the other hand, the appearance of FDM components in novel advanced and functional applications means the parts must address more demanding requirements. Following this, an extensive analysis of the mechanical response of FDM-printed components must be available as a reference for engineers and designers. The more advanced the application, i.e. the more critical the requirements, the more reliable must the part be. This prompts to approach from a mechanical perspective the behavior of FDM-ed components both in safe and damage regimes, to exploit the best performance out of them in circumstances where failure is not an option. In order to define a framework for the mechanics of parts 3D-printed via FDM technology, focus must lay on the additive process itself, schematized in Figure 2.3.

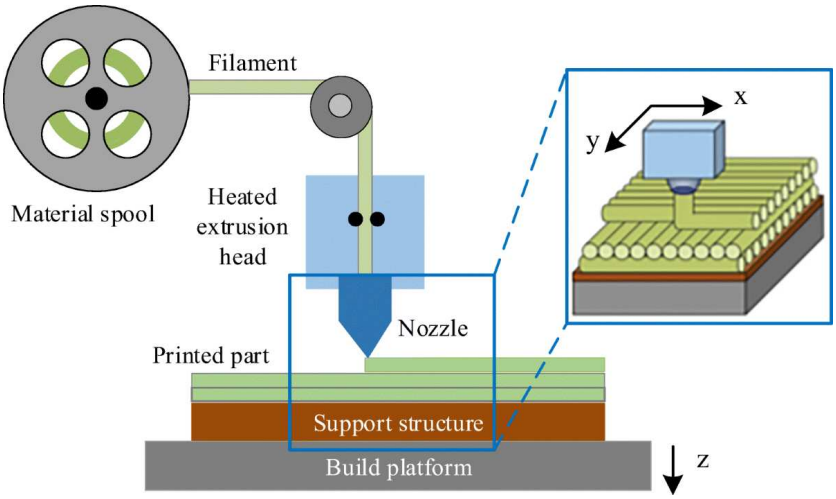

Figure 2.3: Schematics of the FDM process, from [28]

The filament is pulled from the material spool to the heated extrusion head, where it reaches a semi-melted state, and then extruded through the nozzle, which moves in a predetermined trajectory in x-y plane, to deposit the material onto the build platform. As each layer cools and solidifies, the build platform moves in z-direction and the process repeats layer-by-layer, gradually building the object from the bottom up. Starting from the 3D CAD

file of the part, a slicer software slices the model into thin horizontal layers, generates the G-Code file for the print which defines the tool-path for the nozzle to follow. Support structures may be added to help with overhanging parts or complex geometries, which can be removed post-printing.

Consequently to the inherent nature of the process, it is evident that process parameters play a primary role to influence the resulting mechanical performance of the FDM-printed component. Among these, the most important are: *i*) the **layer thickness**, ruling the part dimensional accuracy and surface finishing; *ii*) the **extrusion temperature**, playing on the filament viscosity while being extruded and the bonding between adjacent filaments; *iii*) the **deposition strategy**. The filament orientation when deposited strongly influences the properties of the final part. In particular, the key aspect is the relative orientation between filament and load directions, as the mechanical performance in terms of load-bearing mechanism widely differs between the deposition direction and the others directions: directional properties explain the significant anisotropy of parts fabricated via FDM technology; *iv*) the **filling density and strategy**. This advantages of additive manufacturing technology allows to save material where not strictly needed, leading to lightweight components with the same (or even better) performance as if filled of bulk material inside: various filling architectures are available, each leading to a different mechanical behavior of the whole part.

Many studies in the technical literature focus on the influence of printing parameters on the mechanical response of FDM-printed parts [29]. Indeed, through a proper understanding of it, the resulting properties of the component can be predicted at the design stage. The anisotropy due to the deposition process has been studied in [30, 31, 32, 33, 34], mainly regarding tensile or compressive loads on standard specimens. Some works have also looked for the optimal combination of parameters considering the mutual interactions between factors [35, 36, 37, 38], embracing Design-of-Experiments (DoE) approaches with statistical or machine-learning-based tools.

It has also been found that the temperature and heat transfer conditions have strong repercussions on the bond quality between filaments and

therefore the mechanical properties of the final part [39]. All these works highlight that FDM-printed parts present non-homogeneous mechanical resistance: the bond formation process between deposited filaments is the key phenomenon to understand. In this framework, thermal-structural Finite-Element models are available to simulate the deposition process by a special tool based on sequential element activation, analyzing how printing conditions affect the degree of bonding between adjacent filaments and confirming that interfaces between filaments are the weakest regions [40, 41, 42]. Basis of these works are found in the notorious work by Brenken [40]: the temperature field and the degree of crystallinity during the fabrication of an air inlet are shown in Figure 2.4(b). Analytical approaches can be also found, for example the two-stage thermal and sintering methodology proposed by Garzon-Hernandez [43] to predict the bond formation process between filaments, allowing to design components with custom properties starting from a comprehensive understanding of the effect of manufacturing settings on the sintering process ruling the bonding at the interface, see Figure 2.4(a).

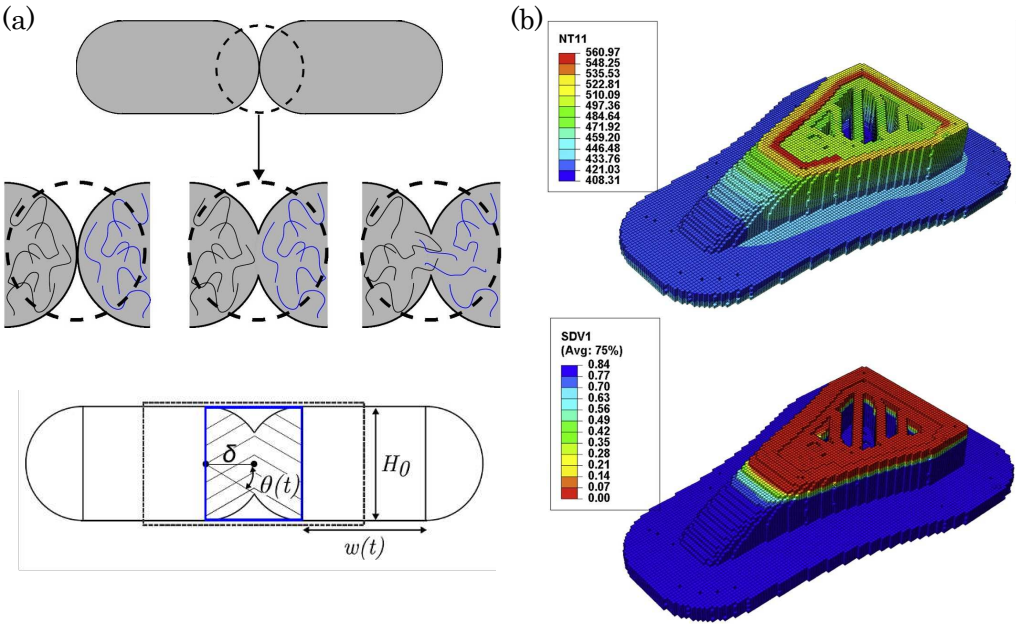

Figure 2.4: Most representative reference works for the mechanics of bonding between filaments in FDM: a)Analytical approach by [43]; b)Numerical simulation by [40].

Also, a heat transfer-based polymer inter-molecular diffusion theory, developed by Yin [44] is found to be effective in modeling the interfacial bonding mechanism, providing accurate predictions that can help improving the mechanical properties and function of FDM-printed products.

Together with the use of FDM process for engineering components, it becomes necessary to investigate the behavior of these parts both in safe and damage regimes. Some studies are available on the understanding of the failure of printed specimens by observing the fracture surface [45] and on the investigation of the damage evolution of printed PLA from the loss of performance under cyclic loading [46]. Material properties correlated with the fracture mechanics have also been related with the set of parameters employed for the filament deposition process. In [47] the apparent fracture resistance of double-cantilever-beams is experimentally correlated with layer thickness and nozzle temperature. Factors influencing the interface bonding between adjacent filaments are identified in [48]: this aspect is again proved to be directly connected with the fracture toughness behavior under various fracture modes, predominantly controlling the structural integrity of the component.

Looking at the main reference works in this field, a comprehensive approach able to consider both the material properties in safe and damage regimes up to failure and the effect of manufacturing parameters on the mechanical response of the component is missing. All the available works focus on one specific aspect, which is investigated in detail; on the other hand, all these approaches are either developed analytically or computationally too expensive to be extensively used to model FDM-printed engineering components inside simulations.

This chapter aims at providing a fast way to model 3D-printed parts in Finite-Element environment, considering the additive manufacturing fabrication process i.e. all the characteristics and properties that make their mechanical response different from the same geometry obtained through traditional subtractive or formative manufacturing methods.

Having more reliable and precise and easy-to-use numerical models for additively manufactured components is one of the main challenges nowadays.

To this end, a multi-scale approach will be introduced in the next section (Section 2.2), while Section 2.3 will focus on the damage mechanism of FDM-printed parts with more complex geometries, such as cellular structures.

2.2 Multi-Scale Modeling

This section presents a novel approach for the multi-scale modeling of FDM-printed components. The underlying motivation is to provide a fast and quite straight-forward methodology to take into account the peculiarities of the additive manufacturing fabrication process when modeling a part inside numerical environment.

In this framework, utilizing a Reference Volume Element (RVE) appears to be a reliable alternative, as it limits the analysis to a single unit cell. This is particularly useful for repetitive structures and when employing numerical methods, as it effectively represents the overall material behavior at the mesoscale. Given the unique symmetry and consistent porosity between neighboring filaments, this method has already provided accurate results in determining the elastic constants of FDM-printed components, e.g. in [49, 50].

Considering the above, this study explores the impact of key controllable process parameters on the mechanical behavior of a broad range of tensile specimens fabricated using FDM technology. Microscope observations serve as the initial step in understanding how the morphology of various specimens is influenced by the parameters selected during the printing process.

In this study, 35 tensile specimens with 1BA geometry, as per the EN ISO 527-2 standard (5x2 mm cross-section), were 3D printed using a Raise3D Pro-2 printer and ABS filament from FormFutura. The filament was initially subjected to mechanical testing to precisely determine its elastic modulus and failure strain. The various combinations of printing parameters investigated are summarized in Table 2.1, while a qualitative illustration of the resulting layered structures is provided in Figure 2.5.

The key parameters studied include layer height and raster orientation angle, along with three extrusion temperatures. Each parameter is evaluated at both the average and extreme values of its range. For each scenario, N specimens are produced and tested, enabling a statistical analysis of the variation in responses within each group. To ensure that the influence of

Table 2.1: Sets of process parameters for each considered Scenario

Scenario	N	Layer height [mm]	Printing temperature [°C]	Raster orientation
1	5	0.4	250	0°
2	5	0.4	250	-45°/+45°
3	5	0.2	250	0°
4	5	0.4	230	0°
5	5	0.4	270	0°
6	5	0.4	230	-45°/+45°
7	5	0.4	270	-45°/+45°

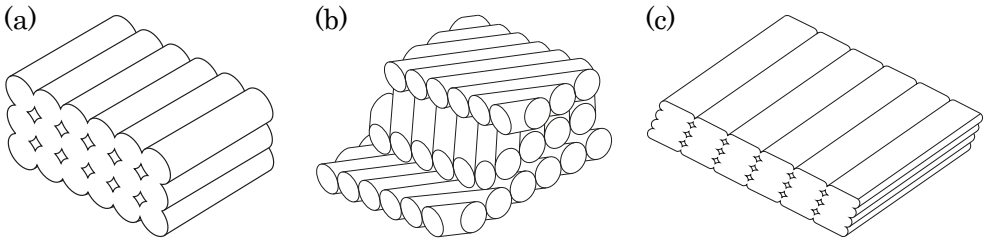

Figure 2.5: Cross-section geometry depending on process parameters: a)1st scenario; b)2nd scenario; c)3rd scenario.

the raster angle on tensile performance is not impacted, the specimens are printed without circumferential layers (walls).

Specimens are sliced using a razor blade mounted on a rigid support, and their cross-sections are observed under a microscope to capture the morphology of the layered structure. This information is used to create a set of 3D CAD models. Since the microstructure is largely uniform across the observation area, the entire part can be viewed as a periodic face-to-face tessellation of a unit cell in 3D space, making it feasible to apply the RVE approach to represent the material system as a whole.

In parallel, a finite-element model series is developed adopting the RVE approach. A unit cell is identified from microscope images as the smallest repeatable entity: Figure 2.6 shows the RVE definition based on the superposition of a sample cell to a micrograph of the cross-sectional morphology.

The layer height is the parameter that most significantly influences the RVE geometry. Two values are considered here: 0.4 mm and 0.2 mm, while the deposition width remains constant at 0.4 mm. For the $-45/+45°$ raster angle condition, the repeating unit observed in the cross-section is twice the

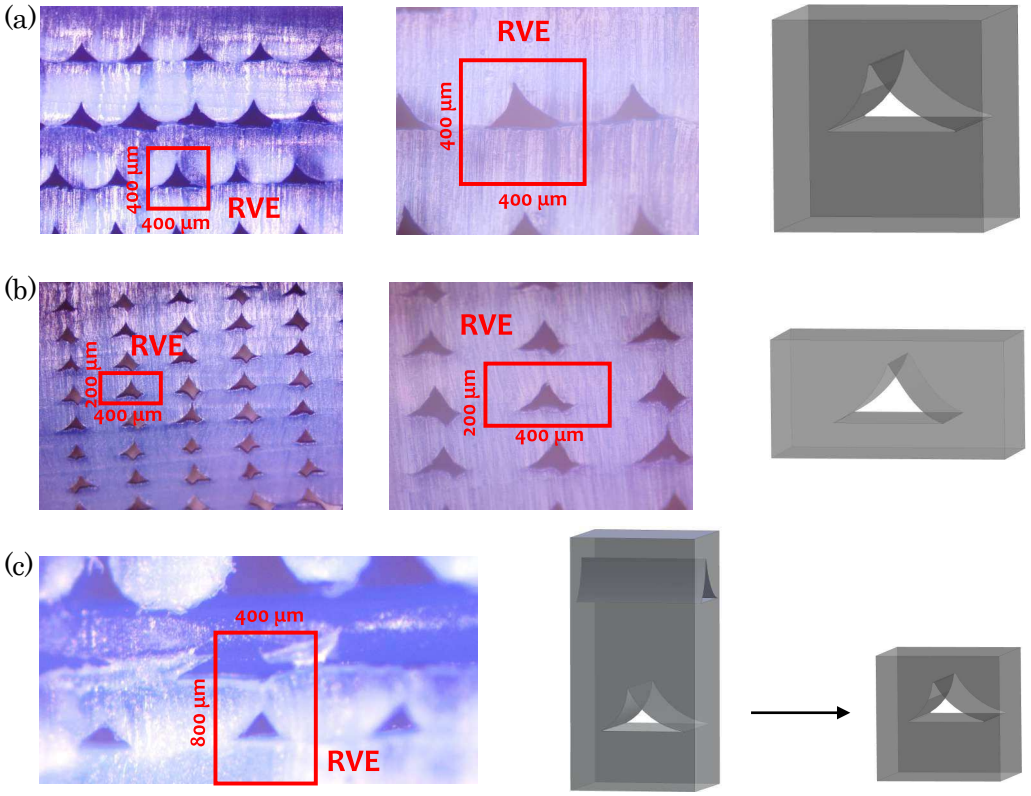

Figure 2.6: RVE definition from cross-sectional morphology: a-b)Layer height of 0.4 and 0.2 mm, respectively; c)-45/+45° raster angle morphology.

size of the unit found for the 0° raster angle condition. This is because the porosities between adjacent filaments align with the raster directions, meaning the porosities of consecutive layers are oriented perpendicular to one another (see Figure 2.6(c)). However, since the loading direction is at a 45° angle relative to the unit cell faces, only half of the unit cell needs to be modeled, as the mechanical behavior is symmetrical between the top and bottom parts. More specifically, the RVE geometry is a cube with 0.4 mm edges, except in scenario 2, where the width and height are reduced to 0.2 mm. The porosity accounts for approximately 7% of the volume, with its height being about half its length, and the length constituting around 65% of the RVE's total length.

Microscope observations of scenarios with varying extrusion temperatures once again reveal that this parameter significantly influences the bonding

quality between adjacent filaments. As shown in Figure 2.7, higher extrusion temperatures improve filament bonding due to reduced material viscosity during deposition. Conversely, lower temperatures result in weaker bonding, as previously noted in [51].

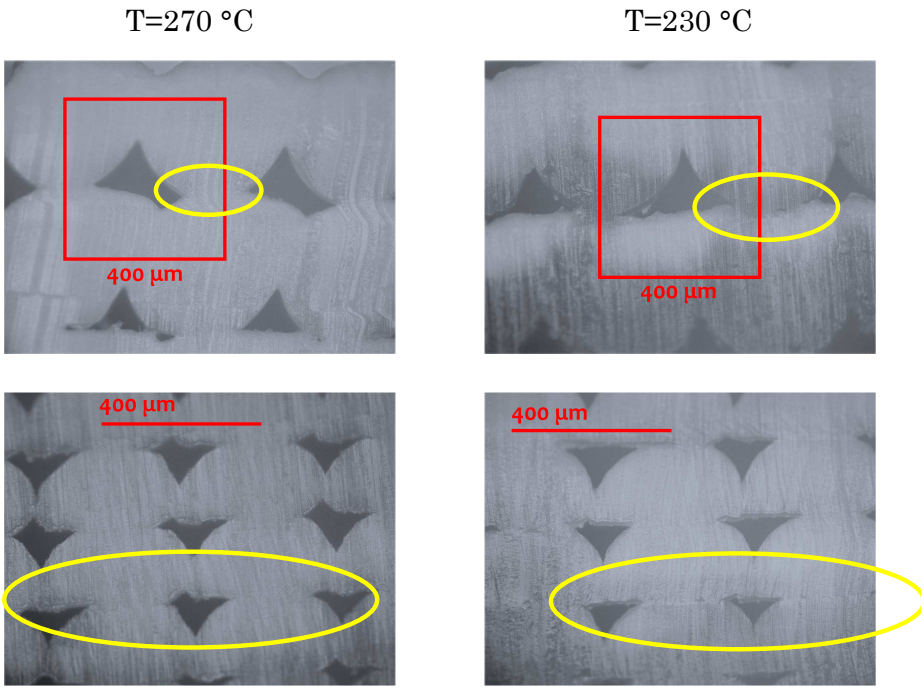

Figure 2.7: Microscope observations of temperature influencing the bonding between filaments

Starting from this observation, the Cohesive Zone Model (CZM) is combined with the previously introduced RVE approach. Interface regions are, indeed, modeled with a layer of cohesive elements, allowing to define these regions differently from the rest of the model, according to experimental observations which find these interfaces to be usually weaker than the bulk material. In this way, it is possible to consider the typically noticed phenomenon at the mesoscale which is responsible for the separation (debonding) of adjacent filaments. In Figure 2.8(a) interface zones, that are 4 in number for each RVE, are highlighted.

Debonding and separating properties are modeled by cohesive sections.

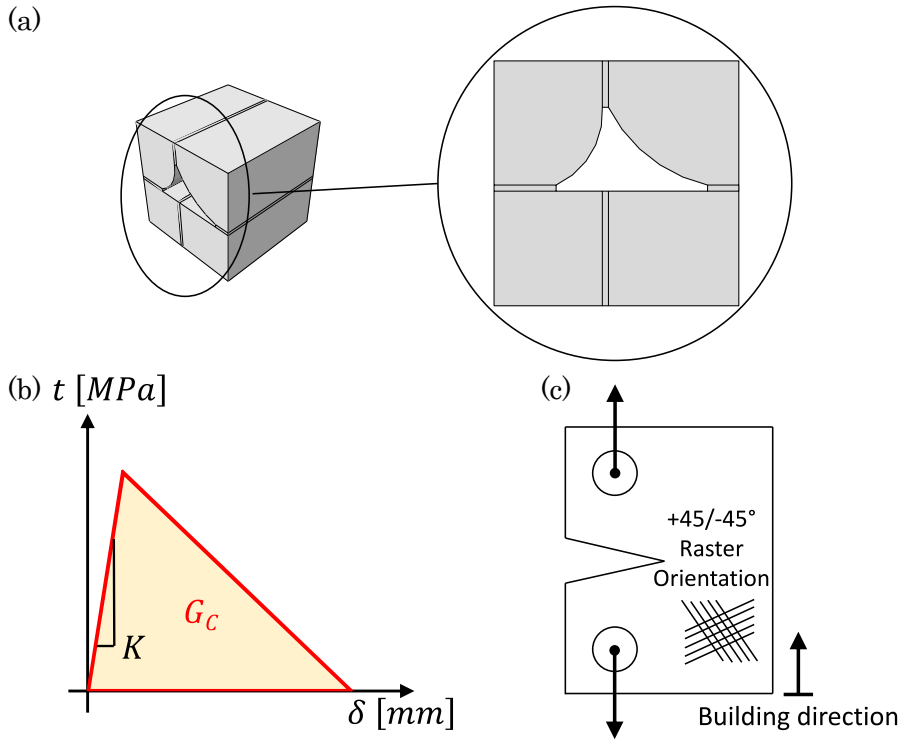

Figure 2.8: Definition of CZM elements properties: a)Cohesive regions in RVE; b)Load-displacement response of cohesive elements; c)CT specimen for fracture toughness test.

The elastic behavior of the cohesive zone is expressed by Equation 2.1, [52]:

$$\begin{bmatrix} t_N \\ t_S \\ t_T \end{bmatrix} = \begin{bmatrix} K_{NN} & 0 & 0 \\ 0 & K_{SS} & 0 \\ 0 & 0 & K_{TT} \end{bmatrix} \begin{bmatrix} \delta_N \\ \delta_S \\ \delta_T \end{bmatrix} \tag{2.1}$$

with t_N, t_S, t_T being respectively the normal stress, shear stress and tear stress, and δ_N, δ_S, δ_T the separation, shear, and tear displacement. Here, K represents the initial stiffness of the interface, schematized in Figure 2.8(b): as in traditional modeling of adhesive joints, the value of stiffness is significantly high as it is defined as the ratio of the elastic modulus over the adhesive thickness, that is nearly zero in this case; a value of 10^6 MPa is frequently employed when modeling composites [52], and the same holds for this work. The fracture toughness G_C is determined from CT specimens

with the same building direction and raster orientation as the samples to be characterized, see Figure 2.8(c).

Meanwhile, the bulk ABS material, corresponding to the RVE regions occupied by the deposited strands far from the bonding interfaces, is numerically modeled through the Ramberg-Osgood constitutive law in the form of Equation 2.2, to appreciate the gradual transition between the elastic and the plastic behavior noticed from experimental tests:

$$E\varepsilon = \sigma \left[1 + \alpha \left(\frac{\sigma}{\sigma_0} \right)^{n-1} \right] \tag{2.2}$$

Parameters E, α, σ_0 and n are determined fitting at best the tensile curve of ABS filament. More in details, a tensile test is performed on a single filament with nominal diameter of 1.75 mm and strain rate of $1.66e^{-3}$ s^{-1}, see Figure 2.9. Although the heat during the extrusion may change the crystallinity of the polymer, this test aims at the definition of the properties of the "bulk" filament, as the printing parameters are already considered in the development of the numerical model.

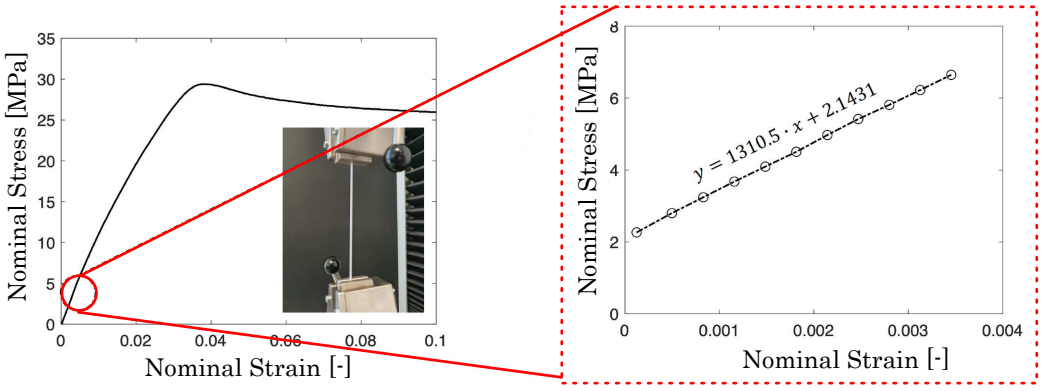

Figure 2.9: Tensile test on a single ABS filament

At this point, the modeling of the material behavior in damage regime must be taken into account. Two damage variables are defined: d for the bulk ABS material and D_C for the cohesive region at the interfaces. In other words, these two damage variables are representative of the possible

damaging mechanism of the component at different length scales: d is defined at the micro-scale, being an inherent property of the material, while D_C plays at the meso-scale being related with the debonding phenomenon between adjacent filaments.

The micro-scale damage is modeled via the ABAQUS isotropic *Ductile Damage Model*, setting a damage strain value that could fit the experimental tests. A damage evolution law is also determined to describe the evolutive part, choosing a quadratic form in accordance with the behavior experimentally noticed. The computed damage variable d affects the elastic modulus E_d as stated in the continuum damage mechanics theory framework, where E is the elastic modulus of the undamaged material:

$$E_d = E(1 - d) \tag{2.3}$$

In order to define the damage behavior of the cohesive zone, it is necessary to introduce the damage initiation displacement δ_0 and the final separation displacement δ_F, with the latter corresponding to the complete debonding. These quantities are defined as follows:

$$\delta_N^0 = \frac{t_N^0}{K_{NN}} \qquad \delta_S^0 = \frac{t_S^0}{K_{SS}} \qquad \delta_T^0 = \frac{t_T^0}{K_{TT}} \tag{2.4}$$

$$\delta_N^F = \frac{2G_{IC}}{t_N^0} \qquad \delta_S^F = \frac{2G_{IIC}}{t_S^0} \qquad \delta_T^F = \frac{2G_{IIIC}}{t_T^0} \tag{2.5}$$

where G_{IC}, G_{IIC}, G_{IIIC} are the critical fracture energies for Mode I, Mode II and Mode III, respectively, and they are responsible of the slope of the softening region in Figure 2.8(b).

Damage initiation threshold is defined via the maximum nominal stress criterion:

$$max \left\{ \frac{\langle t_N \rangle}{t_N^0}; \quad \frac{t_S}{t_S^0}; \quad \frac{t_T}{t_T^0} \right\} = 1 \tag{2.6}$$

Once the condition for damage initiation is reached, the cohesive damage variable D_C is computed according to Equation 2.7, where the effective relative displacement in case of mixed-mode scenarios is $\delta_m = \sqrt{\delta_N^2 + \delta_S^2 + \delta_T^2}$.

$$D_c = \frac{\delta_m^F(\delta_m - \delta_m^0)}{\delta_m(\delta_m^F - \delta_m^0)} \tag{2.7}$$

The damage variable D_C affects the properties of the cohesive region, operating on $\bar{t}$ which represents the stress components predicted by the elastic traction-separation behavior for the current strains without damage. Indeed:

$$\begin{aligned} t_N &= \begin{cases} (1 - D_C)\bar{t}_N & \bar{t}_N \geq 0 \\ \bar{t}_N & \bar{t}_N < 0 \end{cases} \\ t_S &= (1 - D_C)\bar{t}_S \\ t_T &= (1 - D_C)\bar{t}_T \end{aligned} \tag{2.8}$$

In this way, the RVE damage is due to two contributions: the isotropic damage of filaments, and the interface decohesion between filaments; these mechanisms are acting at the micro-scale, and as in typical unit cell approaches, the response is evaluated at the meso-scale. Table 2.2 summarizes the set of parameters adopted for the development of the numerical model.

Some remarks are necessary to properly understand and discuss the values found in the table. The ductile damage model parameters are chosen from the previously reported filament test, while the fracture energy G_C found in [34] for CT specimens, see Figure 2.8(c), is adopted as reference value since material, deposition path, and filament diameter are the same of the present investigation; only, to cover the full nozzle temperature range here considered, i.e. 230–270 °C, a variation of ± 10 % of G_C every ± 20 °C is set in accordance to what found in [47]. The fracture properties of the structure are defined equal to those of the cohesive elements adopting the "weakest-link approach", according to [34] where the direction of crack propagation is evidenced being along the interface between filaments. Finally, the damage initiation stresses for Mode I condition are determined from the tensile curves at raster angle ± 45°, considering the influence of temperature. Values for Mode II/III conditions are calibrated from Mode I values according to [53, 54], assuming the damage initiation stress to be proportional to the fracture load.

After the detailed modeling process for the RVE, a proper setting of Periodic Boundary Conditions (PBCs), representative of the spatial tessellation

Table 2.2: Material parameters in the numerical model

ABS filament				
Elastic modulus E [MPa]	1310			
Poisson coefficient ν [-]	0.3			
Plastic offset α [-]	0.007			
Yield stress σ_0 [MPa]	22			
Strain-hardening exponent n [-]	13			
Material ductile damage model				
Fracture strain [%]	0.6			
Displacement at failure [mm]	0.0002			
Exponential law parameter [-]	2			
Cohesive section				
Elastic stiffness [MPa/mm]	10^6			
Fracture energy G_C [kJ/m^2]	Temp [°C]			
$[G_C = K_{IC}^2\ (1-\nu^2)E^{-1}]$	230	1.65		
	250	1.82		
	270	2.00		
Damage initiation stress [MPa]	Temp [°C]	Mode I	Mode II	Mode III
	230	14	32	32
	250	20	40	40
	270	27	56	56

of the unit cell, is required by this approach. PBCs stipulate that opposite pairs of surfaces on the boundary of the RVE must deform identically under a given loading history, as expressed in Equation 2.9:

$$\zeta_{(x,y)}^{N_a} = \zeta_{(x,y)}^{N_b} \quad \text{on boundary} \quad \Omega_k \tag{2.9}$$

being ζ the considered model parameter (displacement in this work), N_a and N_b the sets of nodes kinematically linked on opposite edges of the RVE, and k the top/bottom/left/right boundary of the unit cell. In the Finite-Element code, this constraint is expressed through a set of canonical equations linking together all the degrees of freedom of nodes belonging to the boundary edge or surface:

$$A_1 U_1^P + A_2 U_2^Q + ... + A_N U_K^R = 0 \tag{2.10}$$

with 1, ..., N scalar coefficients and 1, ..., k the DOFs of P, ..., R nodes. Master nodes are defined, where loads are applied, in traction or shear.

As for the meshing strategy, 8-node linear brick elements (C3D8) are chosen for the ABS material, justified by the unit-cell cubic geometry and by the lack of significant flexural fields, and 8-node three-dimensional cohesive elements (COH3D8) are adopted to mesh interface regions. The thickness of the cohesive zone is 10 μm and it is meshed with sweep technique and direction normal to the interface surface. The choice of not opting for a zero-thickness cohesive layer, very often used for this kind of fracture simulations, is simply due to the need of having non-coincident nodes when applying PBCs.

The last remark regards the load application to the RVEs. While the application of a traction is straightforward when filaments and loading direction are parallel, in the 45° configuration the load is applied considering an equivalent stress state: in detail, considering an infinitesimal element Φ, when the raster angle is zero the uniaxial load acts along the X-direction, situation 1 in the scheme of Figure 2.10. On the contrary, for raster angles different than zero, as the RVE is defined with 90° faces, it must be rotated by the same angle. Thus, in accordance with a Mohr's circle, a biaxial stress state along X and Y axes should be defined as producing the equivalent uniaxial tension along X. The equivalence is obtained by applying both normal and shear stress, as Figure 2.10 graphically explains.

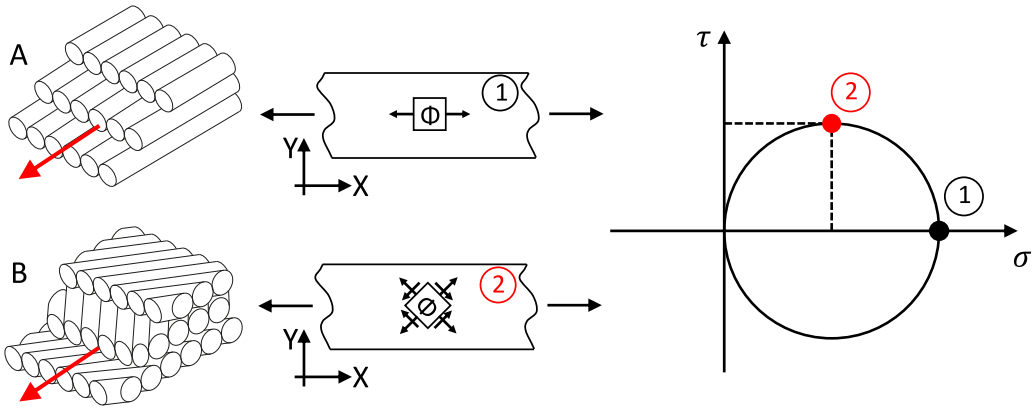

Figure 2.10: Stress fields in Scenarios 1 and 2

Outputs from numerical simulations are compared and validated against experimental tests. All the samples are mechanically tested in displacement control at constant rate of 3 mm/min on the uniaxial tensile Test® GMBH Universal Testing Machine (Model 112) equipped with a 2kN cell load, and data are elaborated in terms of nominal stress–strain curves, not showing the specimens any significant necking during the traction.

As expected from previous considerations, the raster angle is the design parameter that influences the mechanical properties the most. In Figures 2.11(a) and 2.12(a) the averaged response with the standard deviation (STD) band for the 5 samples belonging to "Scenario 1 – raster angle 0°" and "Scenario 2 – raster angle ± 45°" is plotted. Engineering nominal quantities are considered. As for the bulk ABS, the response is linear elastic for most of the strain range, slightly deflects for a relatively short plastic regime, and abruptly falls when damage starts to occur till the rupture strain that is about 3.5 % and 2 % for the two sets, respectively. For comparison, the plots include the simulated curve by the RVE models, which shows the contours of stress (Figure 2.11(b) and Figure 2.12(b)) and of the damage variables. As said, the raster angle affects the damage mechanism that leads to failure. When the raster angle is 0°, i.e. all the filaments are oriented in the same direction of the load, the load-bearing capacity is relatively good, with an ultimate stress of about 28 MPa. Accordingly, Figure 2.11(c) shows how the damage d initiates and evolves in correspondence of increasing levels of strain following the intrinsic micro-scale ductile damage imposed for the ABS polymer described by Equation 2.3. For such a simple load, no interaction effects between filaments are evidenced by the FE model; in other words, the cohesive elements do not work as they are not subjected neither to traction-separation neither to shear loads. This means that the average value of 3.5 % for failure strain reflects the constitutive law of the filament material itself, whereas the porosity affects the elastic properties only.

An alternative interpretation can be applied to the behavior in scenario 2, where the raster angle is ±45° relative to the loading direction. In comparison to the zero-degree angle, the specimens experience failure at around 50% of the failure strain, as shown in Figure 2.12. For reference, the same

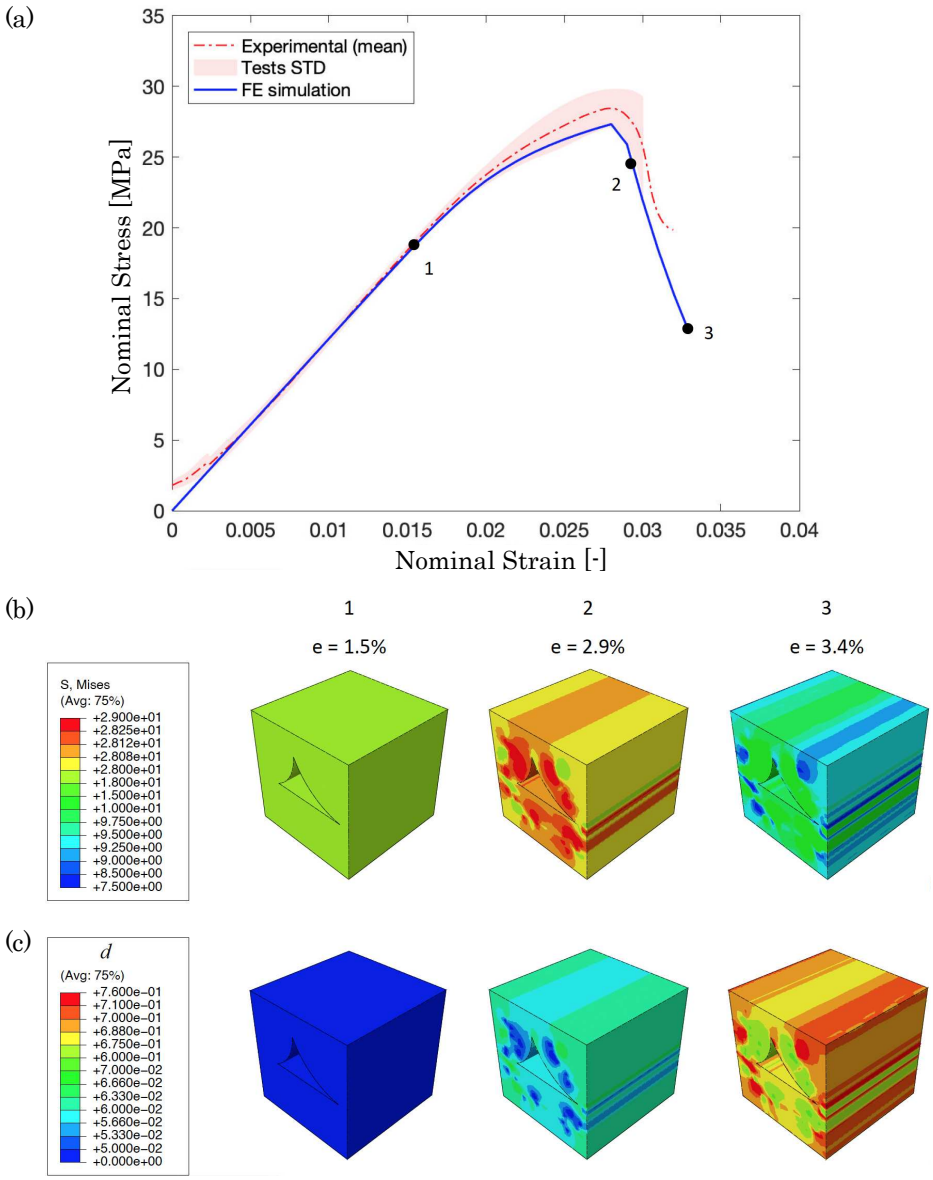

Figure 2.11: Experimental and simulation results on Scenario 1: a)Tensile response; b)RVE stress field at points 1, 2, 3; c)Damage evolution at the micro-scale.

figure 2.12(a) shows with a blue dotted line the response of the RVE without cohesive elements being modeled or activated. In this scenario, the damage mechanism no longer aligns with the experimental results, as the ten-

sile curve declines in subsequent steps at strains of approximately 1.2% and 3.2%, corresponding to the failure of individual layers, one by one. Specifically, intersections between adjacent filaments, which are continuous in this model, lead to local stress concentrations that accelerate stiffness degradation and cause unrealistic load redistribution. Returning to the cohesive elements RVE, debonding between adjacent filaments occurs near the end of the elastic phase, as indicated by point 3 in Figure 2.12(b-c). This debonding competes with the onset of the ABS plastic regime. As the RVE stress state becomes biaxial, as shown earlier in Figure 2.10, the cohesive layers are subjected to Mode I separation and Mode II shear, making them the "weakest link" to sustain damage and ultimately fail. Figure 2.12(d) depicts the evolution of cohesive damage, which leads to the progressive loss of load-bearing capacity in the RVE, highlighting the moments when cohesive elements begin to function and then completely fail.

In Figure 2.13, the experimental response of specimens printed with the parameters set of Scenario 3, i.e. layer height half of the previous value, is compared with the FE simulation output. The match is accurate, validating the numerical model as a reliable tool to understand the influence of this important parameter as well. Failure strain raises back to about 3%, in accordance with the response of Scenario 1, see previous Figure 2.11(a), because again the damage first occurs within the filaments, and not in the weakest sealing zones between filaments. Here the filaments work essentially under uniaxial tension that acts along the same direction of deposition. This allows to state that, as one might expect, the predominant damage mechanism, or the ductility of the structure, depends on the mutual direction between load and filament deposition, i.e. on the raster angle of filament layers.

After having evidenced the influence of the deposition strategy on the mechanical properties and failure of the FDM-printed part, another primarily important process parameter, which is the extrusion temperature, must be investigated at this point. As previously demonstrated, the temperature of the extruding nozzle plays a crucial role in determining the quality of bonding between adjacent filaments, which in turn affects the interfacial strength between them. Analyzing the tensile tests for scenarios 1–4-5 and 2–6-7 re-

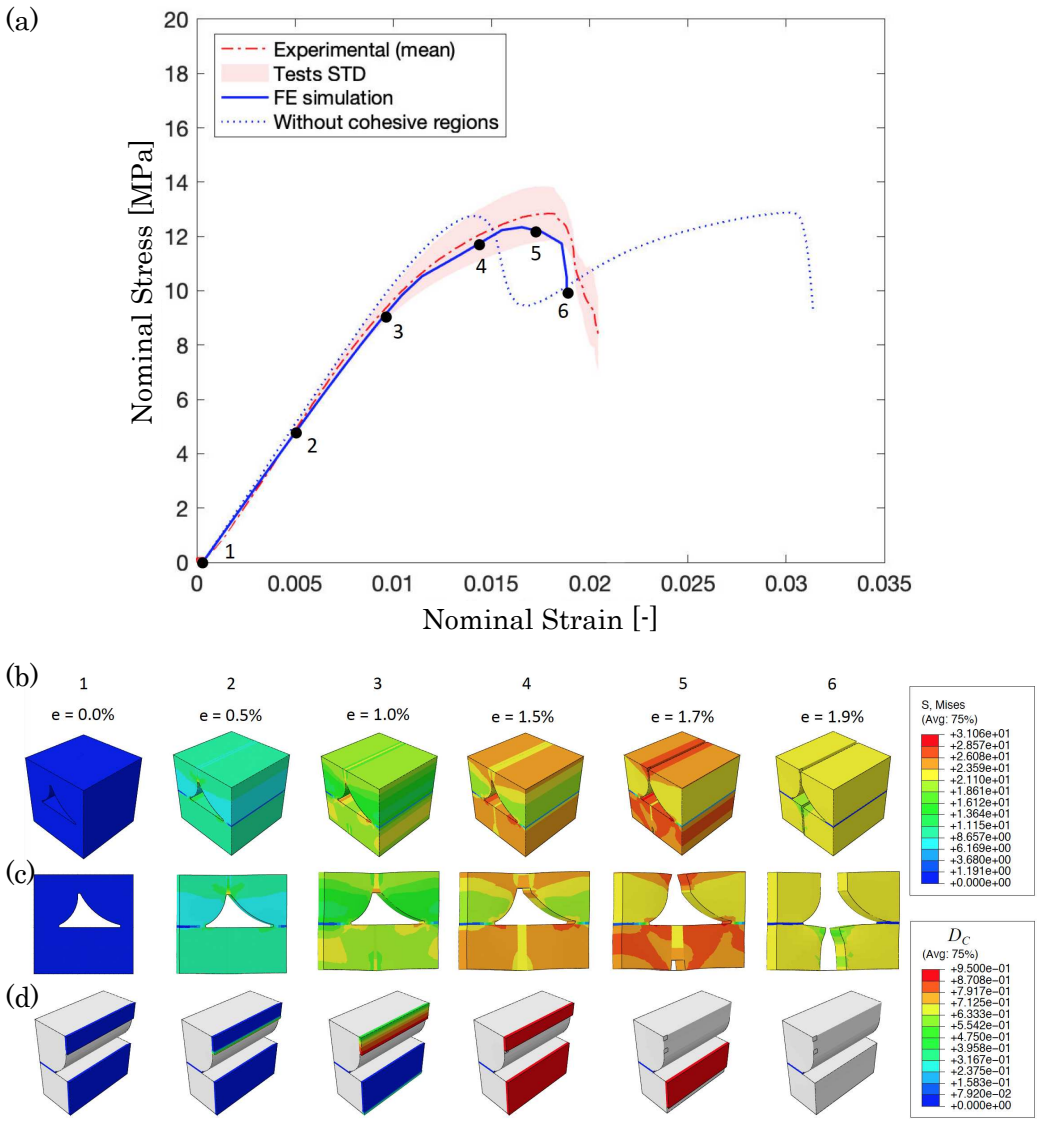

Figure 2.12: Experimental and simulation results on Scenario 2: a)Tensile response; b)RVE stress field at points 1, ..., 6; c)Detail of separation between adjacent filaments (magnitude 5x); d)Damage evolution of the inter-filaments melted interface.

veals that the first group, with a 0° raster angle, is not influenced by the temperature. In contrast, the response of the second group is highly sensitive to the printing temperature. This is illustrated in Figure 2.14(a), where the curves at different temperatures for the 0° raster angle overlap (shown

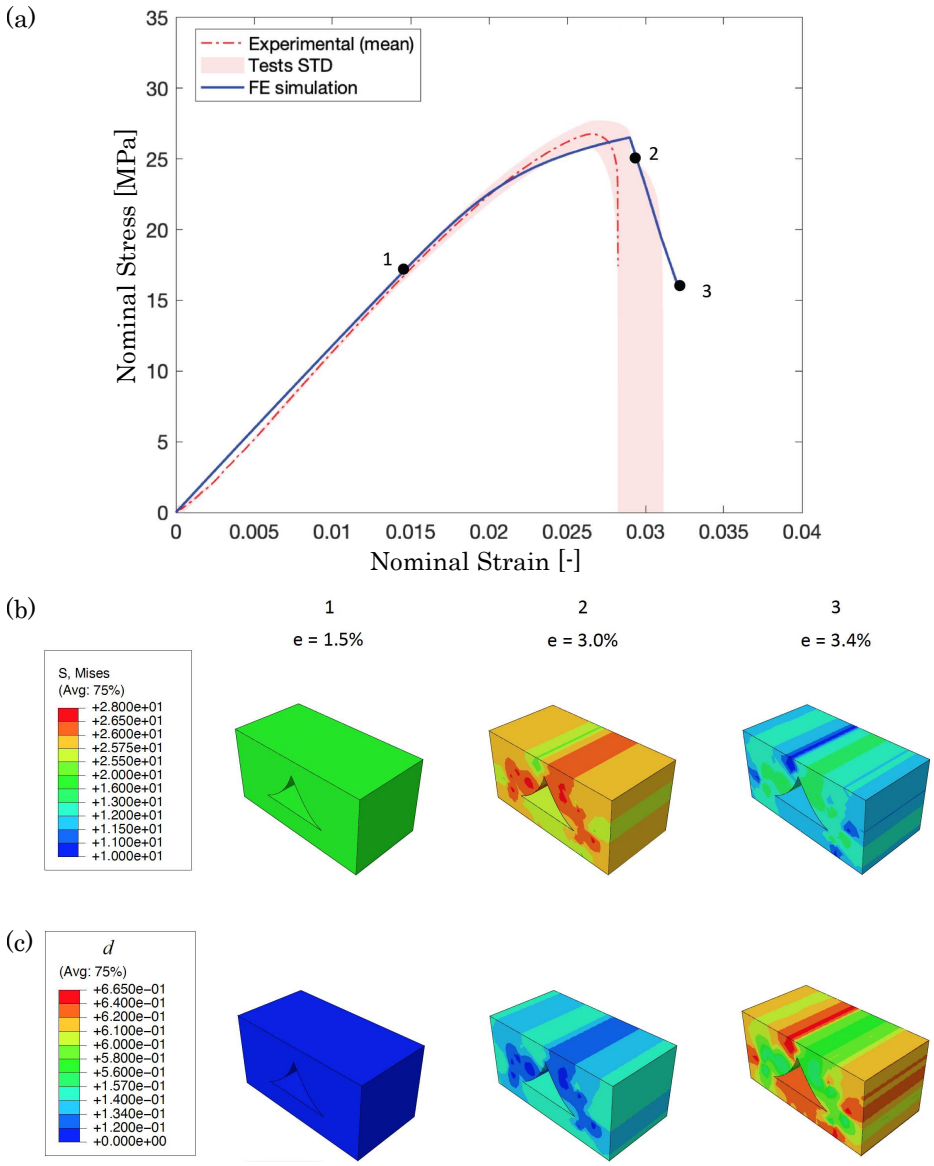

Figure 2.13: Experimental and simulation results on Scenario 3: a)Tensile response; b)RVE stress field at points 1, 2, 3; c)Damage evolution at the micro-scale.

in pink), while those at other angles are clearly distinguishable (shown in black). This observation is further clarified in Figure 2.14(b), which depicts the ultimate tensile strength (UTS) as a function of temperature for the two scenario groups. These findings support the hypothesis proposed in this

study: when there is a non-zero angle between the load and the deposited filament orientation, the specimen experiences a multi-axial internal stress state. As a result, the bonded interfaces between the filaments are subjected to separation forces, causing the filaments to detach and leading to the initiation of micro-cracks, which ultimately result in "premature" failure.

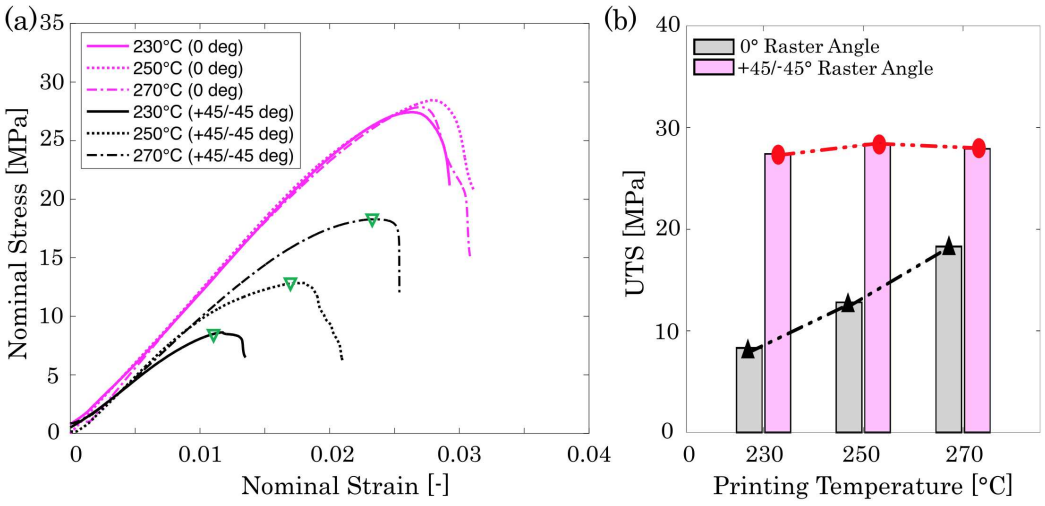

Figure 2.14: Extrusion temperature affecting the tensile response: a)Influence of raster angle; b)Bar plot for UTS.

Looking at the black curves in Figure 2.14(a), green markers are added in correspondence of the meso-scale damage initiation. From these points, a set of damage initiation thresholds t_N^0, t_S^0, t_T^0 are determined for the cohesive elements, expressed as function of temperature. Resulting data have been anticipated in Table 2.2. This results with good approximation a linear form of T:

$$\begin{aligned} t_N^0(T)[MPa] &= 0.325\ T[C] - 60.92 \qquad Mode\ I \\ t_{S,T}^0(T)[MPa] &= 0.350\ T[C] - 48.17 \qquad Mode\ II\ \ and\ \ III \end{aligned} \tag{2.11}$$

The agreement between simulations and experiments is now evident, confirming the model's accuracy in replicating the material behavior. Additionally, it establishes the model as a useful tool for predicting and optimizing the printing path when the principal stresses are known. This key outcome is il-

lustrated in Figure 2.15, where the RVE response is compared with variations in printing temperature using the previously determined parameters.

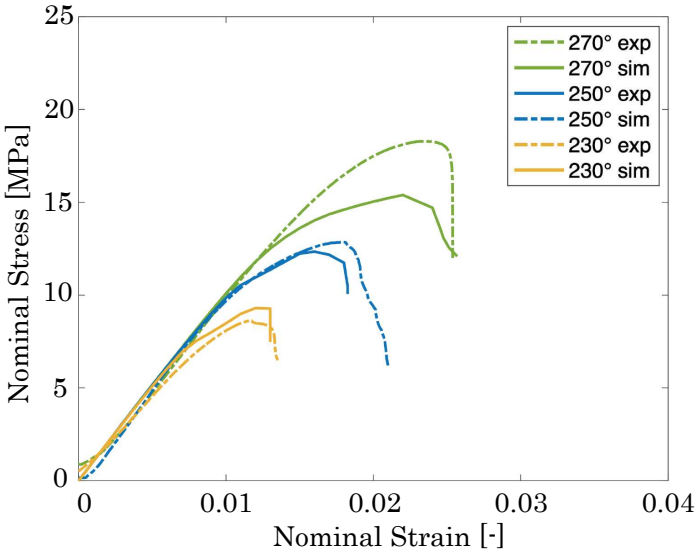

Figure 2.15: Simulation of the extrusion temperature effect on Scenarios 2 (blue lines), 6 (yellow lines), and 7 (green lines)

The numerical results for the green curves (270 °C) underestimate the maximum nominal stress observed during the tensile test, even though the elastic region is well captured. This discrepancy might be attributed to the very low viscosity of the extruded filament at such a high temperature. For Scenario 7, the RVE approach reaches its representational limits as the material becomes fully fused, resulting in a mix of failure mechanisms.

However, this limitation only applies to temperatures exceeding the recommended range for FDM printing of commercial filaments, which approaches the material's printability threshold. Thus, the model's predictive capabilities remain promising within the appropriate temperature range.

A common application of the RVE approach consists in the goal of obtaining a homogeneous material with the same properties as the modeled unit-cell. Thinking for example of Finite-Element simulations, it would be possible to assign to the material properties of the simulated component those obtained from the homogenization of a unit-cell where all the features typical

of MEX additive manufacturing are deeply evaluated. In this way, not only it is possible to quantitatively consider the additive nature of the part, but the numerical analysis would be much quicker and lighter as only the geometry at the macro-scale is to be modeled, with all the properties derived from the preliminary unit-cell study. Resuming, the ABS behavior at the micro-scale is imposed and the RVE response, through loading-displacement curves and elastic constants, is obtained from the meso-scale behavior aimed at the description of the macro-scale behavior. To do so, six independent strain fields are separately applied to the RVE, three in tension and three in shear mode, and the corresponding directional stress components developed in the RVE are extracted. Obtained numbers are the so-called "Engineering Constants" E_1, E_2, E_3, G_{12}, G_{13}, G_{23} and ν_{12}, ν_{13}, ν_{23} Poisson's ratios, obtained from the compliance matrix C^{-1} expressed in Equation 2.12:

$$\begin{bmatrix} \bar{\varepsilon}_{11} \\ \bar{\varepsilon}_{22} \\ \bar{\varepsilon}_{33} \\ \gamma_{12} \\ \gamma_{13} \\ \gamma_{23} \end{bmatrix} = \begin{bmatrix} \frac{1}{E_1} & -\frac{\nu_{21}}{E_2} & -\frac{\nu_{31}}{E_3} & 0 & 0 & 0 \\ -\frac{\nu_{12}}{E_1} & \frac{1}{E_2} & -\frac{\nu_{32}}{E_3} & 0 & 0 & 0 \\ -\frac{\nu_{13}}{E_1} & -\frac{\nu_{23}}{E_2} & \frac{1}{E_3} & 0 & 0 & 0 \\ 0 & 0 & 0 & \frac{1}{G_{12}} & 0 & 0 \\ 0 & 0 & 0 & 0 & \frac{1}{G_{13}} & 0 \\ 0 & 0 & 0 & 0 & 0 & \frac{1}{G_{23}} \end{bmatrix} \begin{bmatrix} \bar{\sigma}_{11} \\ \bar{\sigma}_{22} \\ \bar{\sigma}_{33} \\ \bar{\sigma}_{12} \\ \bar{\sigma}_{13} \\ \bar{\sigma}_{23} \end{bmatrix} \tag{2.12}$$

The compliance matrix is the inverse of the stiffness matrix $\bar{C}$: coefficients of $\bar{C}$ are obtained performing the ratio of the volume average of corresponding stress component in RVE over the corresponding elementary strain applied in RVE, as resumed in Equation 2.13:

$$\bar{C}_{ij} = \frac{\bar{\sigma}_{ij}}{\varepsilon_{ij}} \quad \text{where} \quad \bar{\sigma}_{ij} = \frac{1}{V_{\text{RVE}}} \int_V \sigma_{ij} \, dV \tag{2.13}$$

Operatively, the homogenization task is performed through *Micromechanics* Plugin in ABAQUS environment. As a result, the homogenized elastic properties of the RVE can be assigned to a printed component as descriptive of the behavior at the macro-scale, once the local direction of printing is known, for example by adopting an anisotropic material model. When the

six independent strains shown in Figure 2.16 are applied to the RVE, the compliance matrix of Equation 2.14 is obtained.

$$C = \begin{bmatrix} 1221.2 & 320.98 & 462.65 & 0 & 0 & 0 \\ & 863.57 & 355.37 & 0 & 0 & 0 \\ & & 1461.9 & 0 & 0 & 0 \\ & & & 338.70 & 0 & 0 \\ & \text{symm} & & & 422.38 & 0 \\ & & & & & 462.65 \end{bmatrix} \tag{2.14}$$

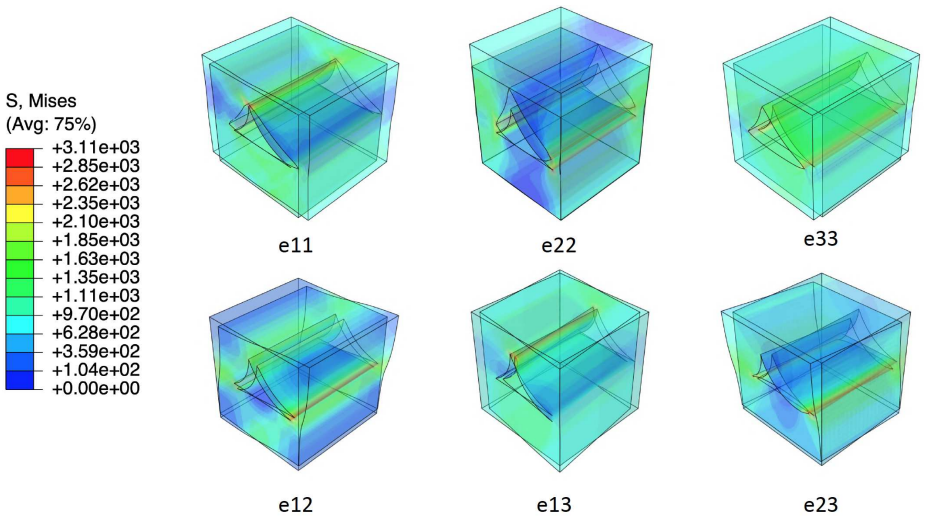

Figure 2.16: Deformation of the RVE with six independent applied strain conditions

What shown is the case of the FDM-printed ABS with 0.4 mm layer height. From that, the engineering constants of an equivalent homogenized material summarized in Table 2.3 can be drawn.

Table 2.3: Engineering constants from RVE homogenization

E_{11} [MPa]	E_{22} [MPa]	E_{33} [MPa]	G_{12} [MPa]	G_{13} [MPa]	G_{23} [MPa]
1014.5	736.5	1216.4	336.6	421.8	342.3

To resume the content of this section, the influence of key adjustable parameters (layer height, nozzle temperature, and raster angle) on the tensile behavior of FDM-printed specimens is analyzed and modeled. Based on microscope observations of cross-sectional morphology, an RVE is defined that incorporates the geometric characteristics alongside a novel approach to damage initiation and progression. Specifically, plasticity originates from the filament material at the micro-scale, whereas at the mesoscale, damage onset and evolution are controlled by the printing path. These mechanisms are triggered by the stress state and the relative orientation between the principal stress direction and the filament deposition direction.

The most important finding is that the raster angle is the primary factor influencing the failure mechanism, while the nozzle temperature only contributes to potential premature failure. The layer height has little impact on the behavior during the damage phase. On top of this, the main finding is found in the multi-scale approach combining RVE technique and CZM elements: this is effective in accurately reproducing the response of components produced via FDM technology. Also, an homogenization process can follow, paving the pathway for new modeling strategies to study the macro-scale response of additively manufactured components by assigning homogenized properties.

2.3 Damaging of Cellular Structures

In Section 2.2, a promising approach to characterize components fabricated through FDM technology has been widely discussed, finding its basis on the multi-scale modeling of the additively manufactured material. However, this methodology starts with the definition of the unit-cell from microscope observations of the cross-sectional morphology of the sample: the underlying hypothesis is that the component at the macro-scale can be reproduced by the three-dimensional face-to-face tessellation of the modeled RVE. This is more than reasonable when thick, 100% density filled, parts are considered. But for objects with complex geometries, available thanks to the recent huge development of 3D-printing, such as the cellular structures introduced in Section 1.1, the assumption is no more completely valid. Cellular solids, indeed, are characterized by thin walls, which make them achieve very desirable light weight and optimize the effective stiffness ratio. In particular, the lower the relative density of the cell, the closer the behavior to effective meta-materials, extending their applicability to a wide range of applications including dampers, shells and functionally-graded structures thanks to their capacity to absorb a large amount of energy prior to failure.

Even for these kind of structures, the mechanical response depends on the direction of loading with respect to the deposition direction, as worse bonding between filaments across different layers compared to those in the same layer is typical. This aspect is influenced by many parameters, the most important of which is the printing path; this has already been investigated in the previous section. As a result, FDM parts can be classified as anisotropic at a certain level, which in turn depends on the process parameters employed.

Studies examining the failure of lattice structures have found that the relative density and unit cell geometry play an important role in determining the failure behavior of the whole lattice structure [55, 56], as well as the fracture toughness [57]. Solutions employing small cells are useful to avoid

low-strain structural failures, while post-manufacture heat treatments can prevent the formation of shear bands giving rise to a plateau stress-strain behavior usually associated with ideal deformation in cellular solids [58]. However, no specific references have yet been made to the effect of layer deposition on damage initiation and fracture behavior in such structures.

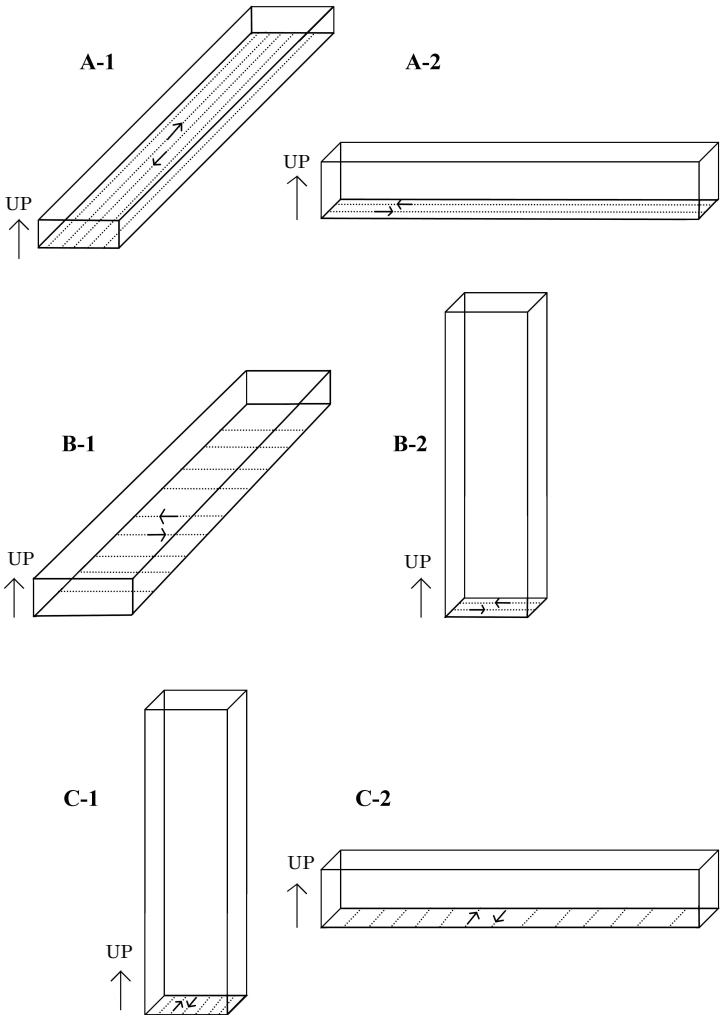

Figure 2.17: Prismatic samples with different filament deposition strategies

This section opens with an investigation of the anisotropy consequent to the filament deposition process. Later, this will be correlated with that of a bio-inspired lattice structure, and a model of the mechanical response up to the damage regime will be developed.

A preliminary study is performed on small prismatic specimens fabricated in ABS with all possible build orientations to determine the elasticity and strength of each. Samples with the configurations in Figure 2.17 are loaded in a 3-Point-Bending (3PB) configuration, see Figure 2.18(a), on a Ametek Chatillon TCD225 Series Force Measurement System equipped with a 1kN loadcell, see Figure 2.18(b), using a velocity of $8.33e^{-2}$ mm/s.

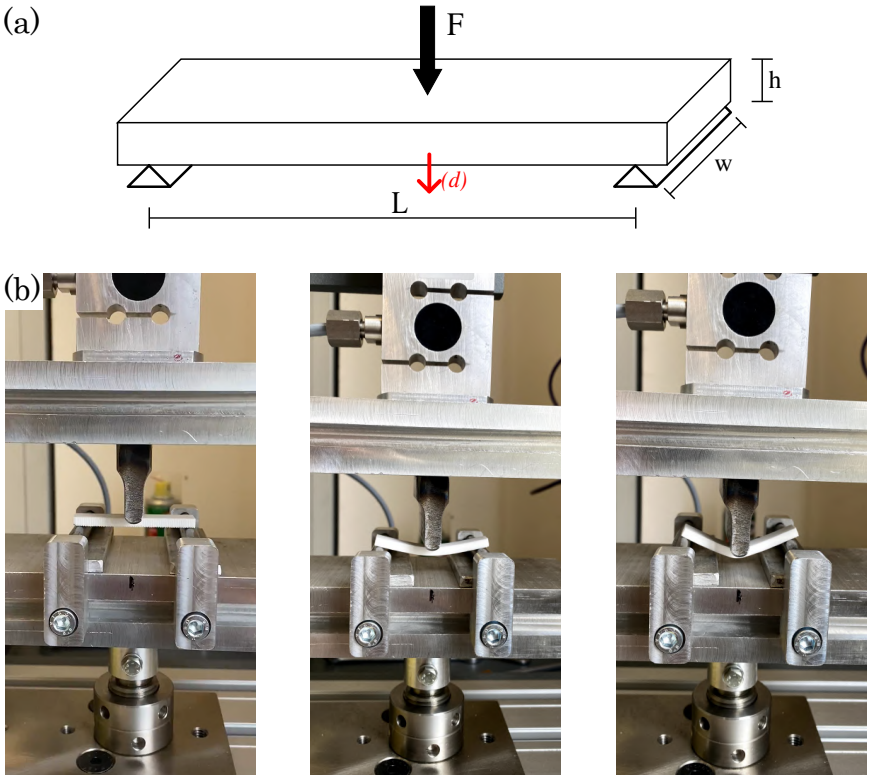

Figure 2.18: 3-point-bending test: a)Load scheme; b)Experimental setup.

ABS is characterised by a significant plastic regime, up to 6-7% of strain, responsible of the remarkable toughness of this material. Such characteristics can be observed in Figure 2.19(a) for flexural tests performed on sample A1, where filaments are deposited in the longitudinal direction. Sample groups B and C instead exhibit brittle behaviour, as seen in the same figure, as the resistant sections are characterised by bonding between adjacent filaments and consequent surface adhesion and molecular diffusion of the material.

Scanning electron microscope (SEM) analysis of group B and C sample fracture surfaces in Figure 2.19(b) confirms the aforementioned trend. Fracture takes place between two adjacent layers, with cracks starting from the notch generated by the bonding of two filaments. The fracture surface is smooth and exhibits the unique aspects of brittle fracture, confirming the observed response.

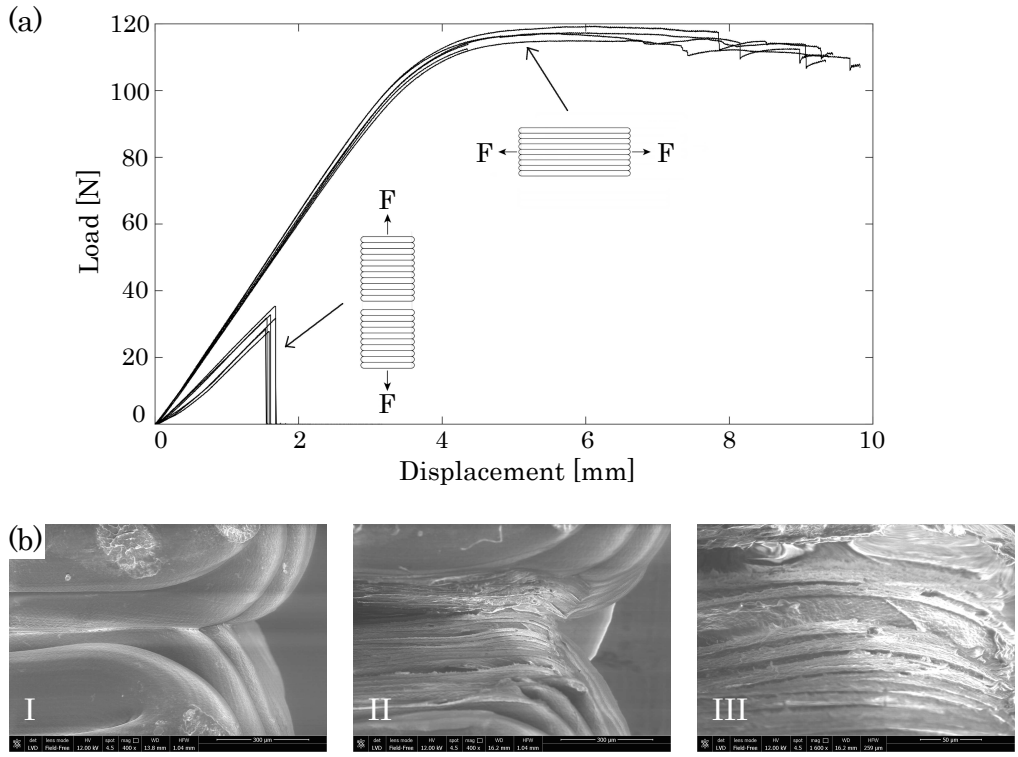

Figure 2.19: Mechanical flexural response of tested specimens: a)Load-displacement curves; b)SEM images of the fracture surface.

Load-displacement data are processed to determine the maximum bending stress, $\sigma_{u,flex}$, and flexural modulus, E_{flex}, using Equations 2.15 and 2.16:

$$\sigma_{u,flex} = \frac{M_{flex}y}{J} = \frac{3FL}{2wh^2} \tag{2.15}$$

$$E_{flex} = \frac{L^3F}{4wh^3d} \tag{2.16}$$

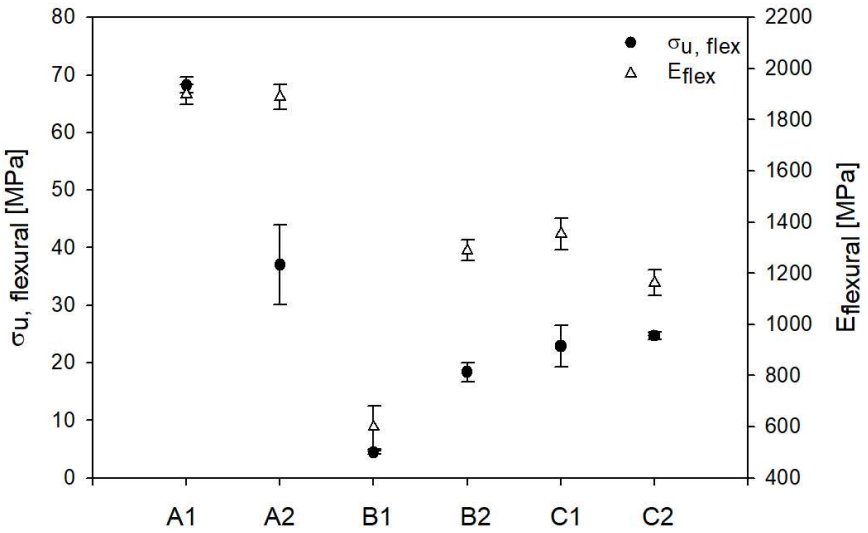

Figure 2.20: Flexural elasticity and maximum bending stress for different specimens groups

Average results for each group are presented in Figure 2.20, together with the corresponding error bands. As expected, samples in group A are the strongest and stiffest, as the material deposition direction coincides with the bending stress principal direction. As can be observed, variability of the quantities is nonetheless high. This preliminary result is important because it provides a ratio between the elastic properties of ABS samples produced via FDM with loading in different orientations, necessary to model and characterize the anisotropy of FDM-printed ABS.

As anticipated at the beginning of this section, focus is set on parts with complex geometries like cellular solids. The lattice structure under consideration originates from the face-to-face tessellation of a unit cell in three-dimensional space. By considering bio-mimicking theory, the unit cell is inspired by nature, representing the morphology of a sea-urchin skeleton in an "open" configuration with holes in the planar faces [59]. The way to generate the unit-cell geometry, explained in Figure 2.21, consists in a trim-mirror-merge-tessellate process; unit-cell dimensions are 8x8x8 mm.

In relation to lattice compression, the load-displacement curve is repre-

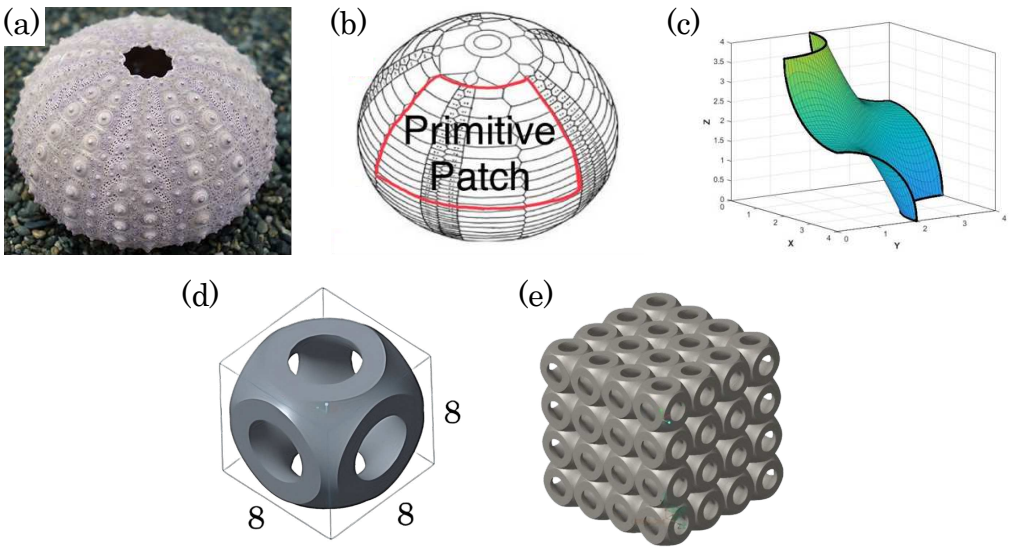

Figure 2.21: Bio-mimicking process for the structure design: a)Sea-urchin skeleton; b)Primitive path; c)Mirroring and merging; d)Unit-cell geometry; e)64-cell structure.

sented in Figure 2.22(a). At the beginning of the test (points 1-2) up to about 6.6% global deformation (point 3), the structure behaves as a spring and the behavior is therefore linear elastic. This region is followed by a decrease in load (points 4-6) when damage begins to occur. The densification regime is then encountered, with the load increasing again rapidly; however, this region is out of the interest of the present case. Direct correlation with the points shown in the load-displacement plot can be seen in photos in Figure 2.22(b) taken at different instants during the test.

It is possible to observe both initiation of a crack in the external wall of the cell and damage between cells caused by lateral deformation of the structure. From this point onwards, some cells completely collapse, leading to a decrease in the response curve up to 19% deformation (point 6), where the structure is functionally damaged.

Moreover, what is of primary interest in this section, is to understand the damage mechanism that affects this kind of structures and its relationship with the FDM fabrication parameters. By observing SEM images of the fracture surfaces, two damage mechanisms are identified. The first, shown

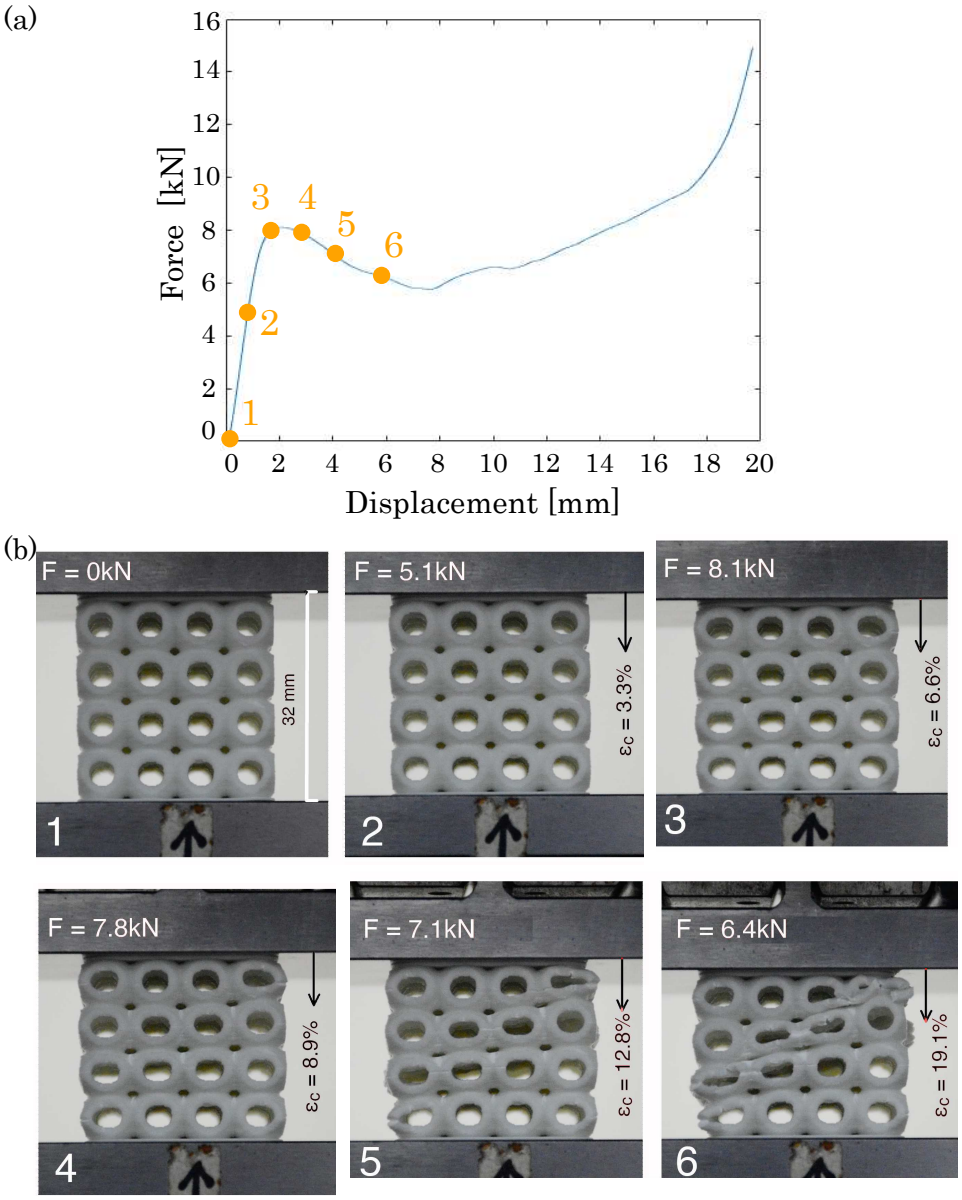

Figure 2.22: Compression test on cellular structure: a)Mechanical response; b)Frames at different nominal compression stages.

in the upper images in Figure 2.23, is the initiation and propagation of a crack across a filament. The macroscopic effect of filament cracking in the direction normal to deposition in different layers can be referred to as "intra-layer damage".

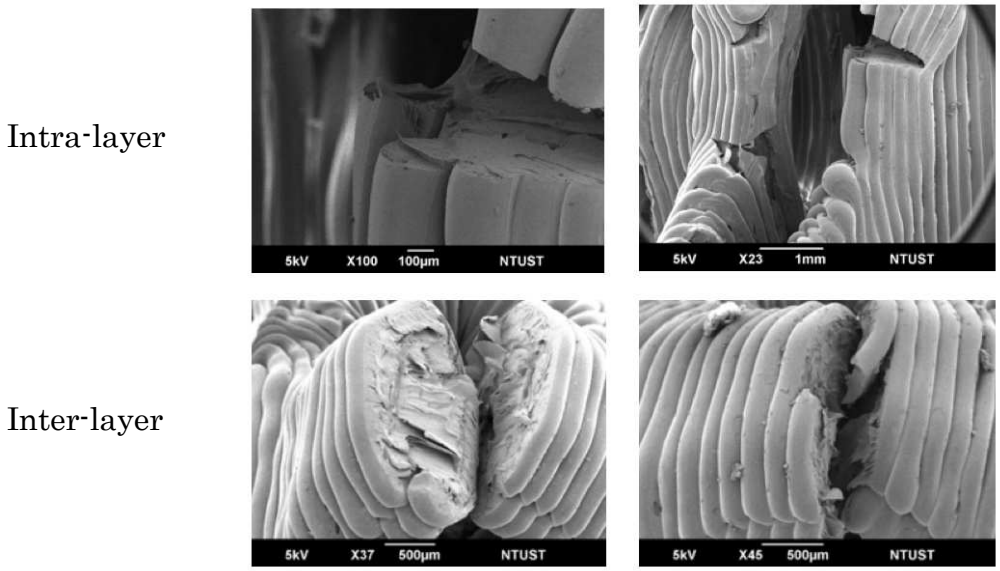

Figure 2.23: SEM images of inter- and intra-layer fracture mechanisms

The second mechanism, illustrated in the lower images of Figure 2.23, causes the separation of two adjacent layers by breaking the bonds between filaments. This phenomenon is referred to as "inter-layer damage." This type of damage is responsible for the initial failure during compressive tests, as the material is weaker in this direction. However, the first mechanism to occur is intra-layer damage, though it does not cause the initial failure. As shown in Figure 2.22(b), material degradation appears between two adjacent cells in the second frame, while crack formation only becomes visible in the third frame, when the internal damage is already substantial. From these results, two key conclusions can be drawn: *i*) FDM-printed parts exhibit at least two distinct damage mechanisms, i.e. inter-layer and intra-layer damage, and *ii*) the strength of the resulting structure is closely linked to the filament deposition order, direction, and the stress distribution influenced by loading and geometry. Knowledge of this relationship and definition of an optimum deposition path are key to defining and optimising the mechanical response of such structures.

To this end, a numerical simulation is developed in the ABAQUS environment in parallel with the compressive tests. ABS is modeled with an

orthotropic constitutive law, in line with observations relating to the material deposition process. Specifically, a transversely isotropic constitutive model is the most suitable for components produced via FDM. This means that material properties are symmetric about an axis normal to a plane of isotropy. In the present case, the plane of isotropy coincides with planes parallel to the basis of the structure, meaning that the material inside each layer is considered as isotropic. Equation 2.17 shows the constitutive matrix for transversely isotropic elasticity, with indices p and t representing the plane of isotropy and transverse direction, respectively.

$$\begin{bmatrix} \varepsilon_{11} \\ \varepsilon_{22} \\ \varepsilon_{33} \\ \gamma_{12} \\ \gamma_{13} \\ \gamma_{23} \end{bmatrix} = \begin{bmatrix} 1/E_p & -\nu_p/E_p & -\nu_{tp}/E_t & 0 & 0 & 0 \\ -\nu_p/E_p & 1/E_p & -\nu_{tp}/E_t & 0 & 0 & 0 \\ -\nu_{pt}/E_p & -\nu_{pt}/E_p & 1/E_t & 0 & 0 & 0 \\ 0 & 0 & 0 & 1/G_p & 0 & 0 \\ 0 & 0 & 0 & 0 & 1/G_t & 0 \\ 0 & 0 & 0 & 0 & 0 & 1/G_t \end{bmatrix} \begin{bmatrix} \sigma_{11} \\ \sigma_{22} \\ \sigma_{33} \\ \sigma_{12} \\ \sigma_{13} \\ \sigma_{23} \end{bmatrix} \tag{2.17}$$

Two damage variables d_p and d_t are defined, referring to the plane of isotropy and the printing direction, respectively. In relation to the first one, a threshold strain value $\varepsilon_{th,p}$ is defined for triggering damage initiation measured by the variable d_p, which takes on a value ranging of 0 for no damage and 1 for a fully damaged material. When the maximum principal strain is equal to the condition for damage initiation, $\varepsilon_p = \varepsilon_{th,p}$, the damage variable is computed and the elastic properties of the material are modified, as will be discussed further. The evolution of damage is then defined according to classical continuum damage models [60], with a kinetic law in the form:

$$\text{for} \quad \varepsilon_{th,p} < \varepsilon_p \leq \varepsilon_{f,p} \qquad d_p = 1 - \left(1 - \frac{ln\dfrac{\varepsilon_p}{\varepsilon_{th,p}}}{ln\dfrac{\varepsilon_{f,p}}{\varepsilon_{th,p}}} \right)^{\alpha_p} \tag{2.18}$$

with $\varepsilon_p = \varepsilon_{f,p}$ the condition for the complete failure of the material.

Conversely, looking back to the 3PB experimental responses in Figure 2.19, the material behaves as brittle in the direction normal to the layers, i.e. in the building direction of the 3D-printing process. Failure is therefore considered to take place without any previous material degradation based on the rule:

$$d_t = \begin{cases} 0 & \text{if} \quad \varepsilon_t < \varepsilon_{f,t} \\ 1 & \text{if} \quad \varepsilon_t \geq \varepsilon_{f,t} \end{cases} \tag{2.19}$$

These formulations result in a one-to-one correspondence between the strain and elastic properties in the considered direction:

$$\text{for } i = p, t \qquad E_{d,i} = E_i \ (1 - d_i) \tag{2.20}$$

where E_d and E represent the elastic modulus of the damaged and safe material in the considered direction respectively, according to the transversely isotropic behavior previously discussed.

The numerical implementation of this anisotropic damage model is achieved through a USER SUBROUTINE code, in which the local tensile strains at the centroid of each element are extracted for each increment and placed within the damage variable formulation. The use of tensile strain comes from an analysis of the structure showing that material failure takes place due to local tensile stresses. When $d = 1$, i.e. when the failure strain value of ε_f is attained, the element completely loses its load-bearing capacity and is therefore suppressed from the analysis.

The FE simulation adopts a mesh comprising C3D8 elements, with the mesh density selected as a trade-off between accuracy and computational time. Optimal results are considered as those presenting low variability during sensitivity analysis. The set of material data and damage parameters used in the numerical simulation is reported in Table 2.4, with reference to the previously shown results of 3PB tests on prismatic specimens.

Simulation outputs are presented in Figure 2.24, in which the experimental and numerical mechanical responses are compared.

Table 2.4: Material parameters adopted in the numerical simulation

Parameter	**Isotropy plane**	**Transverse direction**
Young's modulus E [MPa]	1500	1300
Poisson's ratio ν [-]	0.3	0.3
Shear modulus G [MPa]	576.9	500
$\varepsilon_{f,t}$	0.016	
$\varepsilon_{f,p}$	0.055	
$\varepsilon_{th,p}$	0.008	
α_p	0.55	

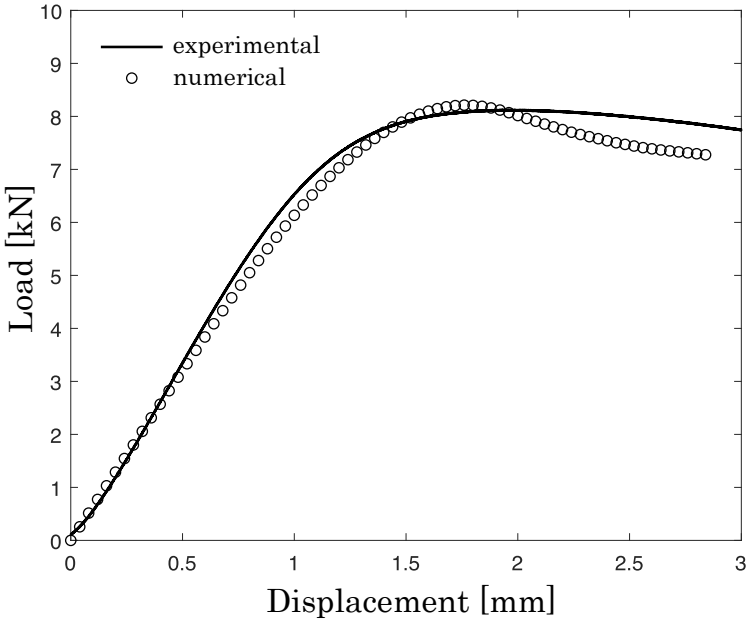

Figure 2.24: Match between numerical and experimental curves

Good alignment is observed, indicating that the two damage mechanisms numerically implemented affect the structure similarly to experiments. This can be seen as an additional validation of the numerical model; as noted previously, the condensation regime is not taken into consideration. In addition to the comparison of load-displacement curves, experimental frames of the structure deformation from 2.22(b) are compared with simulation frames at the same nominal strain levels. The failure mechanisms of the lattice structure are very well reproduced by simulation outputs, further validating the

numerical model. This allows to plot contours of the damage variable during the compression test, see Figure 2.25.

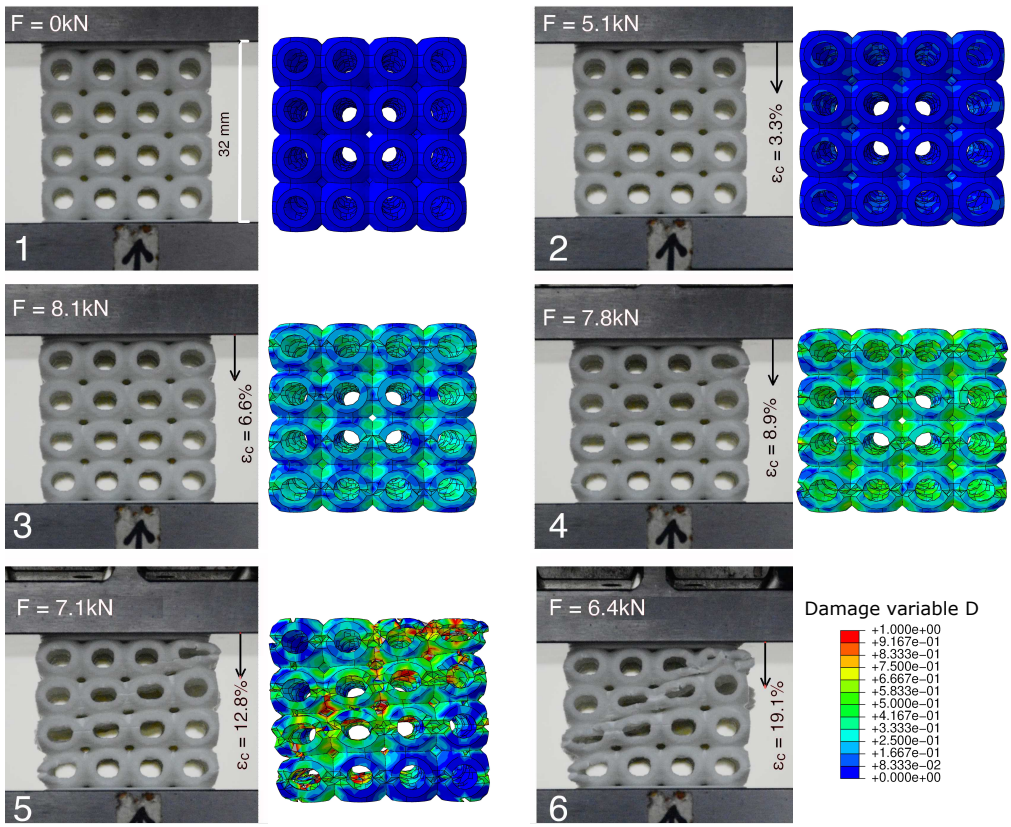

Figure 2.25: Damage in the structure at increasing nominal compression values and validation against experimental frames

Phenomena related with damage appearance and evolution are correctly predicted in terms of both location and strain level. Inter-cell damage, responsible for local material degradation, firstly appears at the upper right corner, followed by intra-cell cracks that are generated by bending stress in the external cell walls. Increasing the compressive strain, the full set of cells fails at the outer perimeter as a result of the bending load, with the maximum principal stress being tensile and inter-layer. Finally, at even higher levels of nominal strain, a 45° band is generated, corresponding to the ultimate strength of the structure.

A macroscopic 45° failure band evidences how the stress field is not the same for every single cell but, depending on the sample size and on the contact interaction-friction with the compressive plates, some recurrent failure trends at the macro-scale take place, as reported also for other lattice geometries [55, 56, 58, 61], depending on the loading conditions on the cellular solid.

Summarizing the content of this section, an anisotropic damage model, ductile and brittle in different directions, is developed starting from the outcomes of an experimental campaign of bending tests. The proposed damage model is added to a transversely isotropic material constitutive model, properly tuned with inter- and intra-layer elasticity and failure strains obtained from simple prismatic specimens, and found to be effective in reproducing the cellular structure mechanical behavior also in damage regime including fracture phenomena.

2.4 Conclusions

This chapter focused on the mechanical behavior of 3D-printed materials via Material Extrusion techniques. The elasticity of the safe material is studied, taking into account all the influences of the process parameters on the resulting properties of the FDM-ed part, but the attention is mainly put on the the damage regime, including the failure mechanisms at play.

Two novel approaches are proposed in this chapter: *i*) a multi-scale methodology to model components fabricated through FDM technology, and *ii*) a directional damage model useful to capture the fracture mechanics of thin-walled complex geometries.

In the first, the combined RVE-CZM approach, based on microscope observations, is both accurate and cost-effective. It is proved to accurately correlate the main controllable printing parameters (deposition strategy and extrusion temperature) with the predominant damage mechanism depending on the loading condition. This approach is potentially extremely useful as it addresses the actual problem of the modelling of additively manufactured parts. In other words, it allows to consider the effect of the deposition process (and its main controllable parameters), differentiating from the tradition bulk materials obtained in subtractive or formative ways, both in terms of material characterization and of damage and fracture mechanisms.

In the second, the developed transversely isotropic damage model is applied to a bio-inspired cellular structure subjected to compressive loading. This model is proved to be a reliable tool to assess the integrity of structures fabricated via material extrusion process. In particular, it extends the applicability range of the previous RVE-based multi-scale approach to the more complex, thin-walled, architectures where the tessellation of a unit cell is no more valid to represent the part geometry. Once again, the material deposition strategy plays a key role, being responsible for the part anisotropy, and consequently for which of the two different process-dependent damage mechanism, almost independent from one another, is predominant depending on the resulting stress field. As a result, advanced Finite-Element damage

models like this one, once accurately tuned, can contribute to more reliable simulations of crack initiation and failure in structures characterised by different levels of anisotropy and damage thresholds, depending on the printing process.

Future further developments will add more complexity to the models presented in this chapter, hopefully integrating the nozzle trajectory during the printing process directly from the G-Code file to a full directional damage model ready to be used in FE environment.

Novel Kirigami Meta-Materials

3.1 The Kirigami World

Kirigami, "cut-paper" in Japanese, is an ancient art of creating beautiful decorations by simply cutting and manipulating a thin piece of paper. The seemingly infinite possibilities of developing 2D or 3D geometries by the kirigami principle have inspired countless implementations in our modern life, from children's pop-up books to art and architecture. Meanwhile, kirigami received a growing interest from the science and engineering communities, who are transforming this humble artistic activity into a framework for architecting, fabricating, and functionalizing a wide variety of engineered systems like flexible electronics, meta-materials, shape-morphing structures, and soft robotics [62, 63, 64].

Before moving deeper into all the disciplines that benefit from kirigami-based new devices, the basic principles underlying kirigami astonishing properties are worth being briefly introduced.

The deformation mechanisms of kirigami meta-materials, realized by perforating rational patterns into flat sheets, are governed by the cut patterns, the ratio of the critical size of the cuts (i.e., the hinge size or the distance between parallel cuts) to the sheet thickness, and the applied boundary conditions. Hence, the design of kirigami is intrinsically scalable and generically material-independent. Following this, the main difference from origami ("folding paper" in Japanese) comes straightforward. While origami periodic and tessellated meta-materials with stiff facets are kinematically over-constrained systems, reducing the overall degree of freedom, kirigami cutting introduces the opposite effect via releasing the continuous constraint in the constituent sheet material and significantly increasing the kinematics degree of freedom. As a result, the essential principle of kirigami is powerful for imparting compliance to nearly inextensible flat sheet, providing the ability to stretch, conform, and adapt, while origami typically creates load-bearing devices and space-filling three-dimensional topologies.

Another unique characteristic of kirigami is its scalability in fabrication and working principle. A cut and stretched micrometer-scale kirigami spring

made out of graphene [65] follows a similar working principle as a centimeter-scale kirigami cutout of plastic [66], or even a meter-scale architecture [67], see Figure 3.1.

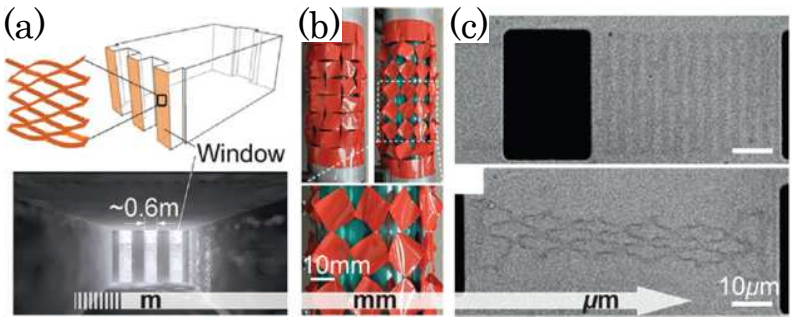

Figure 3.1: Kirigami at different length scales: a)Kirigami window shade for buildings, from [67]; b)Robotic kirigami skin made out of plastic sheets, from [66]; c)Kirigami spring based on graphene, from [65].

Many classifications are available in literature for kirigami structures: the most common are the one distinguishing between local movement and global shape change, and the one facing in-plane deformations and out-of-plane deformations leading to three-dimensional kinematics. In this chapter, the second classification is used, more useful to understand the content of the following sections.

Kirigami characterized by in-plane deformation rely on planar kinematics to achieve extreme mechanical and geometrical properties which are not seen in the initial, non-cut, sheet of material. Many of them rely on triangular or squared rotating units, which can also be cut as fractals to enhance even more their desired properties (Figure 3.2(a)). The regular cut pattern is often changed by an optimization or inverse design process to achieve target shapes [68]: the result is a mechanism that can easily switch between two 2D shapes by planar relative rotation of the rigid parts along small hinges (Figure 3.2(b)).

In the biomedical discipline, for example, wearable sensors, bio-electronics, and flexible displays, exploit kirigami' s ability to create controlled deformation patterns that can conform to complex surfaces. Examples of stretchable devices interacting with the human body are shown in Figure 3.2(c-d), with

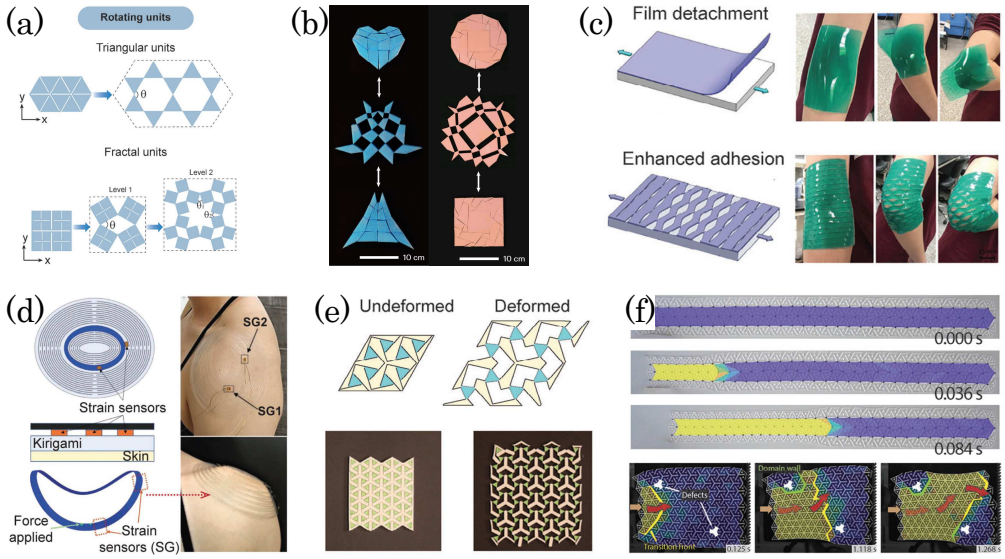

Figure 3.2: Kirigami with in-plane deformation: a)Triangular and fractal rotating units, from [62]; b)Kirigami mechanism to obtain target planar shapes, from [68]; c)Enhanced film adhesion with kirigami, from [69]; d)Kirigami flexible sensor, from [70]; e)Auxetic bi-stable kirigami, from [71]; f)Bi-stable kirigami for guided wave transition, from [72].

parallel [69] and concentric [70] cut pattern respectively. 2D kirigami's unique properties are not limited to planar shape reconfiguration capability and high conformity to non-planar surfaces. More in the mechanical field, auxeticity and bi-stability are among the most promising kirigami characteristics. Auxetic structures expand when stretched and shrink when compressed, achieving a negative value for the Poisson ratio. Bi-stable auxetic kirigami inspired by ancient art motifs [71] are shown in Figure 3.2(e); the same geometry can harness the transition energy between the two stable states for elastic wave guidance in dynamic applications [72], see Figure 3.2(f).

Considering now the kirigami family characterized by out-of-plane deformations, different mechanical and functional properties are achieved by this group of meta-materials. The interesting properties are not limited to the structure kinematics and its geometrical-mechanical behavior: the three-dimensionality of these kirigami when stretched opens a wide range of new possible applications. Some of the most known applications from literature

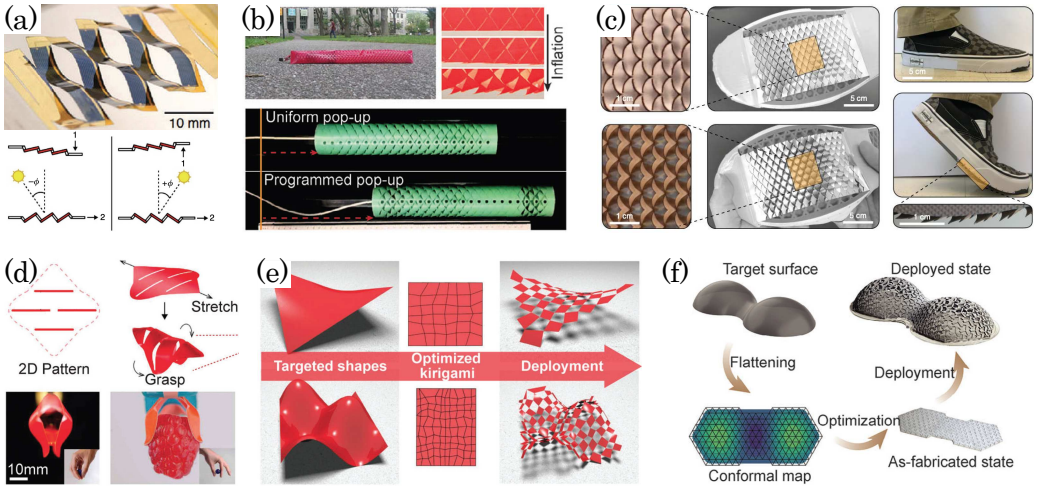

Figure 3.3: Kirigami with out-of-plane deformation: a)Kirigami for dynamic solar tracking, from [73], b)Crawling locomotion for soft robots, from [74]; c)Kirigami assistive shoe grip, from [75]; d)Grasping with kirigami shells, from [76]; e)Three-dimensional shape-morphing via kirigami design, from [77]; f)Shape-morphing structures via periodic tessellation of cells with different sizes when deployed, from [78].

are here presented. The integration of kirigami into energy systems has enabled advancements in stretchable energy storage devices. In Figure 3.3(a) kirigami-based solar cells have been designed to dynamically track solar positions, optimizing energy capture through their ability to deform and orient with respect to light sources [73]. In soft robotics, kirigami-based structures are utilized to develop tunable, reptile-inspired locomotion systems that can adapt to various environmental constraints [74], as the one in Figure 3.3(b); this concept can be extended also in devices interacting with humans, such as the assistive shoe grip of Figure 3.3(c) helping in preventing slides and falls [75]. All these examples are based on the local out-of-plane displacement of units mainly due to the twisting of the hinges. Other concepts are based on the global 3D shape of the final kirigami structure, initially a planar thin sheet. Soft robotics discipline can also benefit of this to develop kirigami-based soft grippers with localized mechanical compliance [76] which allows for the creation of actuators with tunable stiffness and large deformation ca-

pabilities, see Figure 3.3(d). Generalizing further, optimized cut patterns can be employed to achieve a desired target shape when activated [77], as those shown in Figure 3.3(e). Similarly, in Figure 3.3(f) playing with the geometrical parameters of a fixed bi-stable unit-cell, different expansion ratios can be achieved, leading to the design of responsive and deployable structures in architecture [78]. Leveraging kirigami's capacity for shape transformation, engineers can design lightweight, adaptive architectural systems that respond to external stimuli: dynamic facades, adaptive shading devices, and deployable shelters are only some examples.

In conclusion of this literature review paragraph, it is possible to state that kirigami has emerged as a powerful design paradigm in engineering, offering a framework for developing highly adaptable, functional, and mechanically versatile systems. By harnessing the interplay between geometry and material properties, kirigami is continuously riving advancements across many different engineeristic sectors, positioning itself as a pivotal tool in modern material and structural design.

In the following sections of this chapter, the effect of the geometrical parameters ruling the out-of-plane displacement on the mechanical response and, in particular, on the bi-stability of the kirigami unit-cell will be deeply investigated. This will be the basis for a new design strategy for multi-stable aperiodic kirigami meta-materials. In the state of the art, bi-stable kirigami meta-materials are limited to periodic planar tessellation of a bi-stable unit cell, like the one in Figure 3.2(e-f). The extension of the design space to aperiodic tilings is going to define a significant advancement in the employment of kirigami in the technology world.

3.2 A New Tile Definition

In this section, the new bi-stable tile developed in this work is introduced and mechanically characterized. More in details, the new tile definition comes from the unit-cell shown in Figure 3.4(a). The unit-cell corresponds to half of the kirigami Von Mises truss: Von Mises trusses are structures characterized by two stable states, arranged symmetrically with respect to the unstable equilibrium configuration, see Figure 3.4(b). The kirigami Von Mises truss is the building block for the proposed meta-materials. As it will be shown later in this Section, the new tile definition leads to peculiar unprecedented mechanical phenomena, which can be beneficially exploited to create a new class of kirigami meta-materials that overcomes some of the biggest limitations found in the literature available designs.

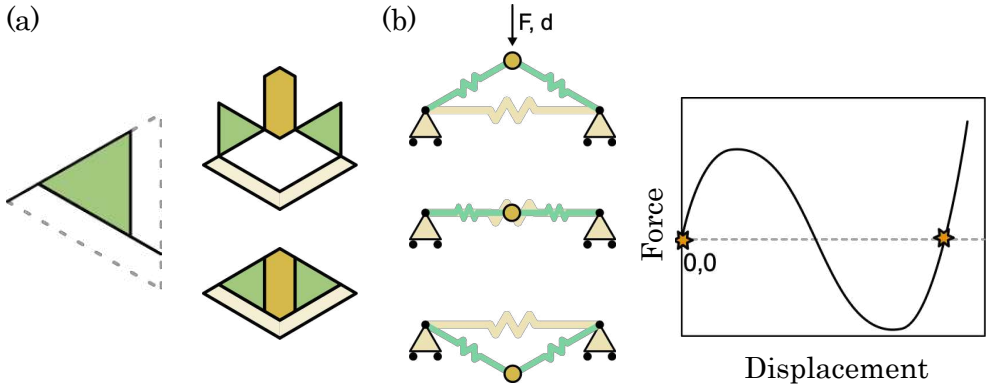

Figure 3.4: Mechanical bi-stability: a)The proposed new tile; b)Bi-stability of the Von Mises truss.

The unit-cell, schematized in Figure 3.5 is defined by its geometrical parameters: γ and β for internal angles, b for the cell side length, h for the hinge thickness, l_{RU} for the distance between the two hinges in each unit-cell. Three different parts can be identified inside the unit-cell: the rotating unit (RU), the rectangular pull tab and the base. The rotating unit is connected to both the pull tab of width $2d$, shared by two adjacent unit-cells, and to the bottom base, which for hypothesis should behave as a rigid part.

The hinges can bend consequently to the pull of the tab, the rotating unit can flex around them and the Von Mises truss can reach its expanded state.

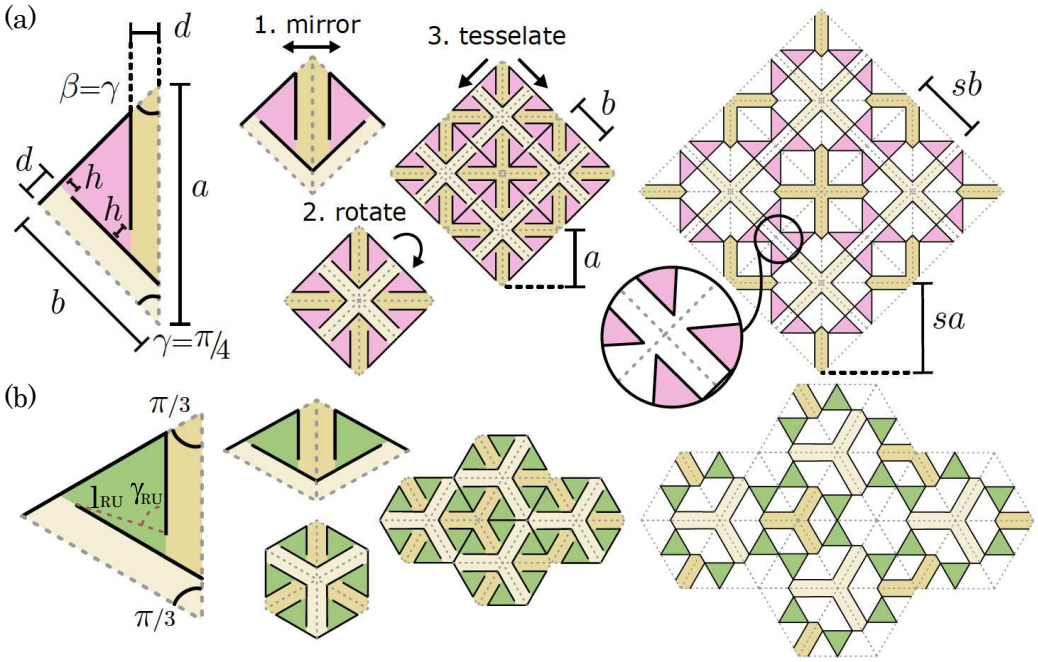

Figure 3.5: Kirigami periodic tessellations: a)Unit-cell with $\beta = \gamma = \pi/4$; b)Unit-cell with $\beta = \gamma = \pi/3$

Next, unit-cells are first mirrored and then rotated to generate a super-cell that can be tessellated in 2D plane to realize periodic kirigami meta-materials with two stable configurations, collapsed and deployed. Figure 3.5(a)-(b) show the results of a 2x2 edge-to-edge tessellation of square and hexagonal super-cells, obtained from unit-cells with $\gamma = \beta = \pi/4$ and $\gamma = \beta = \pi/3$, respectively, both in collapsed and expanded states. When deployed, the samples reach stable configurations that persist despite the removal of the load, confirming the bi-stability of the design. Following, it is necessary to define a parameter, function of the unit-cell geometry, to estimate the change in size between the collapsed and deployed configurations. The scale factor s, referring to the unit-cell side length a, is computed as:

$$s = 1 + 2\frac{l_{RU}}{a}\cos\gamma_{RU} \tag{3.1}$$

For the particular case of Figure 3.5 where $\beta = \gamma$, the scale factor equation can be written as:

$$s = 2 - \frac{d}{b}\left(\frac{1}{\sin(2\gamma)} + \frac{1}{\sin\gamma}\right) - \frac{3h}{b\,\sin(2\gamma)} \tag{3.2}$$

At this point, periodic samples (2x2 super-cells) undergo tensile tests to evaluate their mechanical behavior. Samples are obtained from a commercial rubber sheet 2.38 mm thick; kirigami cuts are made with a Universal Laser Systems PLS6.150D laser-cutting machine. Square super-cells are fabricated with cell side length $c = 10$mm, hinge thickness $h = 0.7$mm, and tab width $d \in (0.8, 1.0, 1.2, 1.4, 1.6, 1.8, 2.2, 2.4, 2.6)$mm, while triangular designs are constructed using $c = 12$mm, $h = 0.7$mm, and $d \in (1.0, 1.5, 2.0, 2.5, 3.0)$mm.

Periodic samples undergo mechanical testing as shown in Figure 3.6(a). Displacement-controlled tests are performed adopting two translation stages (Thorlabs LTS300) with a load cell (Futek LSB200), jointly controlled by a custom Python library. Two metal pins are used to fix the samples to the moving stages. A lubricated plate of acrylic is placed under the sample during the test, working as a support. A second lubricated plate of acrylic is positioned above the sample. Two different setups are indeed investigated: the "free" and the "confined" configurations. In the first one the sample is supported by the slide plate only, while in the second one the second plate at the top acts as a confinement against out-of-plane deformations. Both stages move at 0.5 mm/s, for a total extension rate of 1 mm/s.

Tensile tests start from the samples' initial length l_0 defined as $l_0 = 2b\cos\gamma$ and $l_0 = 3b\cos\gamma$ for square and hexagonal super-cells, respectively. To ensure that each sample is expanded fully and to a comparable degree, a maximal displacement u_{max} is defined for each structure, calculated using:

$$u_{max} = C(l_0 s_0 - l_0) \tag{3.3}$$

where $C = 1.1$ is a coefficient that quantifies the amount of over-extension from the size of the deployed configuration, and s_0 is the theoretical expansion factor considering the ideal case of zero-thickness hinges. For the periodic samples s_0 is determined via

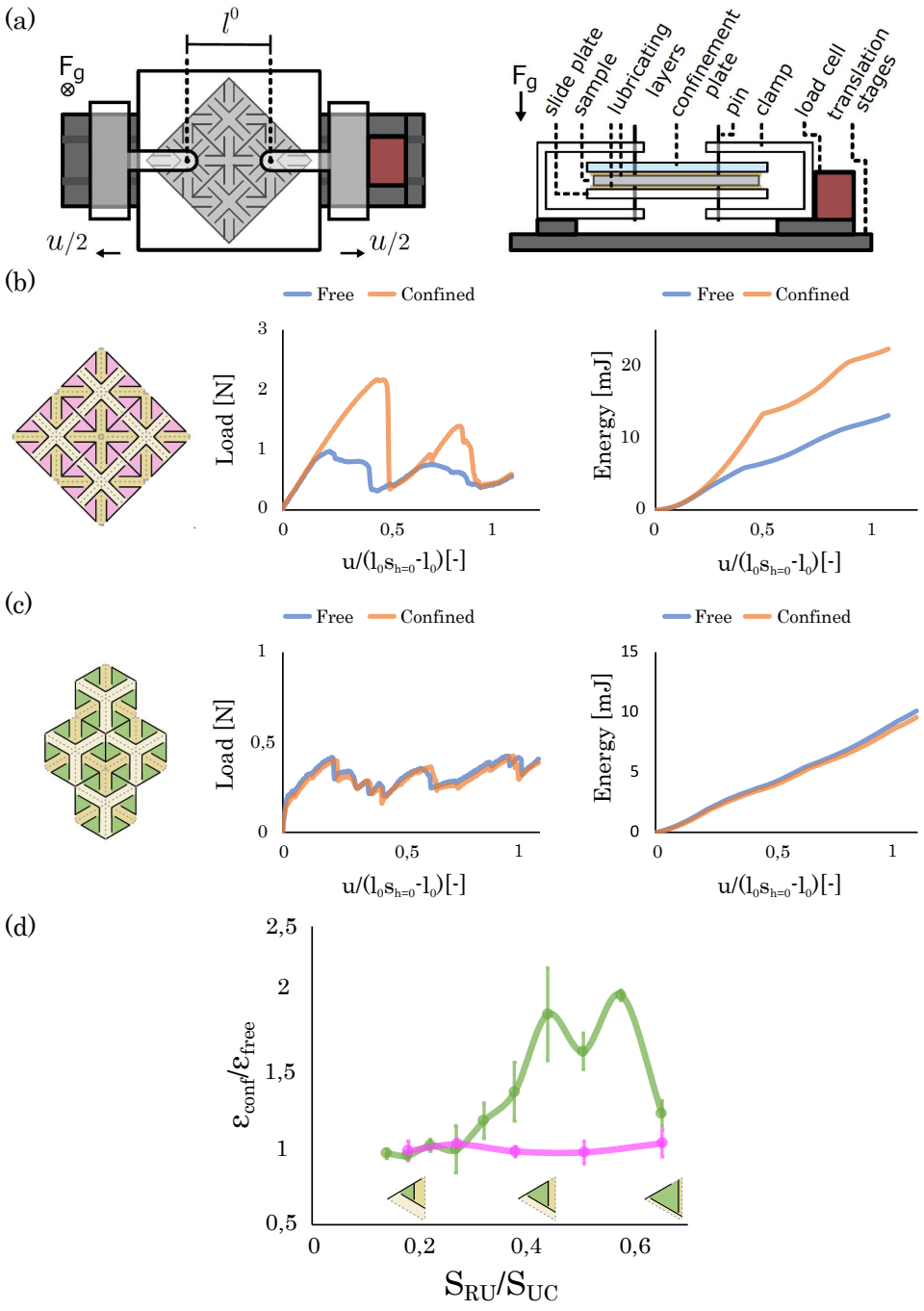

Figure 3.6: Mechanical testing of periodic kirigami: a)Test setup; b)Load and Energy for square super-cell; c)Load and Energy for hexagonal super-cell; d)Geometry effect on mechanical behavior.

$$s = 2 - \frac{4d}{\sqrt{3}c} \tag{3.4}$$

for triangular samples and

$$s = 2 - (1 + \sqrt{2})\frac{d}{c} \tag{3.5}$$

for quadrilateral tessellations.

Load curves plotted against normalized displacement are reported in Figures 3.6(b)-(c). The energy plot is easily obtained by integrating the force over the displacement. Results show remarkable drops in the load curve each time a snapping phenomenon occurs, validating the multi-stability of the specimen. On top of this, what is really interesting is the huge difference between the trends in "free" and "confined" configurations for the square super-cell samples (the total energy for the "confined" scenario is double the energy when "free"); this behavior is not evidenced in the hexagonal super-cell sample, where the two curves are coincident. The reason for this lies in the out-of-plane displacement during the deployment: the kirigami Von Mises trusses of the square sample show a strong tendency to pop-up during the transition between close and open equilibrium states. The confinement plate therefore forces them to stay planar, configuration which does not correspond to the minimum energy configuration. Figure 3.6(d) resumes the ratio between confined and free energy for different geometric parameters (ratio between surface of the rotating unit S_{RU} and the surface of the unit cell S_{UC}). While the unit-cell geometry does not affect the mechanics of the hexagonal samples, the choice of the unit-cell parameters plays a key role in the behavior of the square samples: the bigger the rotating unit, the stronger the out-of-plane tendency (excluding the last point of the plot where the unit-cell base, supposed to be rigid, bends significantly affecting the whole structure mechanics).

This curious behavior will be deeply investigated later in this section. Before that, it is worth showing the FE numerical model developed both to confirm what noticed in the experiments and to deeper analyze the stress field during and after the deployment. In the numerical environment, a

hyper-elastic second-order polynomial constitutive law is adopted to model the rubber behavior. The strain energy density function U for this model is given by:

$$U = \sum_{i+j=1}^{i+j=2} C_{ij}(\bar{I}_1 - 3)^i(\bar{I}_2 - 3)^j \tag{3.6}$$

where $\bar{I}_1$ and $\bar{I}_2$ are the first and second invariants of the isochoric part of the left Cauchy-Green strain tensor. The parameters C_{ij} represent the material's elastic properties, and are determined from a tensile test on standardized specimens (geometry according to ISO EN 527-1 type 1BA, extension rate of 1 mm/s). The resulting force-displacement curve and the match with the best fitting hyper-elastic constitutive law are shown in Figure 3.7(b). Values for parameters are resumed in Table 3.1.

Table 3.1: Coefficients of the hyper-elastic constitutive model

C_{10} [MPa]	C_{01} [MPa]	C_{20} [MPa]	C_{11} [MPa]	C_{02} [MPa]
−3.6828	5.4176	0.8757	−3.0356	3.7889

The density of the rubber is assumed to be 1.34 g/cm^3. The model's geometry is shown in Figure 3.7(a): half of the actual structure is modelled and symmetric boundary conditions are consequently added. A strain of ε = 0.7 is applied in displacement control. Dynamic Implicit solver is chosen, and CPS6M quadratic plane-stress elements are adopted for the mesh. To help convergence, material damping (Rayleigh model) is included, with parameters $\alpha = 0.988$ and $\beta = 0.001$.

As shown in Figure 3.7(c), both the load-displacement curve and deformation fields are excellently validated against experimental data in the confined configuration (so that only planar displacements are allowed). In addition, the FE simulation confirms what expected: during the deployment, stress concentrates in the hinges, and contact of the free vertex of the rotating units is responsible of a large energy barrier between sequential opening of individual trusses.

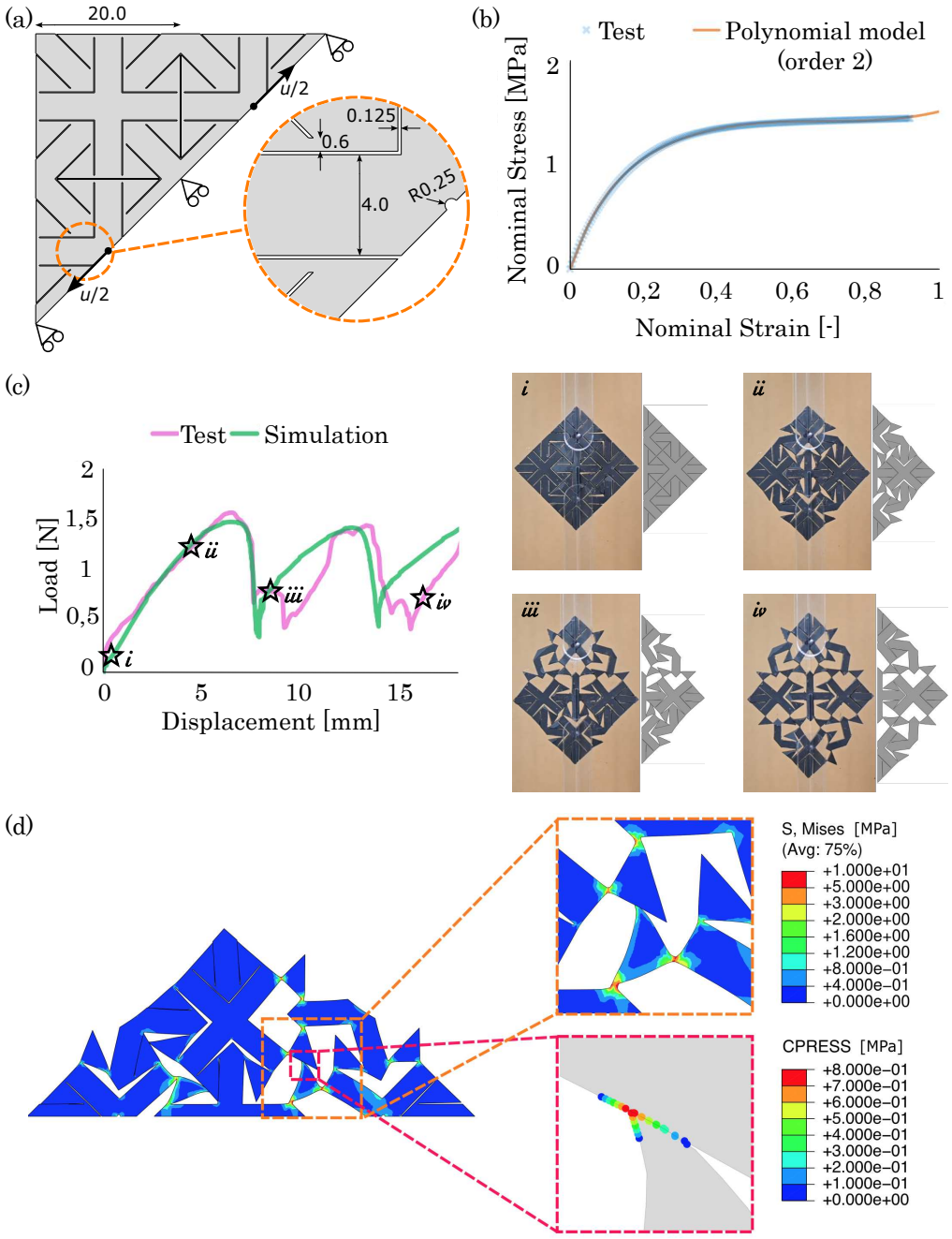

Figure 3.7: Finite-Element simulation of the Kirigami deploying process: a)Geometrical model; b)Material constitutive model; c)Match with experiments; d)Details of stress field concentration and contact pressure.

As mentioned previously, a deeper and more extensive investigation on the influence of unit-cell geometrical parameters on the resulting mechanical behavior is needed to fully understand the physics of these kirigami Von Mises trusses. The interest of this analysis mainly concerns the peculiar out-of-plane displacement during deployment and its proven correlation with the multi-stable behavior of the structure.

Individual kirigami Von Mises trusses are fabricated and undergo tensile tests (Figure 3.8(a)) with the exact same test conditions of the previously tested periodic meta-materials (Figure 3.8(b)). 12 designs are fabricated and tested, with varying γ and d, i.e. varying γ_{RU} and l_{RU}/l_{RU}^{max}, see Figure 3.8(c). $b = 24$ mm, $h = 0.7$ mm, and $\beta = \gamma$, are kept constant for all designs.

Results are reported in Figure 3.8(d): frontal picture of the samples are associated with their corresponding side picture when the maximum out-of-plane displacement occurs. When γ_{RU} is large and l_{RU}/l_{RU}^{max} is small, the truss moves in-plane and is mono-stable in the collapsed state (pentagonal marker). Oppositely, when γ_{RU} is small and l_{RU}/l_{RU}^{max} is large, the truss is stable in both collapsed and open configurations (star marker). Also, during the transition between these two extreme cases, a gradual increase in the out-of-plane displacement is evidenced.

A color is assigned to each marker to quantify the ratio between the maximum out-of-place displacement recorded during the test and the kinematically maximum out-of-plane rotation of the rotating unit: dark green corresponds to values close to 1, very light green to zero, meaning only in-plane displacement is noticed.

To understand the mechanics underlying this behavior, an analytical model is developed. In the model, each rotating unit is schematized as an axial spring with initial length l_{RU} oriented with an angle γ_{RU} with respect to the z-axis, see Figures 3.9(a)-(b). The rotating unit, subjected to axial compressive stress, acts as a spring with stiffness k_{RU}; one end is fixed, and the other is free to move in the y- and z-directions. In-plane and out-of-plane deformations are quantified via angles $\Delta\theta$ and $\Delta\tau$, respectively. These deformations are contrasted by two additional linear springs placed in correspondence of each hinge at the base, one for bending with stiffness k_θ and

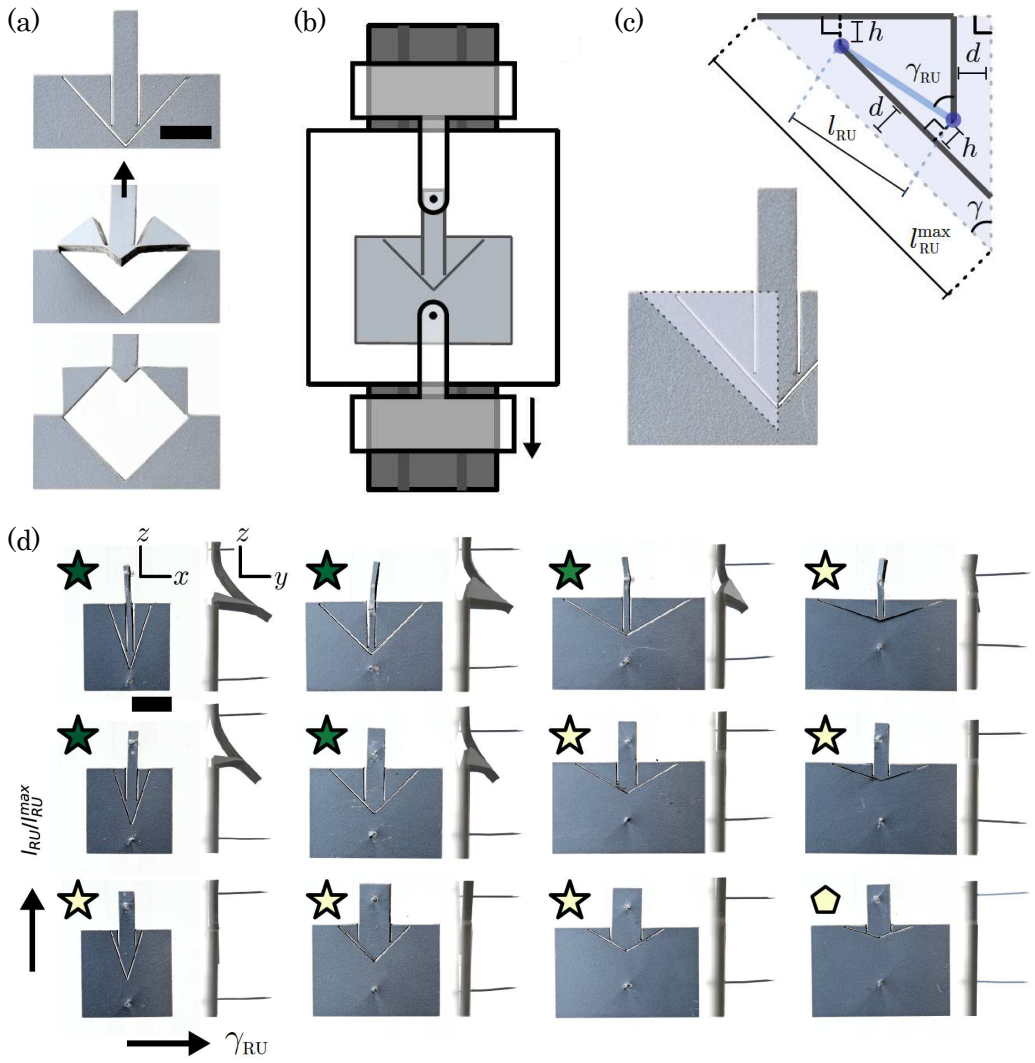

Figure 3.8: Mechanical testing of the kirigami Von Mises truss: a)Sample behavior; b)Test setup; c)Unit-cell parameters; d)Out-of-plane tendency for different geometries.

one for torsion with stiffness k_τ. Hence, the structure total elastic energy ε is defined by Equation 3.7, where the three terms represent stretching, in-plane rotations, and out-of plane rotations, respectively.

$$\varepsilon = \frac{1}{2}(k_{RU}\Delta l_{RU}^2 \ + \ k_\theta \Delta\theta^2 \ + \ k_\tau \Delta\tau^2) \tag{3.7}$$

An accurate parameter calibration must be performed for the three stiff-

nesses. As for the axial spring, the rotating unit is approximated to a rectangular bar of thickness t, length l_{RU}, and effective width h_{eff} defined as the average of the minimal and maximal axial load bearing widths of the rotating unit.

$$h_{eff} = \frac{1}{2}(h \ + \ l_{RU}\cos\gamma_{RU}\sin\gamma_{RU}) \tag{3.8}$$

Considering elastic modulus E, Equation 3.9 follows:

$$k_{RU} = \frac{Eth_{eff}}{l_{RU}} \tag{3.9}$$

Then, each hinge is modelled as a beam of thickness t, length l_{cut}, and width h, where l_{cut} is the thickness of the cut produced by the laser cutter. Bending of the beam in the x-z plane and twisting around x-axis are resisted with respective stiffnesses:

$$k_\theta = \tilde{K_\theta}\frac{Eth^3}{12l_{cut}} \tag{3.10}$$

$$k_\tau = \tilde{K_\tau}\frac{Eth^3}{6(1-\nu)l_{cut}}\left[1 - 3.36\frac{3h}{16t}\left(1 - \frac{h^4}{12t^4}\right)\right] \tag{3.11}$$

with $\tilde{K_\theta}$ and $\tilde{K_\tau}$ pre-factors to be accurately tuned.

To check the model's behaviour, three designs are considered with b = 24 mm, h = 0.7 mm, d = 6.2 mm, and progressively increasing base angle γ. In Figure 3.9(c) the designs are shown together with their elastic energy landscapes $\varepsilon(u_z, u_y)$. The minimum value of the energy landscape for each value of displacement p_z is marked with a colored dot: this allows easily to predict the out-of-plane tendency p_y of the three different designs. The evolution of ε^{eq} as a function of applied displacement u_z is reported in Figure 3.9(d) for the three considered designs. Consistent with our experimental findings, it is observed that small values of γ result in large out-of-plane deformations. Moreover, results suggest that increasing γ eventually leads to the structure becoming mono-stable.

Figure 3.9(e) shows the analytical model predictions in terms of normalized out-of-plane displacement for different combinations of bending pre-

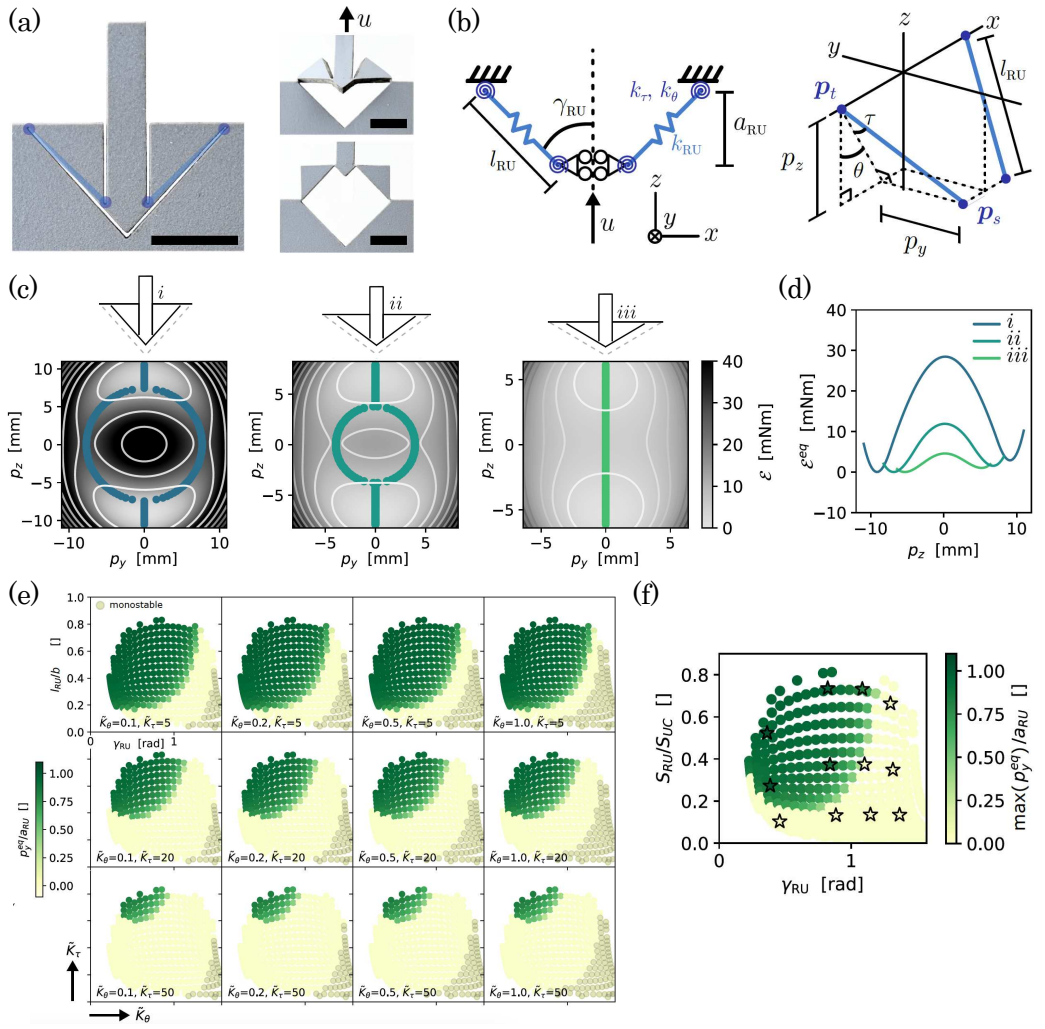

Figure 3.9: Analytical model for the Von Mises truss: a)Sample behavior; b)Analytical model parameters; c)Elastic energy landscapes; d)Equilibrium energy trend; e)Parameters pre-factors calibration; f)Match between model prediction and experimental tests for $\tilde{K_\theta} = 1$ and $\tilde{K_\tau} = 15$.

factor $\tilde{K_\theta}$ and twisting pre-factor $\tilde{K_\tau}$. High twisting pre-factor minimizes the out-of-plane deformation; high bending pre-factor leads to a broader range of mono-stable structures. Best-fitting values $\tilde{K_\theta} = 1$ and $\tilde{K_\tau} = 15$ lead to a very accurate prediction of experimental results: colored star markers from Figure 3.8(d) perfectly fall in the regions of corresponding color in Figure 3.9(f).

To resume the content of this section, a new tile definition is introduced and adopted to generate periodic kirigami structures. Mechanical tests highlight a peculiar behavior related with the deformation mechanism during deployment. This is found to be the key to relate the geometrical design with the structure bi-stability: both studies from analytical and experimental side are effective in explaining this unprecedented property of kirigami Von Mises trusses.

3.3 Aperiodic Tessellations

So far, only periodic kirigami meta-materials have been presented. Periodic tessellations, even if generated from different unit-cell definitions, can be found in the state of the art. In this section, the new tile definition introduced and analyzed in the previous section leads to a new sets of compatibility rules for the tessellation: the progressively removal of geometrical design constrains paves the pathway to new design degree of freedom. In other words, multi-stable kirigami meta-materials can be generated also by assembling non-identical Von Mises trusses.

The design process starts from the definition of multiple distinct convex polygons. From each polygon a super-cell generates by dividing them into triangular cells by drawing lines from their geometric centers to each vertex and each edge midpoint, see Figure 3.10(a). Pairs of these triangles outline the Von Mises trusses and define their angles γ and β, as well as their side length b.

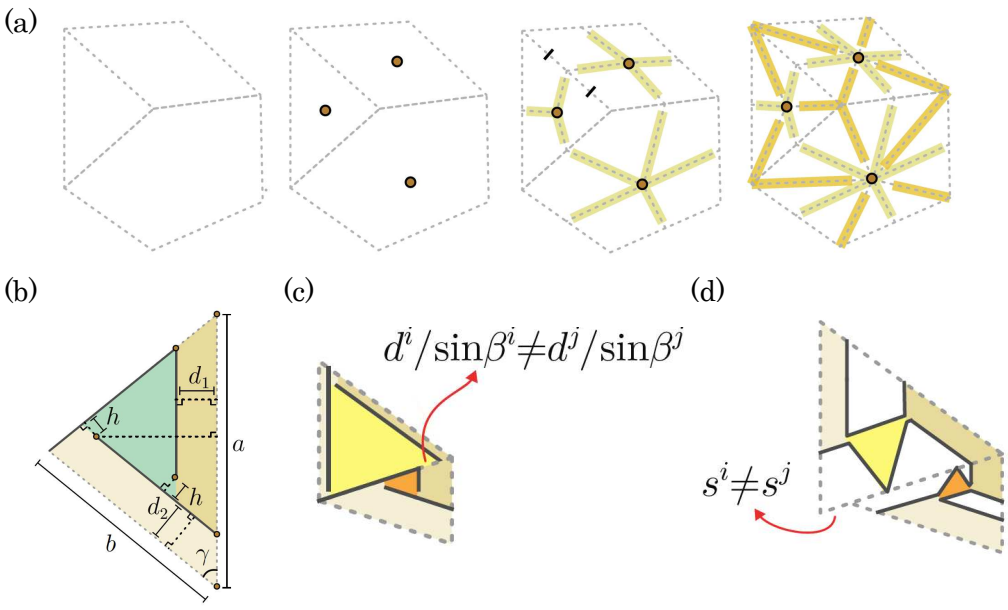

Figure 3.10: New kirigami design strategy: a)Design steps; b)Unit-cell parameters; c-d)Geometrical design constraints.

Next, the cutting pattern must be defined and cannot be chosen arbitrarily. More in details, cuts of adjacent unit-cells must align to ensure continuity: translated into equation, it means that $d/\sin\beta$ must be the same for adjacent unit-cells. If this condition is not satisfied, the discontinuity of Figure 3.10(c) would be present. Moreover, all kirigami Von Mises trusses must exhibit the same expansion factor s, to avoid the non-conformal expansion shown in Figure 3.10(d).

Considering super-cells whose vertex bisectors meet at their geometric centers, these can be patterned with symmetric kirigami Von Mises trusses. An example for this tiling family is the Penrose tiling, see Figure 3.11(a), consisting of two rhombus-shaped super-cells with edges of identical length $2b$ and vertex angles $2\pi/5$ and $3\pi/5$ for the first one, and $\pi/5$ and $4\pi/5$ for the second; four different unit-cells are consequently defined from the Penrose rhombi, all with the same edge length but different angles. The hinge thickness h is fixed at 0.7mm, as the fabrication lower limit, recalling that thin hinge means desirable low bending stiffness and consequently good bi-stability; tab width is chosen to satisfy the geometric constraints described above. This leads to the fact that the pull and base tabs of each Von Mises truss must have different widths d_1 and d_2. Figure 3.11(b) schematizes the geometrical constraints for the periodic tilings of Section 3.2 on the left and those, less, of the aperiodic Penrose tiling on the right, opening new design degrees of freedom. For this particular geometry the expansion factor s can be expressed as:

$$s = 2 - \frac{d_2}{b\ \sin 2\gamma} - \frac{d_1}{b\ \sin\gamma} - \frac{3h}{b\ \sin 2\gamma} \tag{3.12}$$

Following, given values for s and tab edge width $d_1/\sin\gamma$, Equation 3.12 provides the value for d_2 that satisfy the design constraints.

The resulting super-cell designs ($s = 1.3$, $d_1/\sin\gamma = 3mm$, $b = 12mm$) in their closed and expanded configurations are shown in Figure 3.11(c). Fabricated sample of Penrose geometry in collapsed and deployed states is reported in Figure 3.11(d).

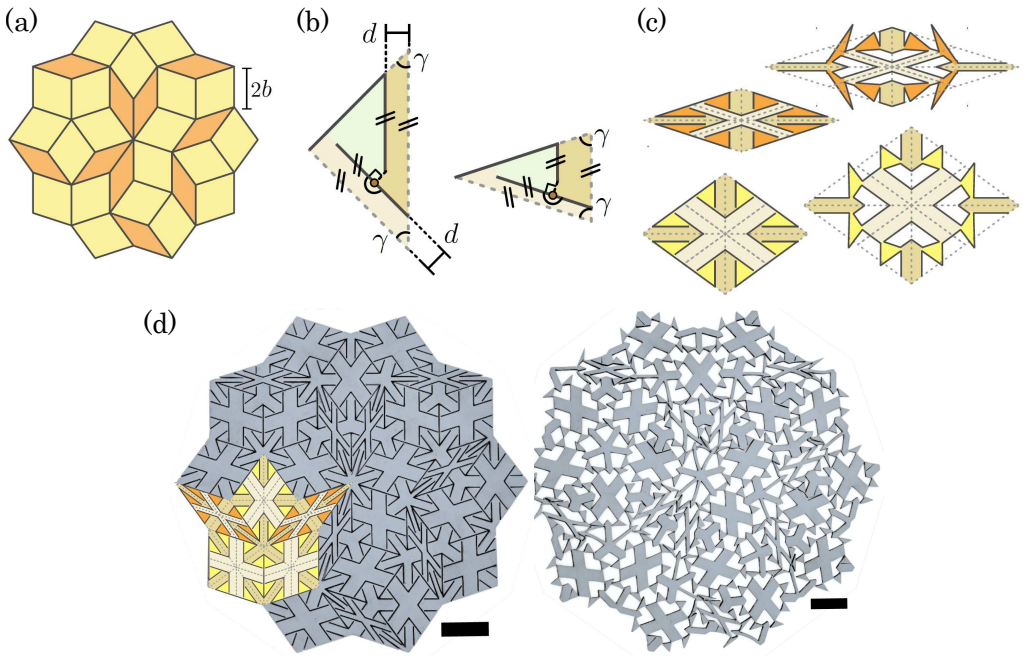

Figure 3.11: Penrose kirigami: a)Penrose tiling; b)Design degrees of freedom; c)Diamond-shaped super-cells; d)Fabricated Penrose meta-material, collapsed and deployed. Scale bar = 20 mm.

The proposed design strategy is not limited to these geometries. Both periodic kirigami meta-materials and the Penrose tiling consist indeed in symmetric kirigami Von Mises trusses, but the methodology can be extended also to asymmetric Von Mises trusses.

An example is found in the Girih tiling. Girih tiles, decorative Islamic geometric patterns used in architecture and handicraft objects, consist in five polygons with constant edge length l_G, which are a regular decagon, an elongated hexagon, a rhombus, a regular pentagon, and a non-convex hexagon (which is divided into two identical convex trapezoidal super-cells to match with the proposed design methodology). Seven out of nine unit-cells (excluding those marked as 2 and 3 in Figure 3.12(a)) are characterized by $\gamma \neq \beta$. Additionally, two pairs of triangles (5-6 and 7-8) are not mirror images of each other and therefore form two asymmetric von Mises trusses when combined.

For kirigami Von Mises trusses with $\gamma \neq \beta$, the equation for the expansion

ratio generalizes as Equation 3.13, which, given values for s, d_1 and h, can be solved to determine d_2.

$$s = 1 + \frac{2}{a}\left[b\cos\gamma + \frac{d_2}{\sin\gamma}\left(\frac{\cos\beta\sin\gamma}{\sin(\beta+\gamma)} - 1\right) - \frac{d_1\,\sin\beta}{\sin\beta\tan\gamma} - h\left(\frac{\cos\gamma}{\sin(\beta+\gamma)} + \frac{1}{\sin\gamma}\right)\right] \tag{3.13}$$

However, asymmetric trusses on one side require the removal of most of geometrical constraints (see Figure 3.12(b)-right) but on the other side an additional design rule must be satisfied to ensure a continuous kirigami cut, which is the base tab edge lengths $d_2/\sin\gamma$ matching between the pair of triangles, as schematized in Figure 3.12(c). When imposing this additional constraint, Equation 3.13 yields no solution, meaning that asymmetric trusses cannot be generated from kirigami patterns featuring tabs of constant width.

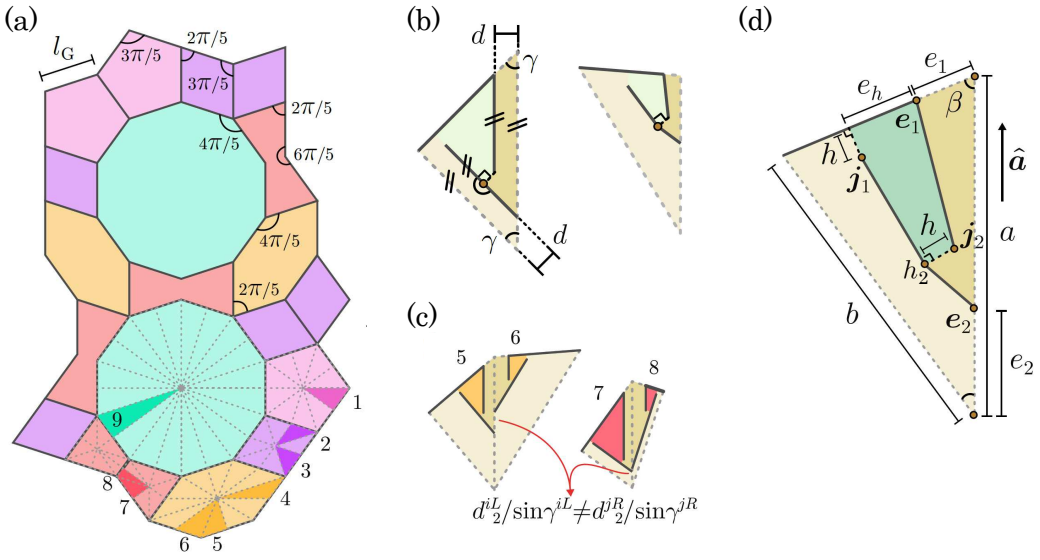

Figure 3.12: Asymmetric aperiodic kirigami: a)Girih tiling; b)Design degrees of freedom; c)Geometrical constraints for asymmetric Von Mises truss; d)Generalized unit-cell.

To overcome this issue, the cuts are allowed to be placed anywhere within the triangle. Referring to Figure 3.12(d), end points e_1 and e_2 are designed

to match the tab edges between triangles, while points j_1 and j_2 control the expansion factor s by Equation 3.14, with $\hat{\mathbf{a}}$ the unit vector along the cell's edge.

$$s = 1 + \frac{2}{a}(\mathbf{j}_1 - \mathbf{j}_2) \cdot \hat{\mathbf{a}} \tag{3.14}$$

To define the kirigami pattern for asymmetric trusses, an optimization process is hence required; each cell pair that forms a complete Von Mises truss is optimized jointly. Geometric parameters $s = 1.4$, $l_G = 24$mm, $h = 0.7$, $e_1 = 2$mm are kept fixed, while values for e_h and γ_{RU} for each cell of the pair are obtained by minimizing a design cost function with the following form:

$$C = W_A A + W_B B + W_C C + W_D D \tag{3.15}$$

in which each term corresponds to a geometrical design requirements i (A-D), with a weight W_i assigned to each of them to define the "importance" of that specific constraint.

Looking at Figure 3.12(d), term A forces the point j_2 to lie close to the cell edge with optimal distance h (distance is minimized to avoid the Von Mises truss becoming a 4-bar mechanism, significantly reducing the bi-stability of the truss). Term B ensures that point j_1 lies between point e_1 and the top-left corner, favouring being closer to the latter. Term C ensures that design points j_2 for adjacent cells lie close together, with optimal distance $2h$. Term D confines the design points j_1, j_2 and h_2 inside the cell region.

Resulting super-cells cut patterns in both collapsed and deployed configurations are shown in Figure 3.13(a), in which the geometry of the asymmetric kirigami Von Mises trusses is the output of the optimization process on the couple of adjacent unit-cells.

An arbitrary tessellation of Girih tilings is fabricated: the expected deployment of the individual tiles is superimposed to the picture of the actual sample in Figure 3.13(b). Excellent agreement is found, confirming that the designed meta-material is effectively multi-stable and its property is governed by the behavior of the single super-cells.

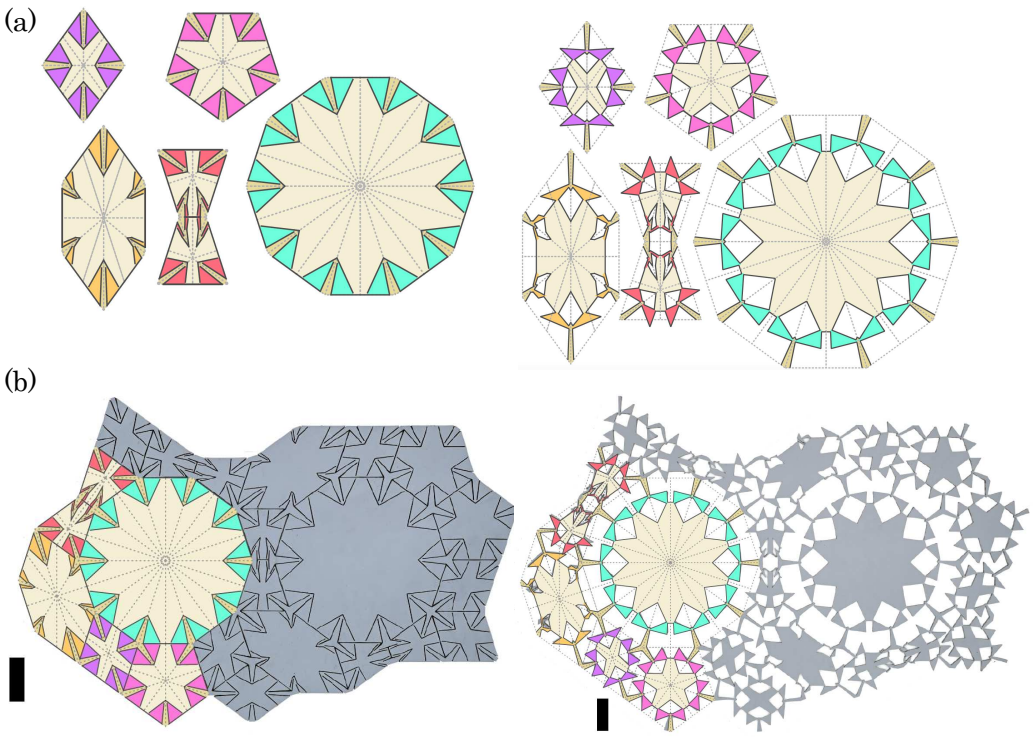

Figure 3.13: Girih kirigami: a)Girih five super-cells, collapsed and deployed; b)Fabricated Girih meta-material, collapsed and deployed. Scale bar = 20 mm.

3.4 Conclusions

In this chapter a comprehensive design strategy for creating multi-stable kirigami meta-materials has been introduced. These meta-materials not only can be deployed from a collapsed to a deployed state, but are characterized by a wide number of intermediate stable configurations, thanks to the new definition of the unit-cell with a lower connectivity in comparison with bi-stable periodic kirigami found in literature which collapse under in-plane compression applied at the outer edges. In other words, the multi-stability is due to the weak coupling between the kirigami Von Mises trusses inside the meta-material: indeed, the collapse of one truss in a super-cell does not force the contraction of its neighbors. Also, the unconnected vertex in the unit-cell leads, during the deployment process, to high-friction contacts as in Figure 3.7(d).

Starting from a deep understanding of the physics underlying the deployment process of the kirigami Von Mises trusses and the consequent bi-stability, mechanical tests are performed on periodic samples obtained from tessellations of square and hexagonal super-cells. Results are compared and discussed in terms of elastic energy performance, to explain the extremely non-linear mechanics of such structures.

But most importantly, this new design strategy overcomes the limitation set by periodicity. While kirigami meta-materials from literature must consist in a face-to-face tessellation of a unit-cell, these novel designs allow for aperiodic tilings, see the Penrose as example, and also for arbitrary polygonal tilings thanks to the possibility of designing asymmetric Von Mises trusses if needed.

The proposed new methodology offers many hints for future studies. Among these, this strategy provides a novel platform to design pluripotent shape-morphing structures, and can be also easily generalized to three-dimensional meta-materials thanks to the opportunities opened by recent advances in additive fabrication.

Conclusion

In this thesis, the mechanical behavior of cellular structures and architected materials is explored through both experiments and simulation outputs. This combination allows, after robust validation of the numerical model, to understand all the phenomena that rule the interesting and peculiar mechanical response of these classes of materials.

Following an introduction to the world of cellular structures, the concept of novel multi-phase composite cellular structures is presented. Inspired by the natural world, where biological structures are the result of millions of years of evolution, and by the recent development of multi-material additive manufacturing technologies, cellular TPMS structures are filled with polymeric foam (Section 1.2) and with non-Newtonian liquid (Section 1.3). Mechanical tests proved the properties enhancement for the proposed multi-phase configurations. In particular, the specific energy absorption of foam-filled structures is about 20% higher than the initial lattice: surprisingly this result does not come from the foam load-bearing contribution, but from its role in affecting the overall deformation mechanism of the whole structure. The interaction between the lattice architecture and the filler material is even more emphasized in the shear-thickening-fluid-filled configuration. This concept is developed to design a meta-material with adaptive mechanical response: the viscous energy dissipation of the dilatant fluid depends on the shear-rate field, which, again, depends on the interaction between the fluid and the cellular structure. As a result, the acceleration profile is function of the dynamic load speed, i.e. the impact velocity, more than 50% smoothed in the STF-filled structure scenario.

Cellular structures and architected geometries are now spreading across engineering disciplines thank to the impressive advancements of additive manufacturing technologies. In this framework, the effect of the fabrication process and its key parameters on the mechanical properties of the 3D-printed part are studied up to failure regime. The multi-scale model proposed in Section 2.2 is found to be an accurate and computationally efficient approach to understand and predict the mechanical response and damage mechanisms of components produced via FDM technology. Once the influence of the extrusion temperature on the properties of the cohesive region is evaluated, the model can effectively reproduce the failure phenomena occurring. Moreover, an anisotropic damage model is proposed (Section 2.3) and numerically implemented to capture the failure mechanisms of thin-walled complex geometries. After a successful validation against experimental tests, the model allows to relate the micro-scale inter- and intra-layer damages to the macro-scale failure of the whole structure.

In the last part of the work, the peculiar behavior of architected materials is explored in Sections 3.2-3.3. In the world of kirigami-based structures, the role of cut pattern geometry on the physics underlying the bi-stability of a kirigami Von Mises truss is investigated with a combined experimental-analytical approach. A new unit-cell tile is defined from this, with less design constraints and additional degrees of freedom, which consequently works as a building block for novel periodic, aperiodic, and possibly arbitrary, multi-stable meta-materials, which allows to widely expand the design space for kirigami-based devices, revolutionizing the range of possible applications.

In conclusion, the findings of this thesis are no doubt going to enrich the collective knowledge in the field, and hopefully they will offer a foundation for new advancements in the design and fabrication of a new generation of architected and multi-material structures with enhanced, smarter, and functional properties.

Bibliography

[1] L. J. Gibson and M. F. Ashby, *Cellular Solids: Structure and Properties*. Cambridge University Press, 1997.

[2] R.-Y. Yao, B. Zhang, G.-S. Yin, and Z.-Y. Zhao, "Energy absorption behaviors of foam-filled holed tube subjected to axial crushing: experimental and theoretical investigations," *Mech. Adv. Mater. Struct.*, vol. 28, no. 24, pp. 2501–2514, 2021.

[3] H. Yin, G. Wen, Z. Liu, and Q. Qing, "Crashworthiness optimization design for foam-filled multi-cell thin-walled structures," *Thin. Walled Struct.*, vol. 75, pp. 8–17, 2014.

[4] A. Ghamarian, H. R. Zarei, and M. T. Abadi, "Experimental and numerical crashworthiness investigation of empty and foam-filled end-capped conical tubes," *Thin. Walled Struct.*, vol. 49, no. 10, pp. 1312–1319, 2011.

[5] R. Yao, T. Pang, S. He, Q. Li, B. Zhang, and G. Sun, "A bio-inspired foam-filled multi-cell structural configuration for energy absorption," *Composites Part B*, vol. 238, p. 109801, 2022.

[6] X. Ren, Y. Zhang, C. Han, D. Han, X. Zhang, X. Zhang, and Y. Xie, "Mechanical properties of foam-filled auxetic circular tubes: experimental and numerical study," *Thin. Walled Struct.*, vol. 170, p. 108584, 2022.

[7] H. Mozafari, S. Khatami, H. Molatefi, V. Crupi, G. Epasto, and E. Guglielmino, "Finite element analysis of foam-filled honeycomb structures under impact loading and crashworthiness design," *Int. J. Crashworthiness*, vol. 21, no. 2, pp. 148–160, 2016.

[8] H. Luo, X. Ren, Y. Zhang, X. Zhang, X. Zhang, C. Luo, X. Cheng, and Y. Xie, "Mechanical properties of foam-filled hexagonal and re-entrant honeycombs under uniaxial compression," *Compos. Struct.*, vol. 280, p. 114922, 2022.

[9] A. Airoldi, N. Novak, F. Sgobba, A. Gilardelli, and M. Borovinšek, "Foam-filled energy absorbers with auxetic behavior for localized impacts," *Materials Science & Engineering A*, vol. 788, p. 139500, 2020.

[10] T. Liu, C. Chen, and Y. Cheng, "Mechanical characteristics and foam filling enhancement mechanism of polymeric periodic hybrid structures under uniaxial compression," *Materials & Design*, vol. 227, p. 111762, 2023.

[11] M. Prajapati, A. Kumar, S.-C. Lin, and J.-Y. Jeng, "Multimaterial additive manufacturing with lightweight closed-cell foam-filled lattice structures for enhanced mechanical and functional properties," *Addit. Manuf.*, vol. 54, p. 102766, 2022.

[12] C. Sciancalepore, E. Togliatti, M. Marozzi, F. Rizzi, D. Pugliese, A. Cavazza, O. Pitirollo, M. Grimaldi, and D. Milanese, "Flexible pbat-based composite filaments for tunable fdm 3d printing," *ACS Appl. Bio Mater.*, vol. 5, no. 7, pp. 3219–3229, 2022.

[13] S. Black and et al, "Mechanical behaviour of gel-filled additively-manufactured lattice structures under quasi-static compressive loading," *Materials Today Communications*, vol. 35, p. 106164, 2023.

[14] L. Wu, F. Zhao, Z. Lu, J.-H. Lin, and Q. Jiang, "Impact energy absorption composites with shear stiffening gel-filled negative poisson's ratio skeleton by kirigami method," *Composite Structures*, vol. 298, p. 116009, 2022.

[15] M. Montanari and et al, "Defect sensitivity mitigation in the compressive mechanical response of two-phase lattice metamaterials," *Composite Structures*, vol. 323, p. 117501, 2023.

[16] S. Soe and et al, "Investigating the dynamic compression response of elastomeric, additively manufactured fluid-filled structures via experimental and finite element analysis," *Additive Manufacturing*, vol. 39, p. 101885, 2021.

[17] M. Wei and et al, "Shear thickening fluids and their applications," *Materials & Design*, vol. 216, p. 110570, 2022.

[18] M. Zarei and J. Aalaie, "Application of shear thickening fluids in material development," *Journal of Materials Research and Technology*, vol. 9(5), pp. 10411–10433, 2020.

[19] L. Lam and et al, "Dynamic crushing performance of bio-inspired sandwich structures with beetle forewing cores," *International Journal of Impact Engineering*, vol. 173, p. 104456, 2023.

[20] X. Wu and et al, "Experimental study on dynamic compressive behaviour of sandwich panel with shear thickening fluid filled pyramidal lattice truss core," *International Journal of Mechanical Sciences*, vol. 138-139, pp. 467–475, 2018.

[21] M. Jeddi and et al, "Energy absorption characteristics of aluminum sandwich panels with shear thickening fluid (stf) filled 3d fabric cores under dynamic loading conditions," *Thin-Walled Structures*, vol. 168, p. 108254, 2021.

[22] Q. Hu and et al, "Dynamic compressive behavior of shear thickening fluid-filled honeycomb," *International Journal of Mechanical Sciences*, vol. 229, p. 107493, 2022.

[23] Q. Hu and et al, "Dynamic responses of shear thickening fluid-filled lattice structures," *International Journal of Impact Engineering*, vol. 189, p. 104954, 2024.

[24] C. Caglayan and et al, "Impact response of shear thickening fluid filled polyurethane foam core t sandwich composites," *Composite Structures*, vol. 243, p. 112171, 2020.

[25] F. Zhao, L. Wu, Z. Lu, J.-H. Lin, and Q. Jiang, "Design of shear thickening fluid/polyurethane foam skeleton sandwich composite based on non-newtonian fluid solid interaction under low-velocity impact," *Materials & Design*, vol. 213, p. 110375, 2022.

[26] L. Lam and et al, "Dynamic crushing and energy absorption of bio-inspired shear thickening fluid-filled origami metastructure," *Engineering Structures*, vol. 299, p. 117122, 2024.

[27] S. Wang and et al, "Experimental study of solid-liquid origami composite structures with improved impact resistance," *Theoretical and Applied Mechanics Letters*, vol. 14, p. 100508, 2024.

[28] T. Tamir, G. Xiong, Q. Fang, *et al.*, "A feedback-based print quality improving strategy for fdm 3d printing: an optimal design approach," *International Journal of Advanced Manufacturing Technology*, vol. 120, no. 9, pp. 2777–2791, 2022.

[29] S. Tientcheu, J. Marae-Djouda, M. A. Bouaziz, and E. Lacazedieu, "A review on fused deposition modeling materials with analysis of key process parameters influence on mechanical properties," *International Journal of Advanced Manufacturing Technology*, vol. 130, no. 5–6, pp. 2119–2158, 2024.

[30] C. S. Lee, S. G. Kim, H. J. Kim, and S. H. Ahn, "Measurement of anisotropic compressive strength of rapid prototyping parts," *Journal of Materials Processing Technology*, vol. 187-188, pp. 627–630, 2007.

[31] V. Vega *et al.*, "The effect of layer orientation on the mechanical properties and microstructure of a polymer," *Journal of Materials Engineering and Performance*, vol. 20, no. 6, pp. 978–988, 2011.

[32] W. Wu *et al.*, "Influence of layer thickness and raster angle on the mechanical properties of 3d-printed peek and a comparative mechanical study between peek and abs," *Materials*, vol. 8, no. 9, pp. 5834–5846, 2015.

[33] H. Izadi Gonabadi, Y. Chen, A. Yadav, and S. Bull, "Investigation of the effect of raster angle, build orientation, and infill density on the elastic response of 3d printed parts using finite element microstructural modeling and homogenization techniques," *The International Journal of Advanced Manufacturing Technology*, vol. 118, pp. 1485–1510, 2022.

[34] T. McLouth *et al.*, "The impact of print orientation and raster pattern on fracture toughness in additively manufactured abs," *Additive Manufacturing*, vol. 18, pp. 103–109, 2017.

[35] O. A. Mohamed, S. H. Masood, and J. L. Bhowmik, "Optimization of fused deposition modeling process parameters: a review of current research and future prospects," *Advances in Manufacturing*, vol. 3, no. 1, pp. 42–53, 2015.

[36] M. Hikmat, S. Rostam, and Y. M. Ahmed, "Investigation of tensile property-based taguchi method of PLA parts fabricated by FDM 3d printing technology," *Results in Engineering*, vol. 11, 2021.

[37] A. Lanzotti, M. Grasso, G. Staiano, and M. Martorelli, "The impact of process parameters on mechanical properties of parts fabricated in pla with an open-source 3-d printer," *Rapid Prototyping Journal*, vol. 21, no. 5, pp. 604–617, 2015.

[38] A. Deka and J. F. Hall, "A framework for optimizing process parameters in fused deposition modeling using predictive modeling coupled response surface methodology," *International Journal of Advanced Manufacturing Technology*, vol. 131, no. 1, pp. 447–466, 2024.

[39] Q. Sun, G. M. Rizvi, C. T. Bellehumeur, and P. Gu, "Effect of processing conditions on the bonding quality of fdm polymer filaments," *Rapid Prototyping Journal*, vol. 14, no. 2, pp. 72–80, 2008.

[40] B. Brenken *et al.*, "Development and validation of extrusion deposition additive manufacturing process simulations," *Additive Manufacturing*, vol. 25, pp. 218–226, 2019.

[41] A. Cattenone *et al.*, "Finite element analysis of additive manufacturing based on fused deposition modeling: Distortions prediction and comparison with experimental data," *Journal of Manufacturing Science and Engineering*, vol. 141, 2019.

[42] H. Vanaei *et al.*, "Numerical prediction for temperature profile of parts manufactured using fused filament fabrication," *Journal of Manufacturing Processes*, vol. 76, pp. 548–558, 2022.

[43] S. Garzon-Hernandez, D. Garcia-Gonzalez, A. Jérusalem, and A. Arias, "Design of fdm 3d printed polymers: an experimental-modelling methodology for the prediction of mechanical properties," *Materials & Design*, vol. 188, p. 108414, 2020.

[44] J. Yin, C. Lu, J. Fu, Y. Huang, and Y. Zheng, "Interfacial bonding during multi-material fused deposition modeling (fdm) process due to inter-molecular diffusion," *Materials & Design*, vol. 150, pp. 104–112, 2018.

[45] M. Khosravani *et al.*, "Fracture behavior of additively manufactured components: A review," *Theoretical and Applied Fracture Mechanics*, vol. 109, p. 102763, 2020.

[46] A. Moetazedian *et al.*, "Damage in extrusion additive manufactured biomedical polymer: Effects of testing direction and environment during cyclic loading," *Journal of the Mechanical Behavior of Biomedical Materials*, vol. 118, p. 104397, 2021.

[47] N. Aliheidari *et al.*, "Interlayer adhesion and fracture resistance of polymers printed through melt extrusion additive manufacturing process," *Materials & Design*, vol. 156, pp. 351–361, 2018.

[48] S. Sharafi *et al.*, "A review of factors that influence the fracture toughness of extrusion-based additively manufactured polymer and polymer composites," *Additive Manufacturing*, vol. 38, p. 101830, 2021.

[49] M. Anoop and P. Senthil, "Homogenisation of elastic properties in fdm components using microscale rve numerical analysis," *Journal of the Brazilian Society of Mechanical Sciences and Engineering*, vol. 41, p. 540, 2019.

[50] P. Ferretti *et al.*, "Representative volume element (rve) analysis for mechanical characterization of fused deposition modeled components," *Polymers*, vol. 13, no. 20, p. 3555, 2021.

[51] A. Zekavat *et al.*, "Investigating the effect of fabrication temperature on mechanical properties of fused deposition modeling parts using x-ray computed tomography," *The International Journal of Advanced Manufacturing Technology*, vol. 100, no. 1–4, pp. 287–296, 2019.

[52] G. Ibrahim and A. Albarbar, "A new approach to the cohesive zone model that includes thermal effects," *Composites Part B: Engineering*, vol. 167, pp. 370–376, 2019.

[53] B. Ameria *et al.*, "Fracture loads prediction of the modified 3d-printed abs specimens under mixed-mode i/ii loading," *Engineering Fracture Mechanics*, vol. 235, p. 107181, 2020.

[54] N. Razavi *et al.*, "Mixed-mode fracture prediction of acrylonitrile butadiene styrene fabricated via fused deposition modeling," *Proceedings of the Institution of Mechanical Engineers, Part L: Journal of Materials: Design and Applications*, vol. 237, no. 5, pp. 1042–1053, 2023.

[55] M. He *et al.*, "Compressive performance and fracture mechanism of bio-inspired heterogeneous glass sponge lattice structures manufactured by selective laser melting," *Materials & Design*, vol. 214, p. 110396, 2022.

[56] P. Wang *et al.*, "Mechanical properties and energy absorption of fcc lattice structures with different orientation angles," *Acta Mechanica*, vol. 231, pp. 3129–3144, 2020.

[57] M. R. O'Masta, L. Dong, L. St-Pierre, H. N. G. Wadley, and V. S. Deshpande, "The fracture toughness of octet-truss lattices," *Journal of the Mechanics and Physics of Solids*, vol. 98, pp. 271–289, 2017.

[58] I. Maskery, N. T. Aboulkhair, A. O. Aremu, C. J. Tuck, and I. A. Ashcroft, "Compressive failure modes and energy absorption in additively manufactured double gyroid lattices," *Additive Manufacturing*, vol. 16, pp. 24–29, 2017.

[59] A. Kumar, L. Collini, A. Daurel, and J.-Y. Jeng, "Design and additive manufacturing of closed cells from supportless lattice structure," *Additive Manufacturing*, vol. 33, p. 101168, 2020.

[60] J. Lemaitre, "A continuous damage mechanics model for ductile fracture," *Journal of Engineering Materials and Technology*, vol. 107, pp. 83–89, 1985.

[61] C. Bhat, A. Kumar, and J.-Y. Jeng, "Effect of atomic tassellations on structural and functional properties of additive manufactured lattice structures," *Additive Manufacturing*, vol. 47, p. 102326, 2021.

[62] L. Jin and S. Yang, "Engineering kirigami frameworks toward real-world applications," *Advanced Materials*, vol. 36, no. 2308560, 2024.

[63] J. Tao, H. Khosravi, V. Deshpande, T. Zhang, and S. Li, "Engineering by cuts: How kirigami principle enables unique mechanical properties and functionalities," *Advanced Science*, vol. 10, no. 2204733, 2022.

[64] S. Chen, J. Chen, X. Zhang, *et al.*, "Kirigami/origami: unfolding the new regime of advanced 3d microfabrication/nanofabrication with "folding"," *Light: Science & Applications*, vol. 9, no. 75, 2020.

[65] M. K. Blees, A. W. Barnard, P. A. Rose, *et al.*, "Graphene kirigami," *Nature*, vol. 524, pp. 204–207, 2015.

[66] H. Khosravi, S. M. Iannucci, and S. Li, "Pneumatic soft actuators with kirigami skins," *Frontiers in Robotics and AI*, vol. 8, 2021.

[67] Y. Tang, G. Lin, S. Yang, Y. K. Yi, R. D. Kamien, and J. Yin, "Programmable kiri-kirigami metamaterials," *Advanced Materials*, vol. 29, no. 1604262, 2017.

[68] L. H. Dudte, G. P. T. Choi, K. P. Becker, *et al.*, "An additive framework for kirigami design," *Nature Computational Science*, vol. 3, pp. 443–454, 2023.

[69] R. Zhao, S. Lin, H. Yuk, and X. Zhao, "Kirigami enhances film adhesion," *Soft Matter*, vol. 14, pp. 2515–2525, 2018.

[70] E. E. Evke, D. Meli, and M. Shtein, "Developable rotationally symmetric kirigami-based structures as sensor platforms," *Advanced Materials Technologies*, vol. 4, pp. 1–11, 2019.

[71] A. Rafsanjani and D. Pasini, "Bistable auxetic mechanical metamaterials inspired by ancient geometric motifs," *Extreme Mechanics Letters*, vol. 9, pp. 291–296, 2016.

[72] L. Jin, R. Khajehtourian, J. Mueller, A. Rafsanjani, V. Tournat, K. Bertoldi, and D. M. Kochmann, "Guided transition waves in multistable mechanical metamaterials," *Proceedings of the National Academy of Sciences*, vol. 117, no. 5, pp. 2319–2325, 2020.

[73] A. Lamoureux, K. Lee, M. Shlian, *et al.*, "Dynamic kirigami structures for integrated solar tracking," *Nature Communications*, vol. 6, p. 8092, 2015.

[74] A. Rafsanjani *et al.*, "Kirigami skins make a simple soft actuator crawl," *Science Robotics*, vol. 3, no. eaar7555, 2018.

[75] S. Babaee, S. Pajovic, A. Rafsanjani, *et al.*, "Bioinspired kirigami metasurfaces as assistive shoe grips," *Nature Biomedical Engineering*, vol. 4, pp. 778–786, 2020.

[76] Y. Yang *et al.*, "Grasping with kirigami shells," *Science Robotics*, vol. 6, no. eabd6426, 2021.

[77] G. P. T. Choi, L. H. Dudte, and L. Mahadevan, "Programming shape using kirigami tessellations," *Nature Materials*, vol. 18, pp. 999–1004, 2019.

[78] T. Chen, J. Panetta, M. Schnaubelt, and M. Pauly, "Bistable auxetic surface structures," *ACM Transactions on Graphics*, vol. 40, no. 4, 2021.